# MOUNTAIN-PLAINS CONSORTIUM

**MPC 24-526** | G. Schurmann Kern and F.K. Ting

## LABORATORY MEASUREMENTS OF BED SHEAR STRESS AND SOIL EROSION RATE IN COHESIVE SOILS

MOUNTAIN-PLAINS CONSORTIUM REGION 8

A University Transportation Center sponsored by the U.S. Department of Transportation serving the Mountain-Plains Region. Consortium members:

Colorado State University
North Dakota State University
South Dakota State University
University of Colorado Denver
University of Denver
University of Utah
Utah State University
University of Wyoming

**Technical Report Documentation Page**

| 1. Report No. | 2. Government Accession No. | 3. Recipient's Catalog No. |
|---|---|---|
| MPC 596 | | |

| 4. Title and Subtitle | 5. Report Date |
|---|---|
| Laboratory Measurements of Bed Shear Stress and Soil Erosion Rate in Cohesive Soils | May 2024 |
| | 6. Performing Organization Code |

| 7. Author(s) | 8. Performing Organization Report No. |
|---|---|
| Gunnar Schurmann Kern, M.S.<br>Francis C. K. Ting, Ph.D., P.E | MPC 24-526 |

| 9. Performing Organization Name and Address | 10. Work Unit No. (TRAIS) |
|---|---|
| Department of Civil and Environmental Engineering<br>South Dakota State University<br>Brookings, SD 57007 | 11. Contract or Grant No. |

| 12. Sponsoring Agency Name and Address | 13. Type of Report and Period Covered |
|---|---|
| Mountain-Plains Consortium<br>North Dakota State University<br>PO Box 6050, Fargo, ND 58108 | Final Report |
| | 14. Sponsoring Agency Code |

15. Supplementary Notes

16. Abstract

The relationship between soil erosion rate and bed shear stress is an important problem in sediment transport and scour. However, obtaining reliable measurements of soil erodibility is challenging, both in the field and in the laboratory. The objective of this study is to investigate an experimental setup for conducting bed shear stress and soil erosion rate measurements using an open-channel flume with a rough bed. The experiments were performed in an A-8 hydraulic channel with a fixed gravel bed. The flow discharge was kept constant and bed shear stress was varied by changing the channel slope. A soil specimen was placed in a circular cutout in the gravel bed. Soil samples with a range of unconfined compressive strengths were prepared by changing the water content, and the soil erosion rate was found from the difference in the mass of the sample taken before and after the test. Two different methods were used to determine the bed shear stress: from the measured velocity profile using the logarithmic law, and from the measured flow depth and channel slope. The velocity profiles were obtained using the particle image velocimetry (PIV) technique. The measured data showed that the equivalent grain roughness correlated well with the size of the large grains in the gravel bed and decreased with the flow-depth-to-grain-diameter ratio. It was found that the bed shear stress in the sediment recess determined using the logarithmic law was not significantly different from the bed shear stress acting on the surrounding gravels when the equivalent roughness of the clay bed was taken to be the same as that of the gravel bed. It was also found that the measured soil erosion rate correlated well with the unconfined compressive strength or water content.

| 17. Key Word | 18. Distribution Statement |
|---|---|
| bridges, cohesive soils, erosion, laboratory tests, roughness, scour, shear stress, test facilities, test procedures, turbulence, velocimeters | Public distribution |

| 19. Security Classif. (of this report) | 20. Security Classif. (of this page) | 21. No. of Pages | 22. Price |
|---|---|---|---|
| Unclassified | Unclassified | 118 | n/a |

**Form DOT F 1700.7 (8-72)** Reproduction of completed page authorized

# Laboratory Measurements of Bed Shear Stress and Soil Erosion Rate in Cohesive Soils

Gunnar Schurmann Kern, M.S.
Francis C. K. Ting, Ph.D., P.E.

Department of Civil and Environmental Engineering
South Dakota State University
Brookings, SD 57007

May 2024

## Acknowledgements

Funding for this work was provided by the Mountain-Plains Consortium (MPC) and South Dakota State University (SDSU). This report is based primarily on the thesis of Gunnar Kern with Francis Ting as the thesis advisor. We would like to thank Dr. Allen Jones for providing valuable advice on geotechnical testing methods and procedures. We would also like to thank Dr. Suzette Burckhard and Dr. Rhoda Burrows for providing valuable comments on the work as members of the thesis committee.

## Disclaimer

# ABSTRACT

The relationship between soil erosion rate and bed shear stress is an important problem in sediment transport and scour. However, obtaining reliable measurements of soil erodibility is challenging, both in the field and in the laboratory. The objective of this study is to investigate an experimental setup for conducting bed shear stress and soil erosion rate measurements using an open-channel flume with a rough bed. The experiments were performed in an A-8 hydraulic channel with a fixed gravel bed. The flow discharge was kept constant and bed shear stress was varied by changing the channel slope. A soil specimen was placed in a circular cutout in the gravel bed. Soil samples with a range of unconfined compressive strengths were prepared by changing the water content, and the soil erosion rate was found from the difference in the mass of the sample taken before and after the test. Two different methods were used to determine the bed shear stress: from the measured velocity profile using the logarithmic law, and from the measured flow depth and channel slope. The velocity profiles were obtained using the particle image velocimetry (PIV) technique. The measured data showed that the equivalent grain roughness correlated well with the size of the large grains in the gravel bed and decreased with the flow-depth-to-grain-diameter ratio. It was found that the bed shear stress in the sediment recess determined using the logarithmic law was not significantly different from the bed shear stress acting on the surrounding gravels when the equivalent roughness of the clay bed was taken to be the same as that of the gravel bed. It was also found that the measured soil erosion rate correlated well with the unconfined compressive strength or water content.

# TABLE OF CONTENTS

# LIST OF FIGURES

# LIST OF TABLES

# 1. INTRODUCTION

## 1.1 Definitions

Erosion occurs in rivers and streams when the bed shear stress produced by the flow exceeds the critical shear stress the soil bed can resist. The erosion rate is a measurement of the amount of soil lost over a specific period. Previous studies have utilized erosion function apparatus (EFA) devices to measure the relationship between soil erosion rate and bed shear stress. Bed shear stress is defined as the force of friction from a fluid acting on a unit area of the soil bed. The critical shear stress is the friction force per unit area needed to initiate soil erosion. Among other soil properties, the unconfined compressive strength has been used to predict the critical shear stress of clay soils. The unconfined compressive strength is the maximum axial compressive stress that a cylindrical sample can withstand under unconfined conditions.

## 1.2 Motivation

This study is concerned with the EFA. Existing EFA type devices use an open-channel flume or water tunnel to recirculate water. Because these devices typically have smooth walls, the local shear stress developed over the soil sample can be much higher than the wall shear stress computed based on a smooth surface. The bed shear stress also varies with the height of soil protrusion into the flow. When the soil surface is eroding non-uniformly, the configuration of the soil protrusion is constantly changing. Therefore, a constant and uniform shear stress cannot be maintained over the soil surface, making it difficult to establish a reliable relationship between soil erosion rate and bed shear stress. Various sensing devices have been developed and employed by researchers to monitor the position of the eroding surface and automatically advance the soil sample without the need for operator intervention, with varying degrees of success.

## 1.3 Objectives and Scope of Work

The present study investigates a different design for the EFA to measure the erosion-rate-versus-shear-stress curve. Instead of the smooth wall used in most devices, a layer of gravel was glued to acrylic sheets and installed in a tilting flume to produce fully developed turbulent flow over a rough surface. A circular cutout was made in the gravel bed to accommodate a circular soil sample. It is hypothesized that the erosive action of the flowing water in this experimental arrangement would be controlled primarily by the boundary-layer turbulence generated on the gravel bed, and thus is less sensitive to the surface roughness and configuration of the soil surface as the erosion progresses. The specific objectives of the experimental study are to:

1. Determine the effect of the soil erosion on the bed shear stress in the experimental setup described above
2. Measure the erosion-rate-versus-shear-stress curves of Nora Moody clay to investigate the effect of unconfined compressive strength and water content on the soil critical shear stress and erosion rate

The turbulent velocity field over the gravel bed and clay sample was measured under a steady, uniform flow condition using a particle image velocimetry (PIV) system. The flow depth in the flume and the channel slope were also measured. The bed shear stress was determined from the measured data using two different methods: (1) from the measured flow depth and channel slope (depth-slope method), and (2) by fitting the logarithmic law (log law) to the measured velocity profile. The results were used to examine the effect of soil erosion depth on the fluid velocity field over the soil sample and the local bed shear stress. Test samples of Nora Moody clay with a

range of unconfined compressive strength values were prepared by varying the water content. The samples were placed in a sediment recess in the tilting flume and eroded under a steady, uniform flow condition. The measured erosion-rate-versus-shear-stress curves were used to investigate the effects of soil unconfined compressive strength on the critical shear stress and soil erosion rates.

## 1.4 Organization of Report

The report begins with a literature review of previous studies on EFA devices and soil erosion testing. The experimental equipment and methods are then described, including the PIV system, PIV data processing and calibration methods, soil sample preparation and geotechnical laboratory testing, and soil erosion testing in the tilting flume. The experimental results on soil erosion will then be presented, followed by the measurement of the bed shear stress using the depth-slope method and the logarithmic law method. The results for the fixed gravel bed are presented first, including a new procedure for finding the bed shear stress using the log law, followed by the results for the clay bed. A discussion of the results will follow to compare the findings in this study with previous studies. Conclusions are then drawn on how the EFA device used in this study may improve upon existing devices, and how the modified log-law method developed may produce more consistent bed shear stress estimates over a rough bed. Last, recommendations for future research are given.

# 2. BACKGROUND AND LITERATURE REVIEW

## 2.1 Introduction

Scour is a result of fluid stresses from the flow being applied to the sediment bed in a river or stream. When soil erosion occurs, it is because the fluid stresses that are being applied to the bed by the flowing water exceeds the resisting strength of the soil. Scour in cohesive soils is believed to be slower than in cohesionless soils. Cohesive soils have soil properties and erodibility that can differ greatly from cohesionless soils. The effects of soil eroding in blocks, chunks, or non-uniformly are just some of the ways cohesive soils may behave. Many studies have been conducted to investigate the erosion processes of cohesive soils, but our understanding is still far from complete. This chapter gives a summary of previous studies that are directly related to the present study.

## 2.2 Erosion Function Apparatus

Cohesive soils erode differently from cohesionless soils. Cohesive soils generally erode more slowly than cohesionless soils, even though their erosion depths at equilibrium conditions may be similar (Arneson et al., 2012). The scour depth that may take a cohesionless soil to reach in one flood could take several flood events to develop for a cohesive soil.

The bridge scour that may develop in a flowing stream depends on many factors, including the discharge, soil properties, and site characteristics such as bridge crossing layout. The HEC-18 document (Arneson et al., 2012) is the procedure commonly used by practicing engineers to evaluate scour at bridges in the United States. Of the different types of scouring, contraction scour is most relevant to the present study. To predict clear water scour in a long contraction, the effect of local scour around piers and abutments and the effect of sediment transport into the contracted section may be ignored. Under these simplifying assumptions, scour depth would increase until the bed shear stress is equal to the critical shear stress of the bed materials. Hence, a soil erosion function can be used with the calculated bed shear stress to compute the contraction scour depth as a function of time by increasing the flow depth in the contraction in a stepwise manner. In this simplified model, the equilibrium scour depth is directly related to the critical shear stress, and the time to reach equilibrium scour depth to the soil erosion rate. The latter is typically modeled as a function of the fluid shear stress. Ting and Kidd (2022) applied this method to compute the history of contraction scour at the SD 37 bridges over the James River in South Dakota for selected flooding events from 1950 to 2017.

The objective of this study is to develop a working, yet cost-effective, laboratory method to measure the erosion rates of cohesive soils. Reliable measurements of soil erosion rates are imperative for accurate prediction of the scour depth that would develop in a period. Briaud et al. (2001a) developed the erosion function apparatus (EFA) to measure the erosion rates of cohesive and cohesionless soils. The apparatus was designed to test soil samples taken from a thin-walled Shelby tube, 76.2 mm outside diameter. Briaud et al. (2001b) incorporated the EFA into a new procedure called the scour rate in cohesive soils (SRICOS) method to predict the time development of scour at bridges using site-specific measurements of soil erosion rates and a measured or constructed hydrograph. Thus, the SRICOS method can predict not only the equilibrium scour depth but also the time history of scour.

The EFA utilizes a steady flow through a water tunnel with smooth walls. A thin-walled tube is attached to the floor of the water tunnel and a piston driven by a stepping motor is used to push the soil sample 1 mm into the flow initially. The soil sample is pushed another 1 mm into the water tunnel after the protruded soil is eroded or after one hour of flow, whichever comes first. This procedure is repeated with different flow velocities to create a curve of soil erosion rate versus applied bed shear stress.

Briaud et al. (2001a) found no clear relationship between soil erodibility and soil properties including grain size, undrained shear stress, and plasticity index. Therefore, the erosion resistance of cohesive soils cannot be determined reliably based on the measured soil properties. Soil samples must be collected from bridge sites and tested in an EFA type apparatus to measure the soil critical shear stress and erosion rate.

The advantages of the EFA are that the erodibility of soils at a given site and from a specific depth can be measured using relatively undisturbed samples, and the results can be used in conjunction with the SRICOS method to predict the time history of scour. A main disadvantage of the EFA setup is deciding when to advance the soil sample and how far the sample should protrude into the flow. Since cohesive soils erode non-uniformly and develop an irregular surface while being eroded, deciding when to advance the soil sample is nontrivial and often subjective, which may produce inconsistent test results. Experimental uncertainty is also introduced by using the Moody Chart or Colebrook equation to estimate the bed shear stress acting on the soil sample.

Improvements to the EFA have been made by other researchers to reduce measurement uncertainties. Shan et al. (2012) developed an ex-situ scour testing device (ESTD), which uses a direct force gauge (DFG) to measure the forces that are exerted on the soil sample, thus eliminating the need to estimate the fluid shear stress using the Moody chart originally developed for pipe flows. In addition, a moving belt and a water pump are used to generate a logarithmic velocity profile in the water tunnel. The soil specimen is mounted on a sensor disk, whose motion is controlled by the DFG, and automatically advanced to maintain a constant shear stress to produce more consistent measurements of soil erosion rate. The design of the ESTD allows for more accurate and consistent measurements of the applied bed shear stress and soil erosion rates under conditions that mimic open-channel flows. However, the ESTD has the same drawbacks as other EFA devices in that the fluid stresses acting on the eroding sample can vary significantly during a test period as the sample erodes non-uniformly, which would complicate the relationship between the measured soil erosion rate and bed shear stress.

Cohesive soil develops a rough surface as it erodes. This rough surface can experience varying local fluid stresses. Crowley et al. (2012a, b) used the sediment erosion rate flume (SERF) to conduct an experimental investigation of different methods for estimating the bed shear stress in a flume-type erosion rate testing device. The SERF was equipped with a shear stress-measuring instrument that can measure shear stress directly. Pressure drops across the soil sample were also measured to estimate the bed shear stress. Their results showed that direct shear stress measurements closely corresponded to shear stress estimates obtained using the Colebrook equation, but measurements of pressure drop across the soil sample underestimated the applied shear stresses. The pressure differential between the upstream and downstream sides of the test area did not change substantially as the soil sample was eroded. Therefore, the bed shear stress cannot be calculated reliably from pressure measurements.

## 2.3 Soil Properties

Soil properties affect the erosion rate and erosion pattern of a soil specimen. Straub and Over (2010) used the EFA to obtain the erosion-rate-versus-shear stress curves of soil samples collected from bridge sites in Illinois. They also conducted laboratory testing on the soil samples to measure the common geotechnical properties. They computed the coefficients of determination of individual soil erosion parameters with the soil properties. They found a strong correlation between the soil critical shear stress and unconfined compressive strength. They also used the SRICOS-EFA method to compute the equilibrium scour depth in pier and contraction scour for the 100- and 500-year floods. They found that the HEC-18 method predicted larger scour depths compared with the SRICOS-EFA method.

Straub and Over (2010) studied the relationship between soil erosion rate and excess shear stress given by the following equation:

$$\dot{z} = a(\tau - \tau_c)^b \tag{2.1}$$

In Eq. (2.1), $\tau_c$ is the critical shear stress and $a$ and $b$ are empirical constants. The equation was fitted to measurements of soil erosion rate and bed shear stress for soil samples collected from bridge sites in Illinois to determine the values of $\tau_c$ and the values of the coefficients $a$ and $b$. Their results showed a linear relationship between $\tau_c$ and the natural logarithm of the unconfined compressive strength, $Q_u$, given by:

$$\tau_c = 5.098 \ln(Q_u) + 10.01 \tag{2.2}$$

where $\tau_c$ is measured in Pascals and $Q_u$ in tons/ft$^2$. Eq. (2.2) has a coefficient of determination ($R^2$) of 0.95. Only weak correlation was found between the coefficient $a$ and the unconfined compressive strength, but the exponent $b$ can be related to $Q_u$ by:

$$b = 1.089 Q_u^{-0.353} \tag{2.3}$$

with an $R^2$ value of 0.61.

Shan et al. (2015) prepared cohesive soil specimens with different percentages of clay, silt, and non-uniform sand and a range of water contents for testing using the ESTD. They found a weaker correlation between the measured critical shear stress and unconfined compressive strength compared with the field samples tested by Straub and Over (2010). They developed the following relationships for $\tau_c$ and $a$ in Eq. (2.1):

$$\tau_c = 0.07 \left(\frac{W}{F}\right)^{-2.0} PI^{1.3} Q_u^{0.4} \tag{2.4}$$

$$a = (Q_u)^{-1.0} PI^{-1.1} \tag{2.5}$$

where $W$ is water content, $F$ is percent particles finer than 0.075 mm, $PI$ is plasticity index, and $Q_u$ is unconfined compressive strength of the soil. A constant of 1.8 for $b$ was found to produce the best fit to their measured data. Eq. (2.4) underpredicted the critical shear stress data from Straub and Over (2010). With $b$ equal to 1.8 and $\tau_c$ and $a$ given by Eq. (2.4) and (2.5), Eq. (2.1) was found to over-predict the erosion rate data from Straub and Over (2010)

# 3. METHODS AND PROCEDURES

## 3.1 Introduction

This chapter describes the materials and procedures used in the laboratory experiments. All the experiments were conducted at South Dakota State University (SDSU). Soil properties were measured in the Geotechnical Engineering Laboratory while the flume tests were conducted in the Fluid Mechanics Laboratory. ASTM standard procedures were followed in determining the soil properties.

## 3.2 Erosion Test Soil Specimen Preparation Procedure

Soil specimen preparation was conducted in the Geotechnical Engineering Laboratory before the samples were transported to the Fluid Mechanics Laboratory for erosion testing in the hydraulic channel.

1. About 1.5 gallons of mostly dry soil were taken from the storage bins labeled “Nora Moody Clay” in the Geotechnical Engineering Laboratory.
2. The soil was placed in a metal container.

**Figure 3.1** Dry soil in metal container before preparation

3. Water was blended evenly into the dry soil using a spray bottle while soil clumps were broken apart.
4. The process continued until there were no clumps big enough to be retained on a No. 4 sieve (4.75 mm).
5. When the soil was mixed to a consistency that was visually moistened. The container was covered, and sealed, in a plastic bag to ensure that the soil became uniformly hydrated for the erosion tests.

**Figure 3.2** Hydrated soil

6. After at least 24 hours the soil was mixed again to ensure uniform hydration.
7. The well mixed and hydrated soil was scooped and compacted in a 4-inch diameter proctor mold following the ASTM D 698 – 91 procedure.

**Figure 3.3** Rammer (left) and mold (right) used to compact soil

8. The soil was filled 1/3 of the way then compacted using a hand-powered rammer.

**Figure 3.4** Layer of soil before being compacted

9. Another layer of soil was added, then compacted using the same number of blows with the rammer.
10. The third layer was filled to the brim of the proctor mold then compacted using the same number of blows as the two layers below it.

**Figure 3.5** Specimen after full compaction effort

11. The soil specimen was then extracted from the proctor mold using a jack lift.


**Figure 3.6** Jack used to extract specimen from Proctor mold

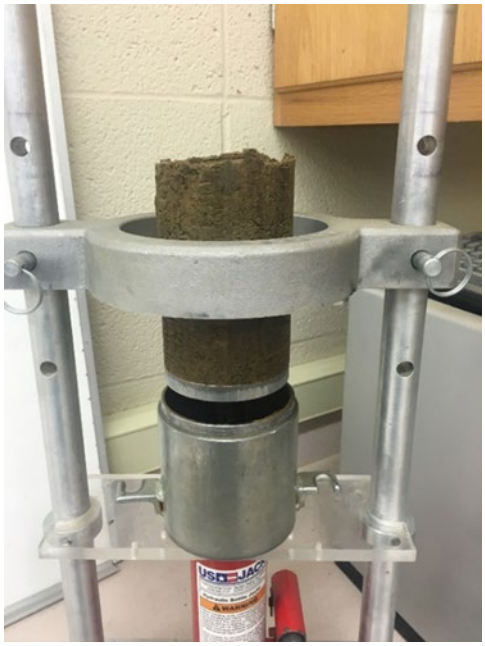

**Figure 3.7** Specimen being extracted from Proctor mold

12. A duplicate soil specimen was prepared from the same batch of soil following the same procedures as described in steps 7-11.
13. Each cylindrical soil specimen was trimmed to a diameter of 2.75 inches while maintaining the same height.

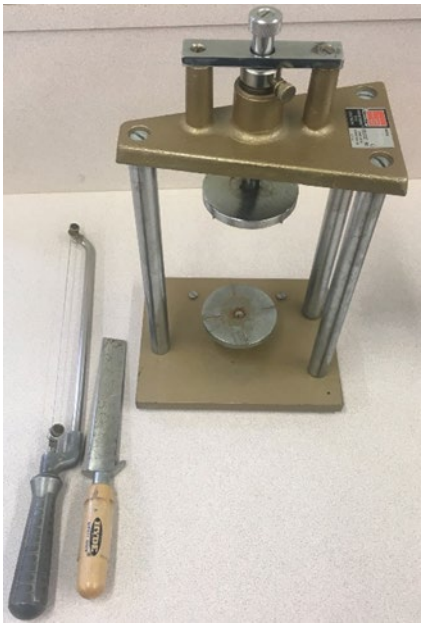

**Figure 3.8** Device and tools used to trim soil specimen

14. Representative trimmings from each sample were weighed in a tin container and placed in an oven to measure the moisture content.

$$w(\%) = \frac{M_{cws} - M_{cs}}{M_{cs} - M_c} \qquad (3.1)$$

where $M_c$ is the mass of container, g; $M_{cs}$ is the mass of the container plus dry soil, g; $M_{cws}$= mass of the container plus wet soil, g; and $w$ is the moisture content of the trimmings, %.

**Table 3.1** Sample results of moisture content of soil specimen's trimmings used for unconfined compressive strength test (A1) and flume test (A2), and of the specimen after the unconfined compressive strength test

| A1: Unconfined Compressive Test Trimmings | | A2: Flume Test Trimmings | | Unconfined Compressive Test Specimen after being tested | |
|---|---|---|---|---|---|
| $M_c$ (g) | 3.63 | $M_c$ (g) | 3.6 | $M_c$ (g) | 4.33 |
| $M_{cs}$ (g) | 122.27 | $M_{cs}$ (g) | 123.48 | $M_{cs}$ (g) | 998.24 |
| $M_{cws}$ (g) | 141.23 | $M_{cws}$ (g) | 143.23 | $M_{cws}$ (g) | 1156.42 |
| $w$ | 15.98% | $w$ | 16.47% | w | 15.91% |

15. One soil sample was stored in a cylindrical metal container and sealed in a Ziploc bag for transport to the Fluid Mechanics Laboratory.

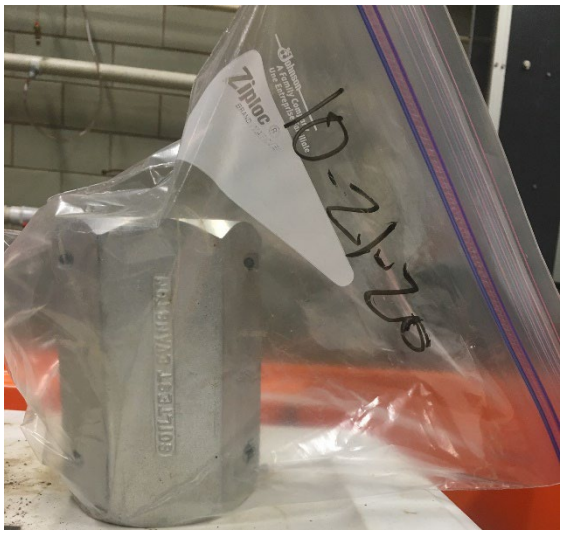


**Figure 3.9** Soil specimen in sealed container ready for transport

16. The other specimen had its initial height ($h_0$) and diameter ($D$) measured. If the $h_0/D$ ratio was > 2 then an unconfined compressive strength test was conducted.


**Figure 3.10** Specimen tested for unconfined compressive strength

17. The unconfined compressive strength machine measures the deflection ($\Delta L$) and resistance (lbf) of the soil specimen (ASTM D 2166-91).
18. A video was taken of the display of the soil testing machine and the video-recorded data was manually entered into a spreadsheet to calculate the unconfined compressive strength of the soil.

**Table 3.2** 2 Unconfined compressive strength test sample results in$^2$

| Raw Data | | | | | | |
|---|---|---|---|---|---|---|
| Vertical Dial Reading (in) | Load Dial (lbs) | Sample Deformation, $\Delta L$ (in) | Unit Strain ($\Delta L/Lo$) | Area Correction Factor (1-$\varepsilon$) | Corrected Area, A' (in$^2$) | Sample Stress (lb/ in$^2$) |
| 0 | 0 | 0 | 0.000% | 1.0000 | 5.940 | 0.000 |
| 0.006 | 0 | 0.006 | 0.101% | 0.9990 | 5.946 | 0.000 |
| 0.017 | 0 | 0.017 | 0.286% | 0.9971 | 5.957 | 0.000 |
| 0.025 | 2 | 0.025 | 0.421% | 0.9958 | 5.965 | 0.335 |
| 0.034 | 5 | 0.034 | 0.573% | 0.9943 | 5.974 | 0.837 |
| 0.041 | 12 | 0.041 | 0.691% | 0.9931 | 5.981 | 2.006 |
| 0.048 | 20 | 0.048 | 0.808% | 0.9919 | 5.988 | 3.340 |
| 0.056 | 29 | 0.056 | 0.943% | 0.9906 | 5.996 | 4.836 |
| 0.064 | 40 | 0.064 | 1.078% | 0.9892 | 6.004 | 6.662 |
| 0.072 | 56 | 0.072 | 1.213% | 0.9879 | 6.012 | 9.314 |
| 0.08 | 73 | 0.08 | 1.347% | 0.9865 | 6.021 | 12.125 |
| 0.086 | 89 | 0.086 | 1.448% | 0.9855 | 6.027 | 14.767 |
| 0.091 | 101 | 0.091 | 1.533% | 0.9847 | 6.032 | 16.744 |
| 0.097 | 116 | 0.097 | 1.634% | 0.9837 | 6.038 | 19.211 |
| 0.103 | 132 | 0.103 | 1.735% | 0.9827 | 6.044 | 21.838 |
| 0.108 | 149 | 0.108 | 1.819% | 0.9818 | 6.050 | 24.630 |
| 0.115 | 168 | 0.115 | 1.937% | 0.9806 | 6.057 | 27.737 |
| 0.121 | 182 | 0.121 | 2.038% | 0.9796 | 6.063 | 30.017 |
| 0.127 | 193 | 0.127 | 2.139% | 0.9786 | 6.069 | 31.799 |
| 0.133 | 204 | 0.133 | 2.240% | 0.9776 | 6.076 | 33.577 |
| 0.139 | 213 | 0.139 | 2.341% | 0.9766 | 6.082 | 35.022 |
| 0.146 | 221 | 0.146 | 2.459% | 0.9754 | 6.089 | 36.293 |
| 0.162 | 234 | 0.162 | 2.728% | 0.9727 | 6.106 | 38.322 |
| 0.176 | 241 | 0.176 | 2.964% | 0.9704 | 6.121 | 39.373 |
| 0.185 | 242 | 0.185 | 3.116% | 0.9688 | 6.131 | 39.474 |
| 0.192 | 241 | 0.192 | 3.234% | 0.9677 | 6.138 | 39.263 |

where,

Sample Deformation, $\Delta L = L_0 - L_i$ (3.2)

$\varepsilon$ (%) $= \frac{\Delta L}{L_0} * 100$ (3.3)

Area Correction Factor = 1-$\varepsilon$ (3.4)

Corrected Area = Initial Area/Area Correction Factor (3.5)

Sample Stress (psi) = Load Dial Reading/Corrected Area (3.6)

$\Delta L$ = Difference from the initial length
(Using the vertical dial on Unconfined Compressive Test Device)

$L_0$ = Initial Length
(Using tape measure)

$L_i$ = Length at load reading

$$L_i = L_0 - \Delta L$$

$\varepsilon$ = Unit Strain (%)

$$\varepsilon = \Delta L / L_0$$

Sample calculations for highlighted row in Table 3.2:

$L_0$ = 5.9375 in

Initial Area = 5.9 $in^2$

$\varepsilon = \frac{\Delta L}{L_0} * 100 == \frac{0.185}{5.9375} * 100\ \% = 3.116\%$

Area Correction Factor = 1 – $\varepsilon$ = 1- 0.03116 = 0.9688

Corrected Area = $\frac{Initial\ Area}{Area\ Correction\ Factor} = \frac{5.9\ in^2}{0.9688} = 6.131\ in^2$

Sample Stress = $\frac{Load\ Dial\ Reading}{Corrected\ Area} = \frac{242\ lb}{6.131\ in^2} = 10.687$ psi

A plot was made using the axial stress vs unit strain to show the specimen's point of failure.

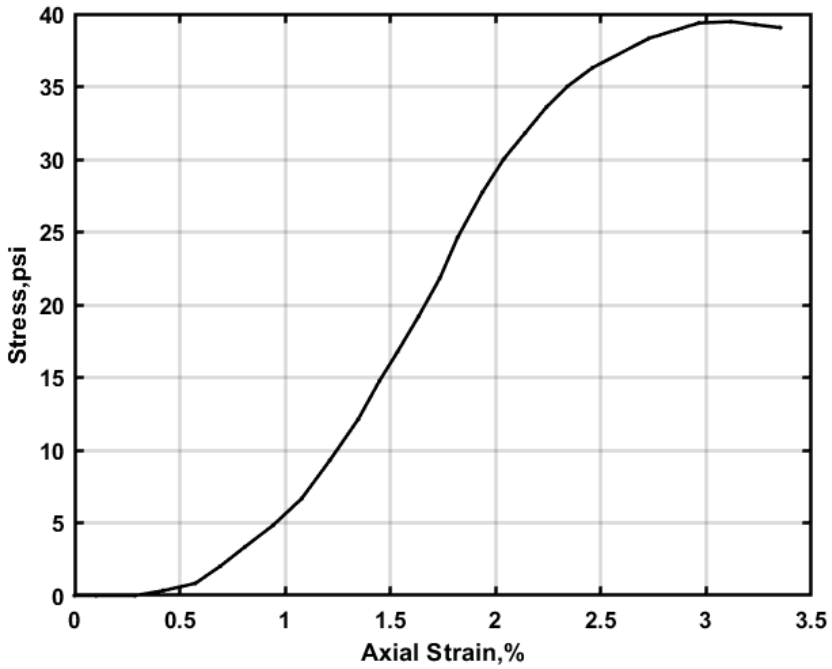


**Figure 3.11** Stress vs axial strain for soil specimen

The maximum measured axial stress was taken to be the unconfined compressive strength of the soil, and the undrained shear strength of the soil specimen was estimated as half the unconfined compressive strength of the soil specimen. Therefore, if $Q_u$ is 39.474 psi then $C_u$ is 19.74 psi; where $Q_u$ is the unconfined compressive strength, psi; and $C_u$ is the estimated undrained shear strength, psi.

19. After the soil specimen failed in the unconfined compressive strength machine, it was weighed and placed in the oven to measure the moisture content. Moisture content was measured to verify the moisture content on the soil trimmings.

**Figure 3.12** Soil specimen after failure

20. The specimen that was put aside in the sealed container was taken to the Fluid Mechanics Laboratory for soil erosion testing in the hydraulic channel.

The unconfined compressive strength data were summarized and plotted in Figure 3.13. This plot shows there is a clear trend that the unconfined compressive strength of a prepared soil specimen can be predicted by the measured water content.

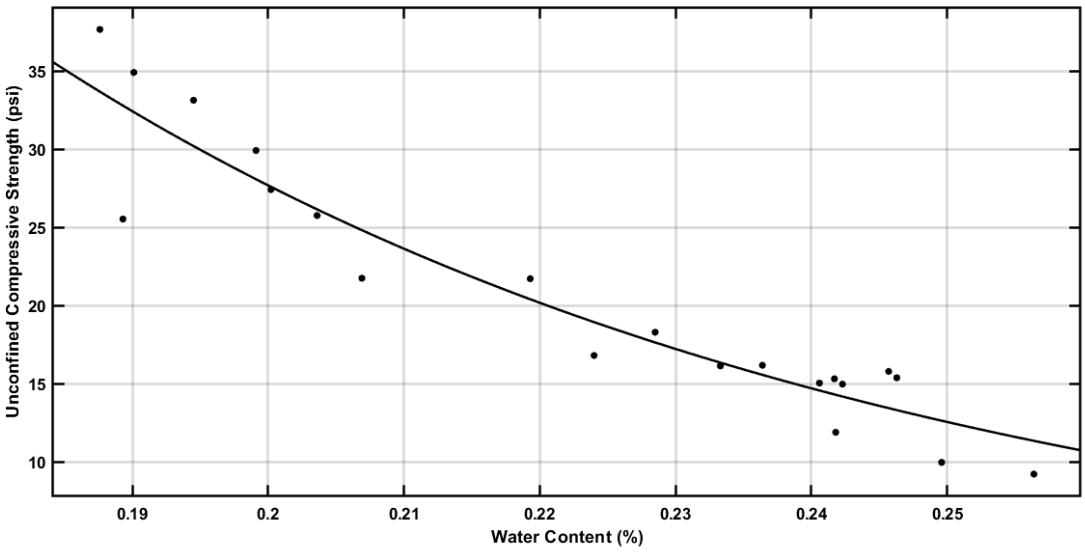


**Figure 3.13** Unconfined compressive strength vs. water content of soil specimens

The best fit line to predict the unconfined compressive strength of the soil samples was an exponential model with an $R^2$ of 0.9028 and an RMSE of 2.636.

$$Q_u = 708.5e^{-16.18w}$$

## 3.3 Soil Particle Size Distribution Procedure

A laboratory experiment was conducted in the Geotechnical Engineering Laboratory to determine the particle size distribution of the Nora Moody clay used in the soil erosion tests conducted in the A-8 hydraulic channel. The procedure followed ASTM D422 – 63: Standard Test method for Particle-Size Analysis of Soils.

1. 50 grams of soil was taken from storage bins labeled "Nora Moody Clay" in the Geotechnical Engineering Laboratory. The soil was dried in an oven and the dry mass was measured.
2. The dry soil was dispersed on the No. 10 sieve (2.00 mm) to determine the percent of soil coarser than 2.0 mm. 100% of the soil sample was finer than the No. 10 Sieve.
3. The portion of soil sample passing the No. 10 sieve was transported to a 250 mL beaker.
4. A solution of 125 mL of sodium hexametaphosphate with a concentration of 40 g of sodium hexametaphosphate/liter of distilled or demineralized water (40 g/L) was poured into a 250 mL beaker, covering the soil sample. Soil slurry was stirred until the soil was thoroughly wetted. The mixture was soaked for at least 16 hours.
5. After the soaking period, the slurry was transferred to a dispersion cup (A). The soil residue in the beaker was washed into the dispersion cup using distilled water from a spray bottle filling the cup until it was more than half full.

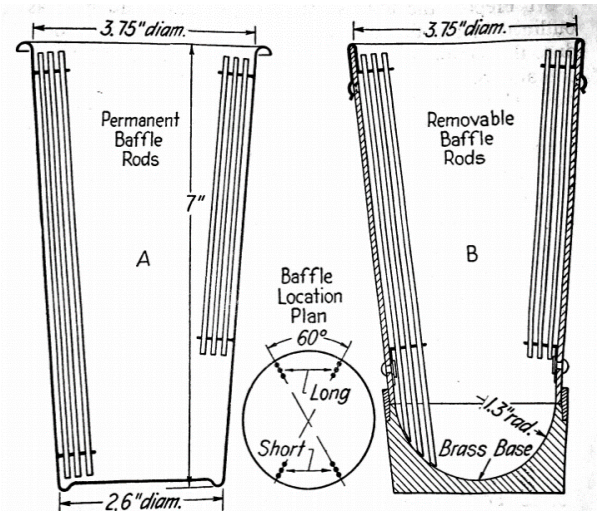


**Figure 3.14** Dispersion cup used to mix soil slurry (A)

6. The soil slurry was then vigorously dispersed using a Hamilton Beach stirring apparatus with a round stirring paddle (a). Soil was stirred for one minute.


**Figure 3.15** Hamilton Beach dispersion device used to thoroughly mix soil slurry

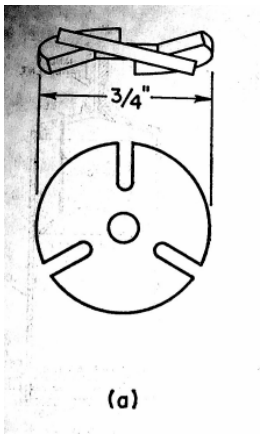


**Figure 3.16** Detail of stirring paddle used

7. Immediately after the soil slurry was dispersed in the mixing apparatus, it was transferred to a 1,000 mL glass sedimentation cylinder. The mixing cup was rinsed using a spray bottle filled with distilled water. The glass cylinder was filled to the 1,000 mL mark with distilled water.
8. Using a rubber stopper at the open end, the glass cylinder was turned upside down and back for one minute at a rate of one turn per second.
9. The glass cylinder was set in a convenient location.

10. A 151H hydrometer was used to take hydrometer readings at 0.5, 2, 5, 15, 30, 60, 120, 250, 500, and 1,440 minutes from the start of sedimentation. The temperature of soil-water slurry in the cylinder was also taken at each time interval.

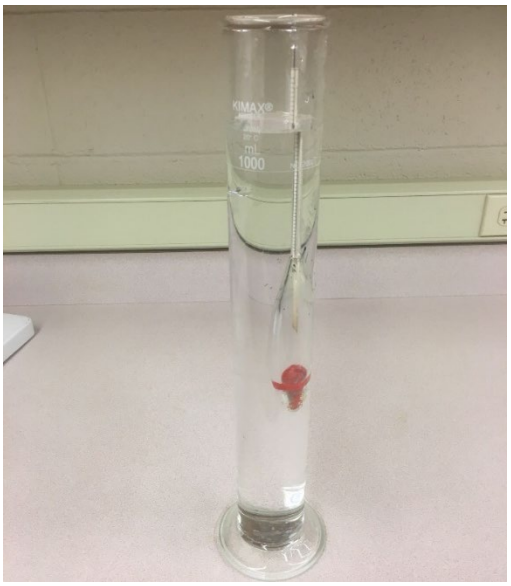


**Figure 3.17** Glass sedimentation cylinder with 151H hydrometer

11. When a reading was taken, the 151H hydrometer was carefully inserted into the glass cylinder for about 20–25 seconds before the reading time at the approximate depth it would settle at. For accuracy, readings were taken at the top of the meniscus formed by the suspension around the stem of the hydrometer.
12. After the reading, R, was taken, the hydrometer was removed and placed in a graduated cylinder of clean distilled water until the next reading.
13. After taking the final hydrometer reading, the soil suspension was transferred to a No. 200 sieve (75-µm) and washed with tap water until the wash water was clear.
14. The material retained on the No. 200 sieve was transferred to a suitable container and dried in the oven at 230°F ± 9°F (110°C ± 5°C).
15. The results were recorded in a table, and the percentage of soil remaining in suspension (percent finer than) and diameter of particles (in mm) corresponding to that percentage indicated by the hydrometer reading were calculated using Stoke's Law.

**Table 3.3** Hydrometer 151H sample results table

| Hydrometer 151H | | | | | | |
|---|---|---|---|---|---|---|
| Hydrometer Readings | | | | Mass of Dry Soil, W (g) | | 56.95 |
| Time (min) | Temp (°C) | $G_1$ | R | *L* (cm) Table 2 | P (%) | D (mm) |
| 0.5 | 21 | 0.997992 | 1.033 | 7.6 | 95.53 | 0.05033 |
| 2 | 21 | 0.997992 | 1.026 | 9.4 | 76.43 | 0.02799 |
| 5 | 21 | 0.997992 | 1.022 | 10.5 | 65.51 | 0.01871 |
| 15 | 21 | 0.997992 | 1.019 | 11.3 | 57.33 | 0.01121 |
| 30 | 21.5 | 0.997882 | 1.017 | 11.8 | 52.17 | 0.00805 |
| 60 | 21.5 | 0.997882 | 1.016 | 12.1 | 49.44 | 0.00576 |
| 120 | 22 | 0.99777 | 1.015 | 12.3 | 47.01 | 0.00409 |
| 250 | 23 | 0.997538 | 1.0135 | 12.75 | 43.55 | 0.00285 |
| 500 | 23 | 0.997538 | 1.013 | 12.9 | 42.18 | 0.00203 |
| 1440 | 22.5 | 0.997655 | 1.012 | 13.4 | 39.14 | 0.00122 |

16. The hydrometer readings were taken recording the time from start (minutes), temperature of soil-water suspension (°C), and the hydrometer reading (R).
17. The percentage of soil remaining in suspension (P) at the level where the hydrometer is measuring (R), the density of the soil-water suspension at the specific time was calculated as:

$$P = \left[\left(\frac{100{,}000}{W}\right) * \frac{G}{(G-G_1)}\right](R - G_1) \qquad (3.7)$$

where *W* is the oven-dry mass of soil sample recorded before test, g; *G* is the specific gravity of soil particles, 2.7992; $G_1$ is the specific gravity of liquid in which soil particles are suspended.

18. The effective depth, *L* (cm), was taken from Table 2, in ASTM D 422, pertaining to the actual hydrometer reading that was recorded.
19. The diameter of the soil particle corresponding to the percentage indicated by a hydrometer reading was calculated using Stoke's Law. This assumes that if a particle of the calculated diameter was at the surface of the suspension at the beginning of sedimentation, it would have settled to the level that the hydrometer density measurement was read. The diameter of the soil particle in suspension at the time of the reading was calculated as:

$$D = K\sqrt{\frac{L}{t}} \qquad (3.8)$$

where *D* is the diameter of soil particle, mm; *K* is the constant depending on the temperature of the suspension and specific gravity of the soil sample (the *K* values were taken from Table 3 in ASTM D 422); *L* is the effective depth, cm (found from Table 2); *t* is the time from the beginning of sedimentation to the recorded reading, min.

20. After the percent finer than, P, and diameter of particles, *D*, were calculated for each time interval and No. 200 sieve, the results were plotted on a percent finer than versus particle diameter chart.

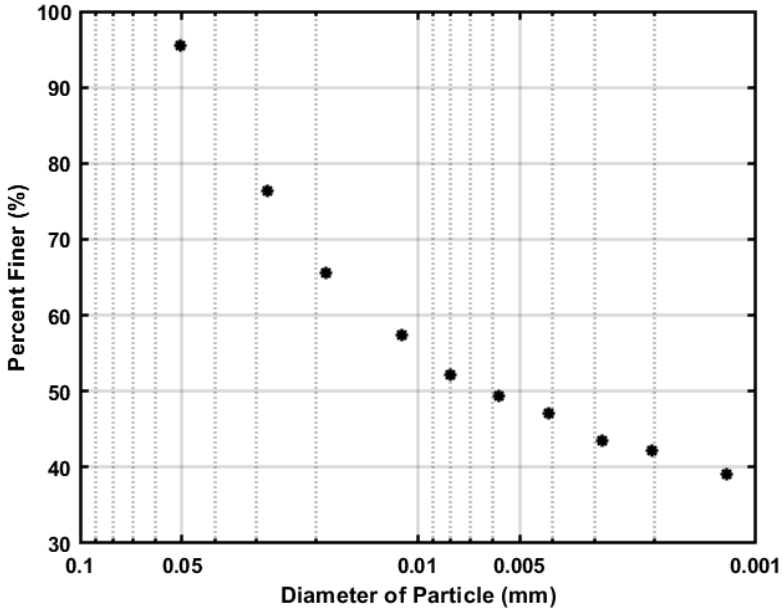


**Figure 3.18** Example plot of particle size analysis results

Table 3.4 displays the geotechnical soil properties that were held constant in the present study while the water content, unconfined compressive strength, and estimated undrained shear strength were varied.

**Table 3.4** Measured soil properties

| Soil Property | |
|---|---|
| Liquid Limit (LL) | 37% |
| Plastic Limit (PL) | 24% |
| Plasticity Index (PI) | 13% |
| Percent Finer than 0.075 mm | > 95% |
| $d_{50}$ (mm) | 0.006 |

## 3.4 Sieve Analysis on Fixed Gravel Bed in A-8 Hydraulic Channel

A sieve analysis was conducted on the gravel used to construct the rough bed in the hydraulic channel used for the soil erosion tests. The ASTM D 422 – 63: Standard Test Method for Particle-Size Analysis was followed for measuring the gravel size distribution.

The following sieve sizes were used: 3/8" (9.5 mm), 0.265" (6.7 mm), ¼" (6.3 mm), No. 3½ (5.6 mm), No. 4 (4.76 mm), No. 5 (4 mm), No. 6 (3.36 mm), No. 7 (2.8 mm), and No. 8 (2.36 mm).

1. The mass of each sieve was recorded, in grams, using a digital scale with a precision of 0.01 grams.
2. The total mass of the gravel, not being greater than about 1,500 grams, used in each trial was recorded.
3. The sieves were stacked in order, with the largest sieve opening at the top, and the smallest at the bottom. A pan was placed under all the sieves to collect the fine materials.
4. The gravel sample was dispersed on the top of the sieve stack.
5. The stack of sieves was placed in a mechanical shaker and shook for 10 minutes.
6. After the 10-minute shaking period, the sieves were removed from the shaker.
7. Each sieve's mass with the gravel that was retained on it was recorded.
8. The mass of the gravel retained on each sieve was found by subtracting the sieve mass from the sieve plus gravel mass.
9. Each mass was recorded on a data sheet and the percent retained and percent passing was calculated.

$$Percent\ Retained(\%) = \frac{Mass\ of\ gravel\ retained\ on\ sieve}{Total\ gravel\ mass} * 100 \quad (3.9)$$

$$Percent\ Passing(\%) = 100\% - Cummulative\ Percent\ Retained \quad (3.10)$$

10. A total of five trials were completed. The results of the different trials were then averaged and plotted to determine the $d_{50}$ of the gravel.

**Table 3.5** Average results for sieve analysis with a total soil mass of 8,175.82 grams

| Sieve No. | Sieve Size (mm) | Mass of Sieve Only (g) | Mass of Sieve with Soil (g) | Soil Mass (g) | Percent Retained | Cumulative Percent Retained | Percent Passing |
|---|---|---|---|---|---|---|---|
| 3/8" | 9.5 | 483.66 | 483.66 | 0 | 0.00 | 0.00 | 100.00 |
| 5/16" | 8 | 505.41 | 509.41 | 46.52 | 0.57 | 0.57 | 99.43 |
| 0.265" | 6.7 | 491.25 | 681.76 | 1689.65 | 20.67 | 21.24 | 78.76 |
| 1/4" | 6.3 | 495.67 | 584.87 | 722.07 | 8.83 | 30.07 | 69.93 |
| 3 1/2 | 5.6 | 493.28 | 741.78 | 1731.58 | 21.18 | 51.25 | 48.75 |
| 4 | 4.75 | 466.34 | 664.72 | 1142.48 | 13.97 | 65.22 | 34.78 |
| 5 | 4 | 478.05 | 771.26 | 1382.84 | 16.91 | 82.13 | 17.87 |
| 6 | 3.35 | 474.68 | 673.42 | 766.61 | 9.38 | 91.51 | 8.49 |
| 7 | 2.8 | 460.3 | 608.65 | 463.57 | 5.67 | 97.18 | 2.82 |
| 8 | 2.36 | 459.14 | 516.86 | 145.03 | 1.77 | 98.95 | 1.05 |
| Pan | 0 | 490.4 | 545.52 | 85.47 | 1.05 | 100.00 | 0.00 |

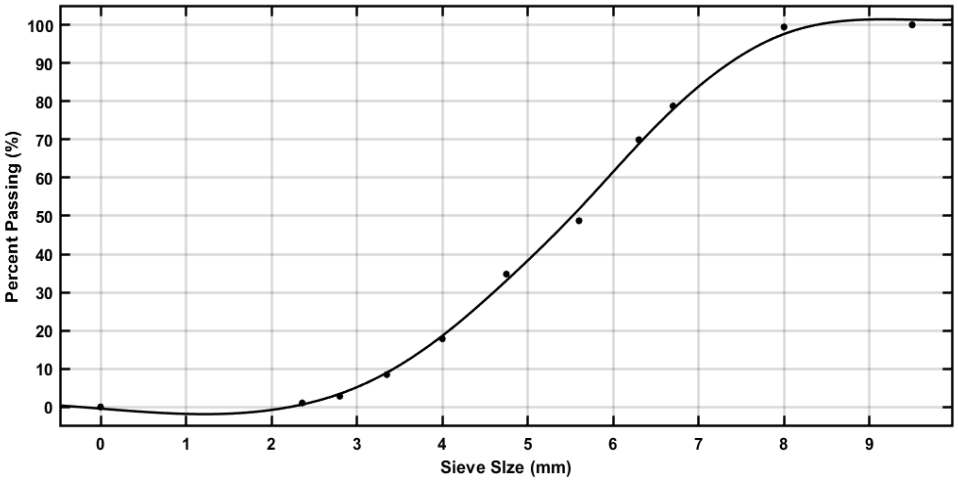


**Figure 3.19** Grain size distribution of gravel

**Table 3.6** Grain size distribution of gravel

| *r* % of particles finer | $d_r$ (mm) |
|---|---|
| 10 | 3.5 |
| 20 | 4.1 |
| 30 | 4.6 |
| 40 | 5.1 |
| 50 | 5.6 |
| 60 | 6.0 |
| 65 | 6.1 |
| 70 | 6.3 |
| 80 | 6.8 |
| 84 | 7.0 |
| 90 | 7.4 |

## 3.5 Soil Erosion Test Procedure in A-8 Hydraulic Channel

The soil erosion tests were conducted in an A-8 hydraulic channel in the Fluid Mechanics Laboratory. The objective was to erode the soil specimen that was prepared in the Geotechnical Engineering Lab, and then relate the erosion rate of the specimen to the measured soil and flow properties.

**Figure 3.20** A-8 hydraulic channel

1. The soil specimen prepared in the Geotechnical Laboratory was trimmed to a height of about 1.5 inches to match the height of the sediment bed recess.

**Figure 3.21** Soil specimen before being placed in hydraulic channel

2. The mass of the trimmed soil specimen was taken, in grams, on a digital scale with 0.01-gram precision prior to the flume test.

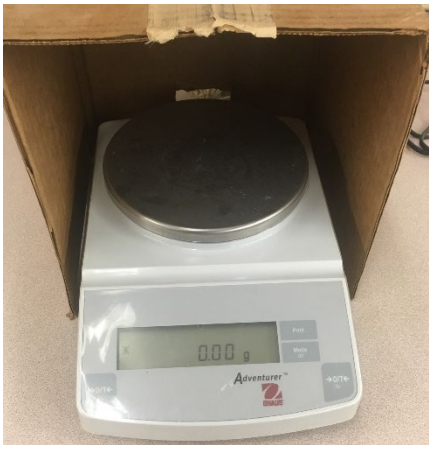


**Figure 3.22** Electronic scale used to measure soil mass

3. The soil sample was placed in an insert in the false bottom installed in the flume. The top of soil sample was set at or slightly above the top of the rock bed.

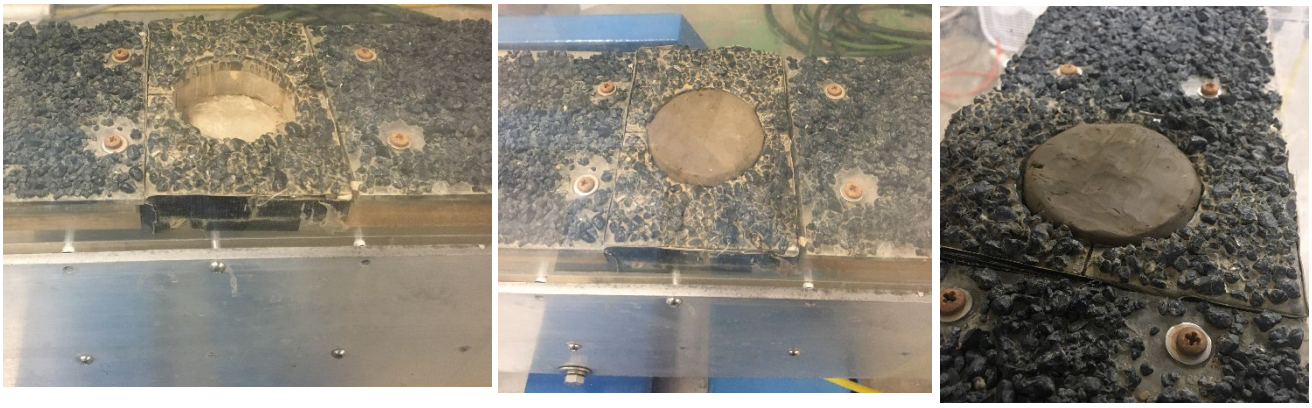

**Figure 3.23** Soil recess in rock bed in A-8 hydraulic channel

4. The flume was set to the maximum flow rate of 0.158 $ft^3/s$ and the desired slope was set using a SmartTool digital inclinometer with a precision of ± 0.1%. The slope was chosen according to the desired bed shear stress to induce erosion.


**Figure 3.24** Slope measuring device

5. A point gage with a precision of ± 0.1 mm was used to record the height of the acrylic sheet where the gravels were adhered. The bottom measurements were taken at the sediment recess and approximately one water depth upstream and downstream.
6. The hydraulic channel flow and a timer were started.

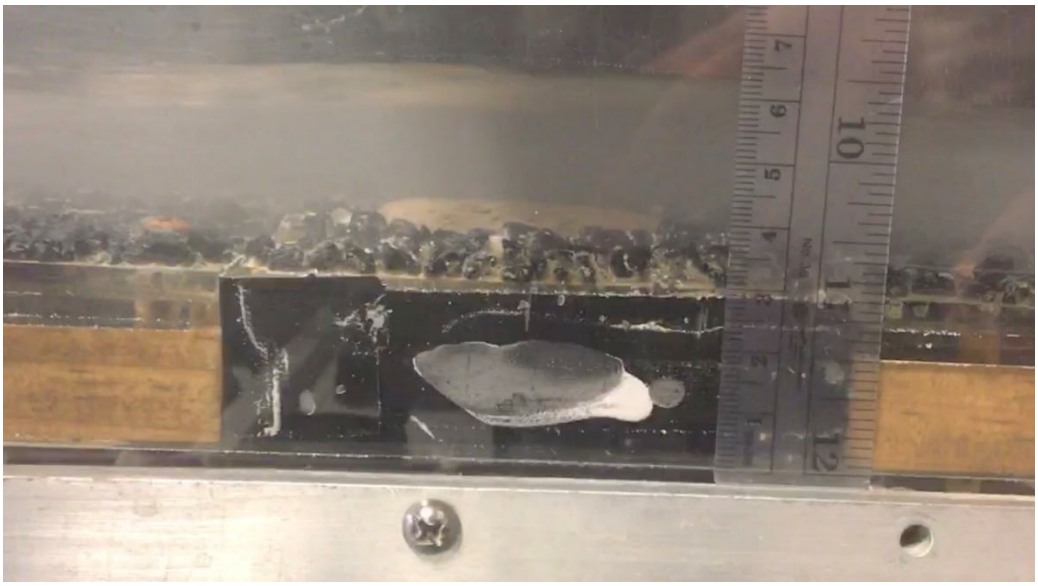

**Figure 3.25** Profile view of test area after steady flow was established

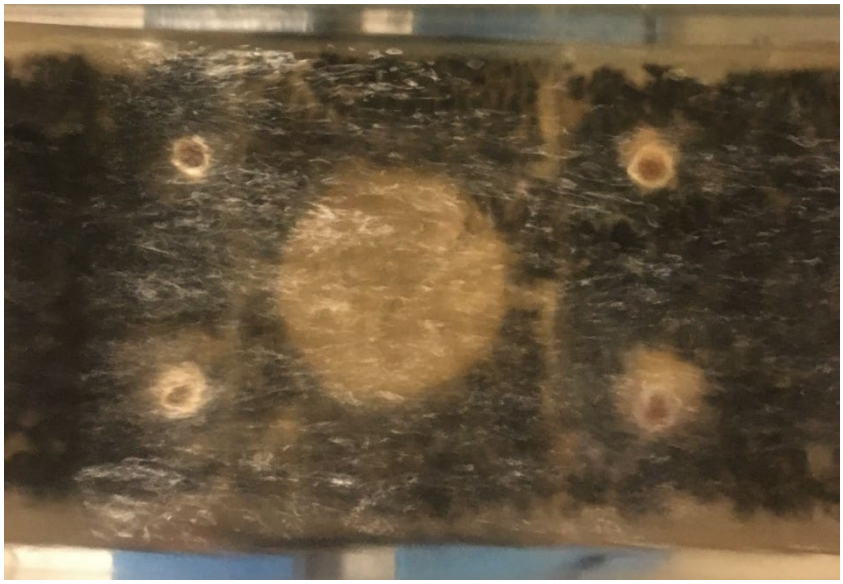

**Figure 3.26** Plan view of test area after steady flow was established

7. The top of water upstream, at the sediment recess, and downstream was measured using a point gage. The water depth was calculated relative to the bottom of the acrylic sheet, using the water height and bed height measured in step 6, and the results were averaged.

$$Y_{Avg} = \frac{Y_{Upstream} + Y_{Downstream} + Y_{Test\ Area}}{3} \tag{3.11}$$

8. Flow through the hydraulic channel was stopped before the soil had visually been eroded below the gravel bed. The soil sample was eroded enough to accurately measure a difference in soil mass but small enough to not significantly change the flow configuration or bed shear stress around the test area; this will be demonstrated in Section 4.1.

**Figure 3.27** Example of soil specimen after being eroded

9. The mass of a tin container ($M_c$) was measured in grams.
10. The sediment recess was removed from the hydraulic channel. The insert was set aside so the soil specimen could be extracted.
11. The eroded sample was extracted from the insert by dumping it into the pre-weighed tin container.
12. The mass of wet soil plus container ($M_{cws}$) was measured using a digital scale with a precision of 0.01 gram.
13. The soil sample and dish were placed in an oven and dried for at least 24 hours.
14. After 24 hours the eroded soil specimen was removed from the oven and cooled for at least 15 minutes.
15. The mass of dry soil plus dish ($M_{cs}$) was measured using an electronic scale.
16. The moisture content of the soil specimen after being eroded was calculated for comparison with the water content before the test.

$$w(\%) = \frac{M_{cws} - M_{cs}}{M_{cs} - M_c} \tag{3.12}$$

17. The difference between the dry mass of the soil before and after the test was considered the amount eroded in the hydraulic channel.

The wet mass of the soil specimen before ($M_{0,\,\mathrm{Wet}}$) and after ($M_{\mathrm{f},\,\mathrm{Wet}}$) erosion, as well as the dry mass after erosion ($M_{\mathrm{f},\,\mathrm{Dry}}$), were recorded. The dry mass of the soil specimen before being eroded ($M_{0,\,\mathrm{Dry}}$) was estimated using the initial moisture content from the specimen's trimmings, which was found in Section 3.2, Step 14.

$$M_{0,Dry} = \frac{M_{0,wet}}{w+1} \tag{3.13}$$

18. The average erosion rate was calculated as:

$$\dot{z} = \frac{l}{t} \tag{3.14}$$

where $\dot{z}$ is the erosion rate (mm/hr), $l$ is the length of the soil sample eroded (mm), and $t$ is the time elapsed (hours).The length $l$ is calculated from the initial height of the soil sample $H_0$ using the percent difference by mass from before and after erosion test.

$$\dot{z} = \frac{H_0 \times Percent\ of\ soil\ eroded}{t} \tag{3.15}$$

where the percent of soil eroded is calculated as:

$$Percent\ of\ soil\ eroded = \frac{M_{0,Dry} - M_{f,Dry}}{M_{0,Dry}} \tag{3.16}$$

## 3.6 Procedure to Determine Bed Shear Stress from Water Depth in A-8 Hydraulic Channel

The procedure used to find the bed shear stress from the measured flow depth in the A-8 Hydraulic Channel is described in this section. The flow discharge rate was measured using the procedure described in Appendix A, and the result was used with the average flow depth measured during each erosion test to calculate the bed shear stress. The flow depth and channel slope were varied in the erosion tests, but the flow rate was kept constant. The measured bed shear stress accounts for side wall correction using the method in Cheng (2011), as well as the estimated porosity of the fixed gravel bed.

The average discharge rate used in the bed shear stress calculations was 0.158 $ft^3/s$. In this method an effective water depth, $h_e$, is estimated using the $d_{50}$ and porosity of the gravel bed. Loosely packed gravel typically has a porosity of about 0.4 (Frings et al., 2011). The void fraction of a single layer of gravel will have a larger porosity. An estimated porosity of $n$ = 0.5 was used since the calculated bed shear stress is insensitive to the porosity of the gravel bed used. As stated earlier, the $d_{50}$ of the gravel bed was 5.6 mm.

The input parameters include the measured discharge, channel slope, and flow depth measured from the base of the gravel.

1. The effective flow depth was calculated as:

$$h_e = h - (1 - n) * \varepsilon \tag{3.17}$$

where $h_e$ is the effective flow depth (m), $n$ is the porosity of the fixed gravel bed (%), and $\varepsilon$ is the effective thickness of the gravel layer taken to be $d_{50}$ = 5.6 mm. The average flow velocity was then determined as:

$$V = \frac{Q}{b * h_e} \tag{3.18}$$

where $b$ is the width of the channel and $Q$ is the flow rate.

2. The bulk hydraulic radius, Reynolds number, and friction factor were calculated as:

$$R_h = \frac{b * h_e}{(b + 2h_e)} \tag{3.19}$$

$$Re = \frac{V * 4R_h}{\nu} \tag{3.20}$$

$$f = \frac{8gR_hS}{V^2} \tag{3.21}$$

where $\nu$ is the kinematic viscosity of water at the measured temperature ($m^2/s$), $R_h$ is the hydraulic radius, $Re$ is the Reynolds Number, and $f$ is the bulk friction factor.

3. The friction factor for the Plexiglas side wall ($f_w$) was calculated as:

$$f_w = 31 * \left[ \left( \ln\left( \frac{1.3 * Re}{f} \right) \right)^{-2.7} \right] \tag{3.22}$$

4. The bed-related friction factor, hydraulic radius, and bed shear stress were calculated as:

$$f_b = f + \frac{2h_e}{b}(f - f_w) \quad (3.23)$$

$$r_b = \frac{f_b}{f} * R_h \quad (3.24)$$

$$\tau_b = \rho g r_b S \quad (3.25)$$

where $f_b$ is the bed-related friction factor, $r_b$ is the bed-related hydraulic radius (m), $S$ is the channel slope (m/m), and $\tau_b$ is the bed-related shear stress (N/m$^2$).

The sidewall-related hydraulic radius and shear stress were also calculated:

$$r_w = \frac{f_w}{f} * R_h \quad (3.26)$$

$$\tau_w = \rho g r_w S \quad (3.27)$$

where $r_w$ is the sidewall-related hydraulic radius (m); and $\tau_w$ is the sidewall-related shear stress (N/m$^2$).

## 3.7 Procedure for PIV measurements in A-8 Hydraulic Channel

Particle image velocimetry (PIV) measurements were taken over the gravel bed and soil sample in the A-8 hydraulic channel. The velocity profile measurements were used to determine the bed shear stress using the logarithmic law. PIV measurements over the soil sample were conducted to investigate the effects of erosion depth on the local bed shear stress.

The PIV system used is manufactured by TSI incorporated. The seeding consisted of latex particles with a mean diameter of 55 μm and a specific gravity of 1.016. The seeding particles were illuminated using a Model IL-105X high-power-LED illuminator manufactured by HARDsoft microprocessor system. The light sheet created by the LED illuminator was directed downward from its mounting position above the test area, as shown in Figure 3.29. Images of the illuminated light sheet were captured using a PowerView Plus 4MP camera (2048 x 2048 pixels, 12-bit intensity dynamic range) equipped with a 105 mm/F 2.8 NIKKOR focal lens. The camera was mounted on the side of the flume, about 20.5 cm away from the side wall, with the field of view (FOV) parallel to the channel slope. The LED and camera were synchronized to capture images of the seeding particles as the LED light was shooting. The time interval between straddle frames was 100 μs and the repetition rate was 7.25 Hz. The maximum FOV was about 34 mm × 34 mm with a spatial resolution of 16 μm/pixel.

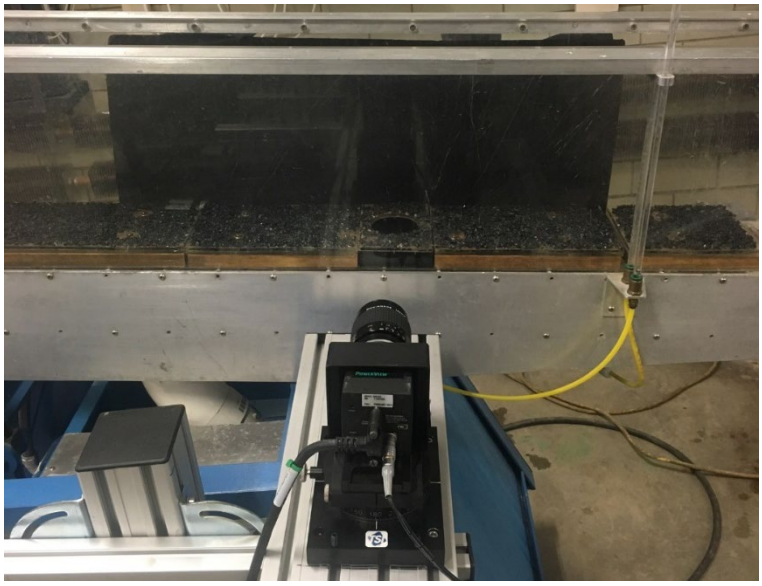

**Figure 3.28** PIV camera setup with gravel bed and sediment recess installed in A-8 Hydraulic Channel

The procedure for PIV measurements were similar for the fixed bed and soil sample, except for the installation of the soil insert. The procedure for the setup of these experiments are as follows:

1. The camera FOV was checked to ensure that the image captured the channel bed and most of the flow depth.
2. The distance from the sidewall to the camera lens was measured.
3. The gravel bed and sediment recess were removed, and a calibration target was placed at the centerline of the channel.

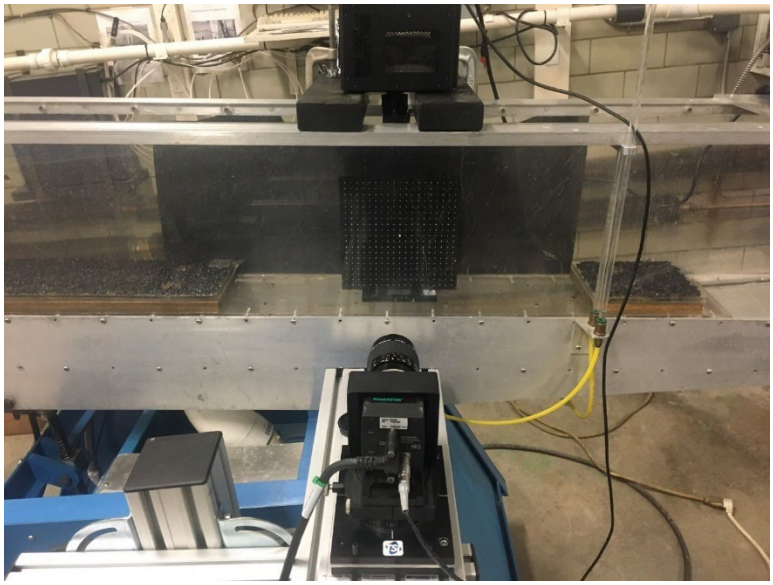

**Figure 3.29** LED illuminator, PIV camera, and calibration target setup

4. The LED illuminator was set on top of the hydraulic channel. A light sheet was generated and projected downward to align with the alignment mirror on top of the calibration target.
5. The pump was started to fill the hydraulic channel for calibration with the target submerged.
6. The PIV camera was focused on the target with the aperture at F2.8.
7. The slope difference between the camera and hydraulic channel was checked using the calibration target and minimized by adjusting the tilt of the camera mount.
8. A calibration image was captured and calibrated using the "Measure" function in the PIV INSIGHT program.
9. The distance between the marker points on the calibration target was measured eight times and averaged (twice along the top, bottom, left, and right side of the image of the calibration target) to determine the calibration factor in mm/pixel.
10. The gravel bed and sediment recess were reinstalled in the channel for the PIV measurements.

# 4. EXPERIMENTAL RESULTS

## 4.1 Soil Erosion Tests

Soil erosion rate testing was conducted in an A-8 hydraulic channel in the Fluid Mechanics Laboratory at South Dakota State University. A gravel bed was constructed by gluing a single layer of fine gravel with a $d_{50}$ of 5.6 mm to acrylic sheets and secured them to the flume floor using metal screws and floor inserts. The fixed gravel bed had a 2.75-inch (69.85 mm) diameter recess for housing a soil sample. The objective of the tests was to determine if there is a direct correlation between the sediment erosion rate and unconfined compressive strength. The turbulent flow created a logarithmic velocity profile over the channel bed, and the fixed gravel increased the bed roughness, which in turn would increase the mean and fluctuating bed shear stress acting on the embedded soil specimen. A rough bed would also have reduced the effect of the soil sample on the flow and maintained a more consistent fluctuating bed shear stress on the soil surface as the sample eroded. Summary tables of the test results are presented in Appendix B.

**Figure 4.1** A-8 hydraulic channel

**Figure 4.2** Soil sample at start of erosion test

The soil sample was trimmed to approximately the same level as the top of the fixed gravel bed in the hydraulic channel. The height of the trimmed sample was about 1.5 inches (38.1 mm), and its diameter was about 2.75 inches (69.85 mm). After its mass was measured, the sample was placed in the sediment recess in the fixed gravel bed. The slope of the channel was adjusted using a digital inclinometer. The flow and a timer were started, and the test was stopped before the soil sample was eroded to the base of the surrounding gravel bed.

**Figure 4.3** Soil sample after erosion test

The eroded soil sample was then extracted from the sediment recess and its wet mass was measured. The soil was dried to determine the dry mass of the sample. The dry mass of the sample before the test was determined from its wet mass before erosion and the measured soil water content (see Section 3.5). The difference between the dry mass before the erosion test and after was used to calculate the average erosion rate as:

$$\dot{z} = \frac{l}{t} \tag{4.1}$$

where $\dot{z}$ is the average erosion rate (mm/hr.), $l$ is the estimated length of the soil sample eroded (mm), and $t$ is the time elapsed (hours).

The estimated length of the eroded soil was found by taking the difference between the dry mass before erosion ($M_{0,Dry}$) and the dry mass after erosion ($M_{f,Dry}$) and calculating the percentage of the soil specimen that had been eroded. The percentage change was used to find the erosion rate:

$$l = H_0 \times Pecent\ of\ soil\ eroded \tag{4.2}$$

where $H_0$ is the initial height of the soil specimen (inches). The result was then converted into millimeters.

The results from the erosion tests are summarized in Appendix B. Figures 4.4 to 4.6 present the measured erosion-rate-versus-unconfined compressive strength curves for three different ranges of bed shear stress values, and Figures 4.7 to 4.9 present the results for the same tests, but with the measured erosion rate versus water content. Each data point is the result of one soil erosion test conducted under one flow condition in the hydraulic channel.

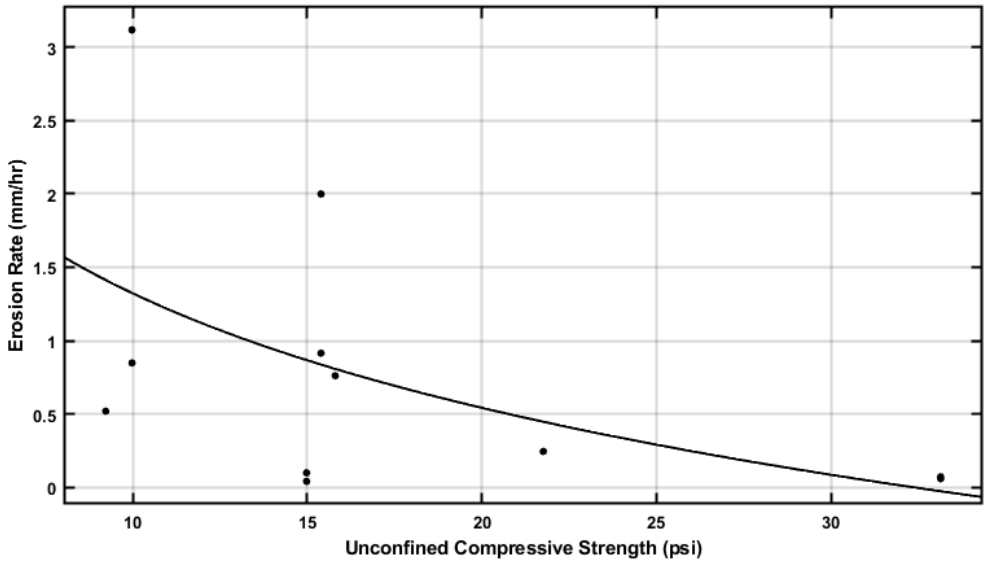


**Figure 4.4** Erosion rate vs unconfined compressive strength for $\boldsymbol{\tau_b}$ < 16 N/m$^2$

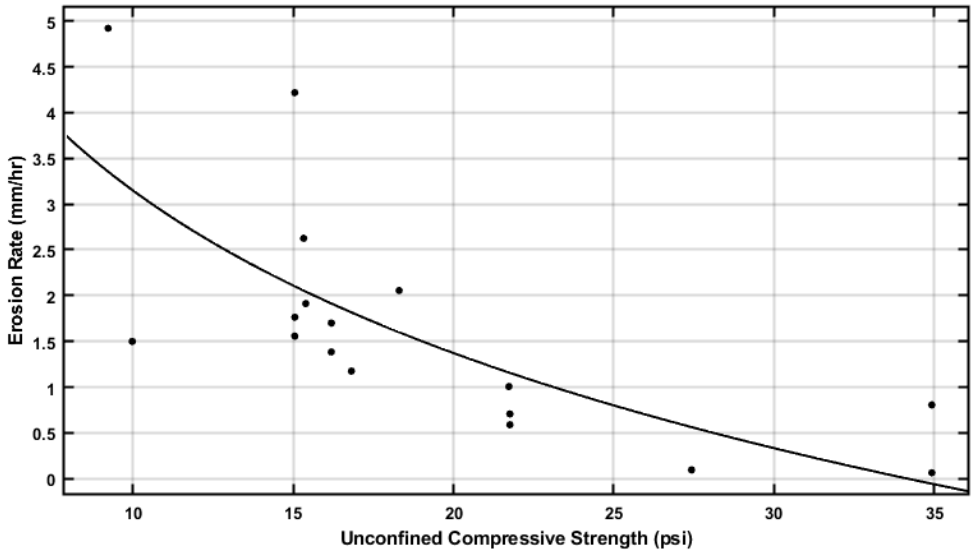


**Figure 4.5** Erosion rate vs unconfined compressive strength for $16 < \tau_b < 19.5$ N/m$^2$

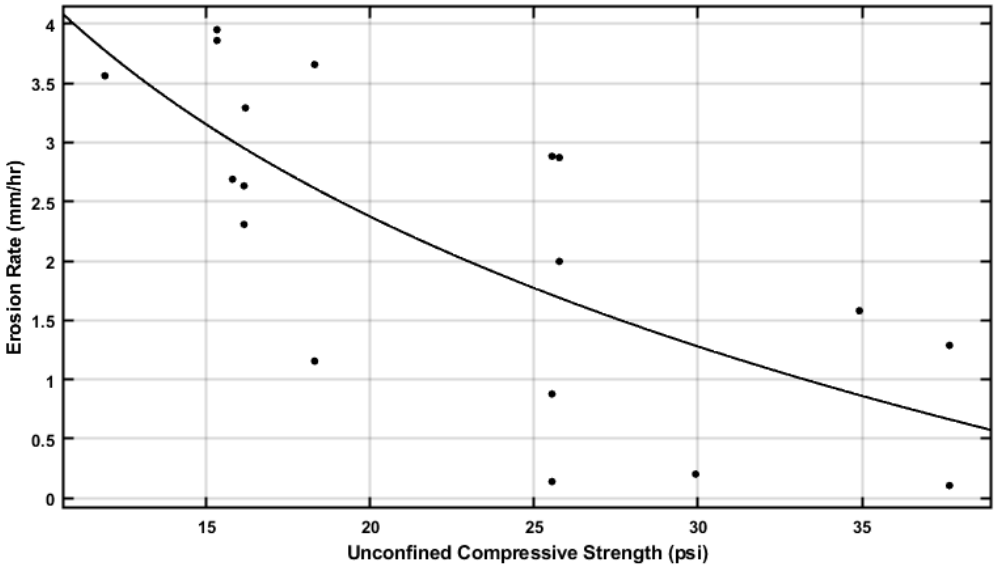


**Figure 4.6** Erosion rate vs unconfined compressive strength for $\boldsymbol{\tau_b} > 19.5$ N/m$^2$

The results were separated into three bed shear stress ranges. The lowest bed shear stress range, $\tau_b < 16$ N/m$^2$, produced results with the weakest correlation due to the critical shear stress of some of the soil specimens being greater than the applied bed shear stress resulting in little or no soil erosion.

The results were more consistent for the bed shear stress greater than 19.5 N/m$^2$. This is the range in which the soil specimens consistently had a critical shear stress that was much less than the applied bed shear stress. The soil specimens that were tested with a bed shear stress between 16 and 19.5 N/m$^2$ show a similar trendline and slope to the data with a bed shear stress greater than 19.5 N/m$^2$.

Soil samples with similar unconfined compressive strength values were found to sometimes produce a wide range of erosion rates. This could be due to the variations in surface roughness and erosion pattern as these were the two parameters that could not be controlled during the tests. This is especially true when the bed shear stress is greater than 19.5 N/m$^2$ (See Figure 4.6). These soil samples had estimated bed shear stress results that were as high as 24 N/m$^2$. The wide range of bed shear stress values could also produce large variations in the average erosion rates.

The strongest correlation between measured soil erosion rate and unconfined compressive strength was found in the bed shear stress range greater than 19.5 N/m$^2$, with $R^2 = 0.527$ and RMSE = 0.9265, producing a relationship of:

$$\dot{z} = -2.7 \ln(Q_u) + 10.5$$

Similarly good correlation was also found in the bed shear stress range between 16 and 19.5 N/m$^2$, with $R^2 = 0.5207$ and RMSE = 0.9273, producing a relationship of:

$$\dot{z} = -2.56 \ln(Q_u) + 9.05$$

The weakest correlation, with $R^2 = 0.2594$ and RMSE = 0.8774, was found when the bed shear stress was less than 16 N/m$^2$, and the relationship is given by:

$$\dot{z} = -1.125 \ln(Q_u) + 3.9$$

The unconfined compressive strength was changed during the preparation of each sample by varying the moisture content of the soil. The results for the erosion-rate-versus-water-content for three different ranges of bed shear stress measurements are presented as follows:

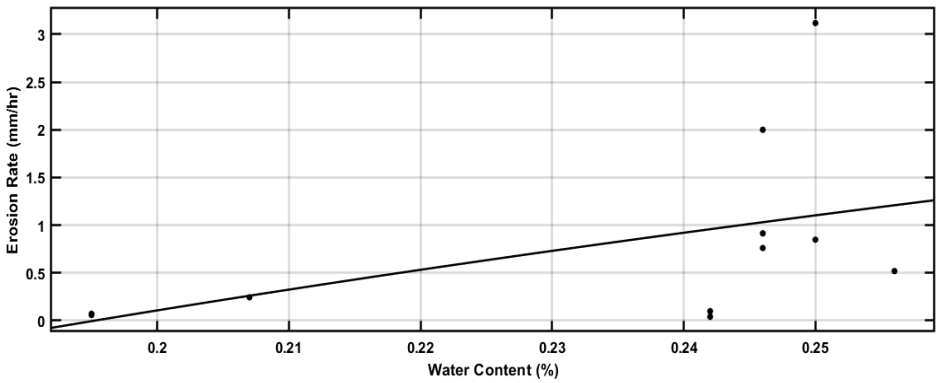


**Figure 4.7** Erosion Rate vs. water content for $\boldsymbol{\tau_b}$ < 16 N/m$^2$

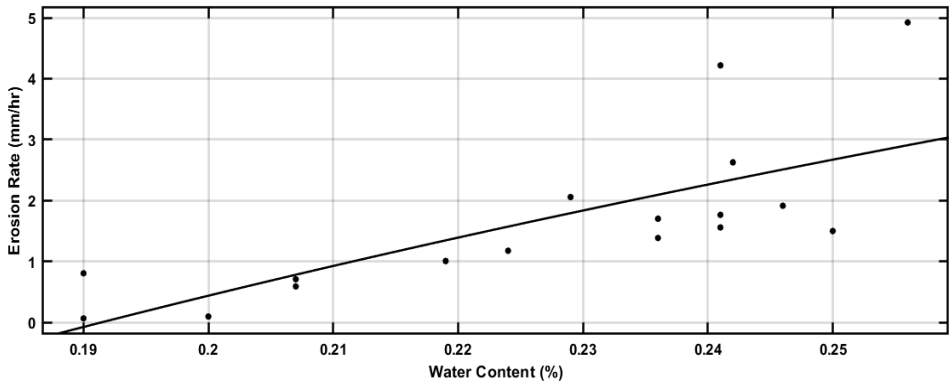


**Figure 4.8** Erosion rate vs. water content for $16 < \boldsymbol{\tau_b} < 19.5$ N/m$^2$

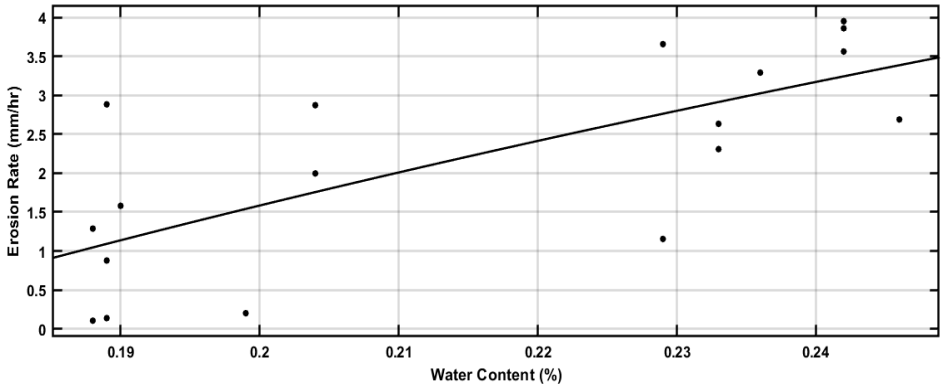


**Figure 4.9** Erosion rate vs. water content for $\boldsymbol{\tau_b} > 19.5$ N/m$^2$

The erosion-rate-versus-water-content results produced similar trend in the correlations as the erosion-rate-versus-unconfined-compressive-strength results as shown in the following:

The strongest correlation between measured bed shear stress and water content was found in the bed shear stress range greater than 19.5 N/m$^2$, with an $R^2 = 0.5263$ and RMSE = 0.9272, producing a relationship of:

$$\dot{z} = 8.7 \ln(w) + 15.6$$

The bed shear stress between 16 and 19.5 N/m$^2$ also resulted in good correlation, with $R^2 = 0.542$ and RMSE = 0.907, producing a relationship of:

$$\dot{z} = 10 \ln(w) + 16.54$$

The weakest correlation, with an $R^2 = 0.23$ and RMSE = 0.895, were the results from the bed shear stress less than 16 N/m$^2$, which had a relationship of:

$$\dot{z} = 4.46 \ln(w) + 7.3$$

These results suggest the soil erosion rate may be related to either the unconfined compressive strength or water content. This is not surprising since other soil parameters were held approximately fixed.

The applied bed shear stress was also related to the measured erosion rate for different ranges of unconfined compressive strength.

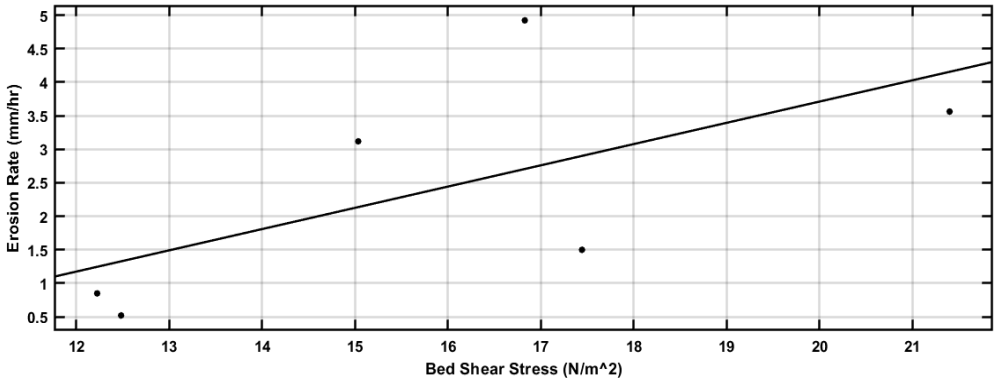


**Figure 4.10** Erosion rate vs. bed shear stress for $Q_u$ < 12 psi

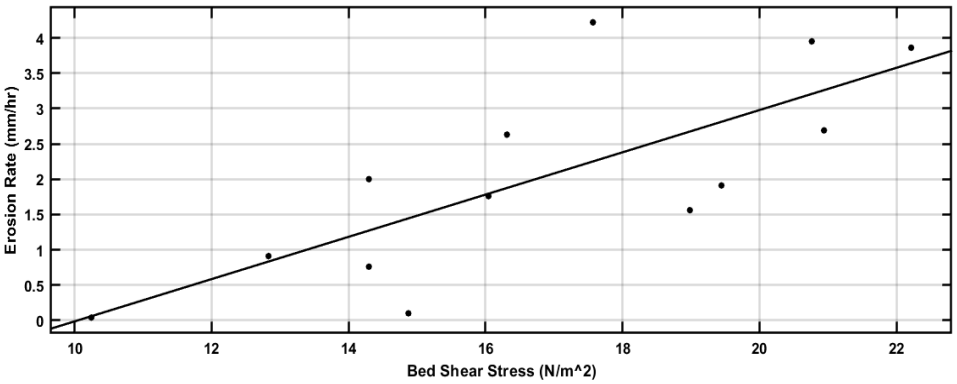


**Figure 4.11** Erosion rate vs. bed shear stress for 12 psi < $\boldsymbol{Q_u}$ < 16 psi

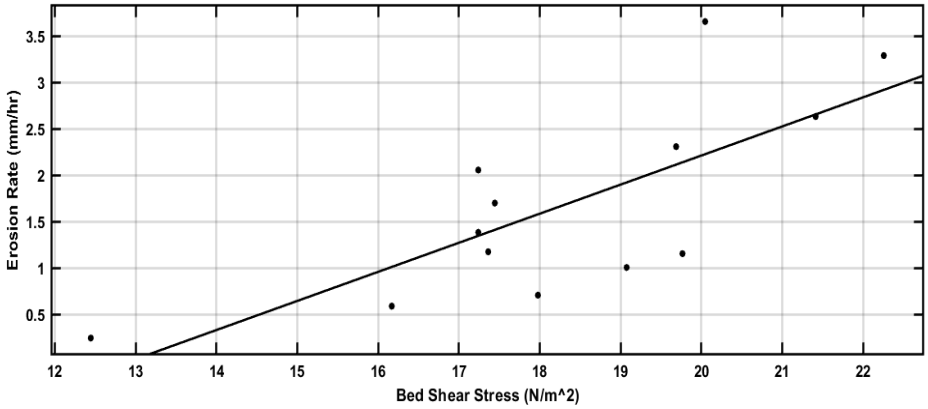


**Figure 4.12** Erosion rate vs. bed shear stress for 16 psi < $\boldsymbol{Q_u}$ < 22 psi

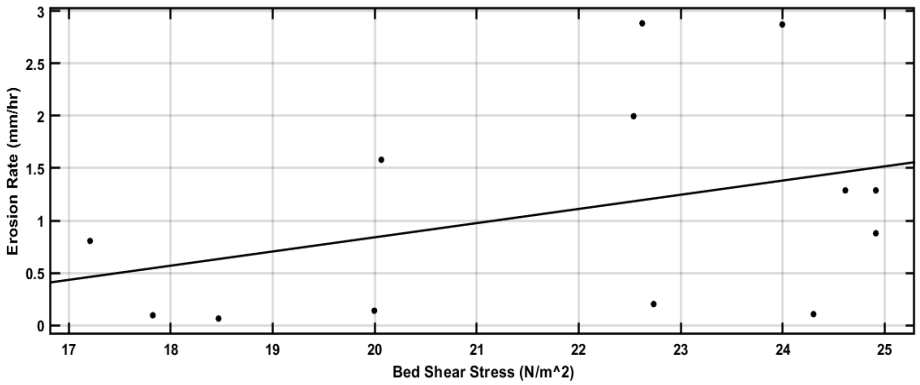


**Figure 4.13** Erosion rate vs. bed shear stress for $\boldsymbol{Q_u}$> 22 psi

The results are separated into four different unconfined compressive strength ranges. The strongest correlations were found for soil samples with an unconfined compressive strength between 12 and 16 psi and between 16 and 22 psi. Soil specimens that had an unconfined compressive strength less than 12 psi and greater than 22 psi had the least consistent results. As discussed, this could be due to the critical shear stress being greater than the shear stress exerted by the flow or variations in unconfined compressive strength and configuration of the eroding surface. Different forms of equations were fitted to each dataset. A straight-line fit was found to produce the most consistent results for the critical shear stress.

The soil specimens with an unconfined compressive strength less than 12 psi had an estimated critical shear stress of 8.3 N/m$^2$, and a best straight-line-fit with $R^2$ = 0.3989 and RMSE = 1.5.

$$\dot{z} = 0.317\tau_b - 2.632$$

The soil specimens with an unconfined compressive strength between 12 and 16 psi had an estimated critical shear stress of 10.05 N/m$^2$, and a best straight-line-fit with $R^2$ value 0.5727 and RMSE = 0.9552.

$$\dot{z} = 0.3\tau_b - 3.01$$

The soil specimens with an unconfined compressive strength between 16 and 22 psi had an estimated critical shear stress equal to 12.95 N/m$^2$, and a best straight-line fit with $R^2$ = 0.5643 and RMSE = 0.7234.

$$\dot{z} = 0.3134\tau_b - 4.06$$

The soil specimens with an unconfined compressive strength greater than 22 psi had an estimated critical shear stress equal to 13.8 N/m$^2$, and a best straight-line fit with $R^2$ = 0.1406 and RMSE = 0.9827.

$$\dot{z} = 0.1355\tau_b - 1.87$$

The critical shear stress was found by extrapolating the best-fit line to where ż was equal to zero. As seen, the estimated critical shear stress increases as the unconfined compressive strength of the soil increases.

The erosion of the clay sample was not smooth or uniform. The specimens eroded in chunks and irregular patterns. Below are a few examples of how the soil samples had eroded. Some of the clay specimens eroded in blocks or chunks creating a deep hole in the soil surface. The holes then created a change in bed configuration, which would produce non-uniform bed shear stresses. The average shear stress on the soil surface was investigated using particle image velocimetry in the next section.

Figures 4.14 to 4.19 show an erosion pattern developing from downstream to upstream in one test. The soil sample had an unconfined compressive strength of 10 psi, and the estimated bed shear stress was 12.23 $N/m^2$.

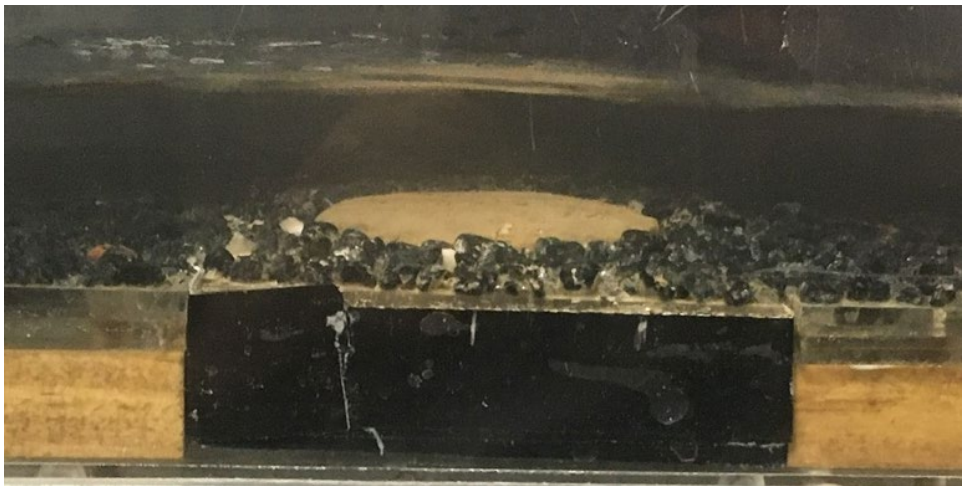

**Figure 4.14** Beginning of soil erosion test

**Figure 4.15** About 1 hour after start of erosion test

**Figure 4.16** About 2 hours after start of erosion test

**Figure 4.17** About 3 hours after start of erosion test

**Figure 4.18** About 4 hours after start of erosion test

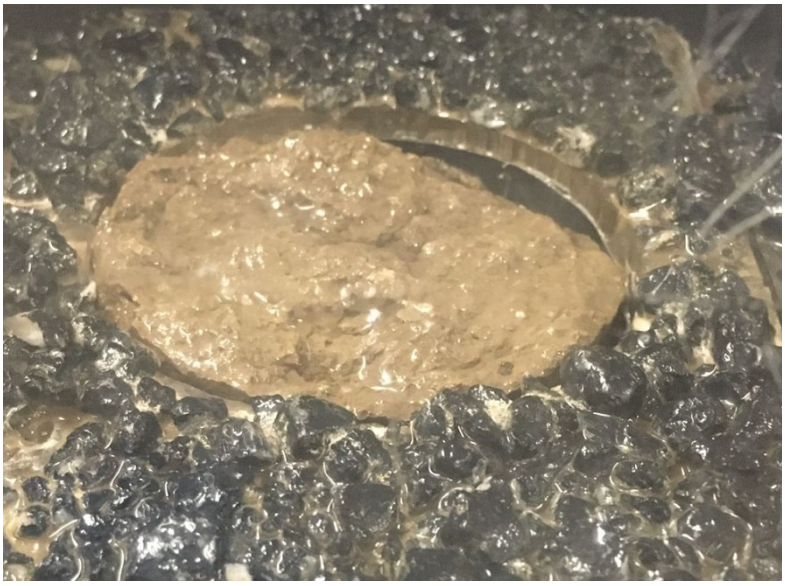

**Figure 4.19** Final erosion depth after about 5 hours

The following images show some examples of other erosion patterns observed in the erosion tests.

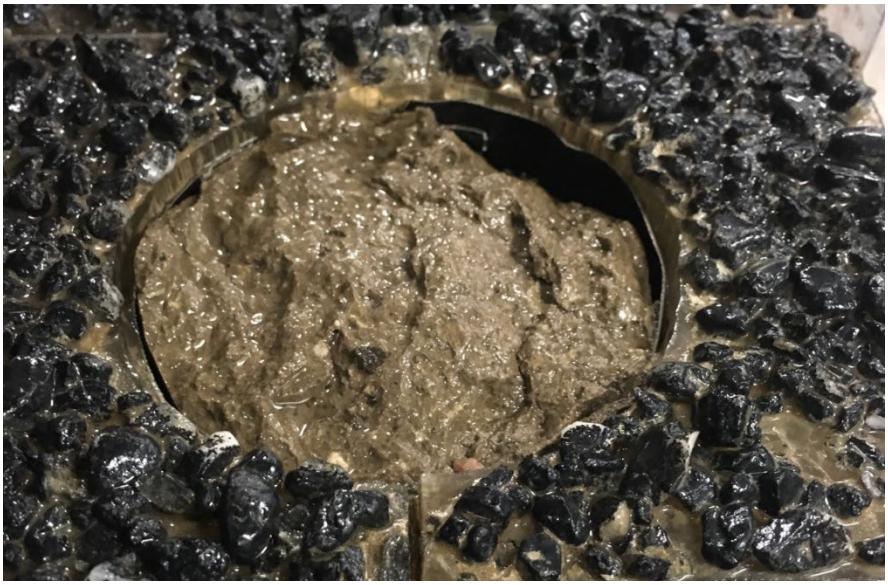

**Figure 4.20** Example of a wavy erosion pattern from front to back

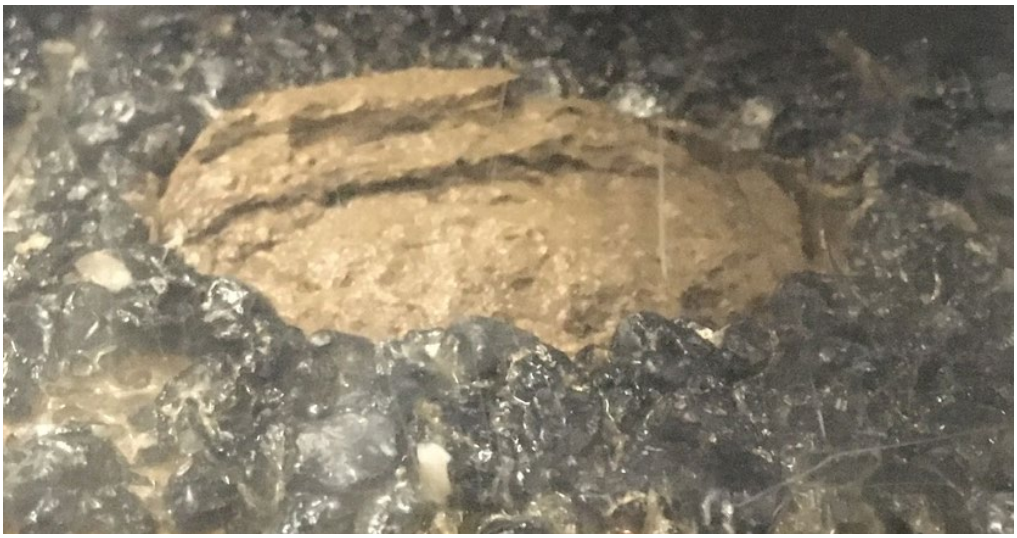

**Figure 4.21** Example of block erosion pattern from side-to-side

**Figure 4.22** Example of cone-shaped erosion pattern

**Figure 4.23** Example of non-uniform erosion pattern in the downstream portion of soil sample

**Figure 4.24** Example of little-to-no erosion

## 4.2 Particle Image Velocimetry Measurements Over Fixed Gravel Bed

Particle image velocimetry (PIV) measurements were conducted on a fixed bed composed of a single layer of gravel with a $d_{50}$ of 5.6 mm in the A-8 hydraulic channel. The objective of the PIV measurements was to measure the time-averaged velocity profile over the gravel bed and use the measured data to determine the equivalent roughness and bed shear stress using the log law. The results showed that the bed shear stress estimates are in good agreement with the values obtained from the measured flow depth and channel slope (depth-slope method) when the equivalent grain diameter is approximated by $d_{84}$ or smaller.

The procedure for operating the camera, LED illuminator, and the channel bed setup is described in Section 3.7. The plane of PIV measurements was located about 75 mm from the side wall closest to the camera. Figure 4.25 shows the experimental setup for the PIV camera and LED illuminator with the fixed gravel bed installed in the hydraulic channel.

After uniform flow was established, the flow depth was measured using a point gauge approximately 0.42 m upstream from the center of the test area. In most runs (see below), 200 straddled frames (frames A and B) were captured at a sampling rate of 7.25 Hz. Ensemble correlation processing was performed on all 200 images to obtain the mean velocity field. Spatial averaging was then conducted on the mean velocity field to obtain a time- and space-averaged velocity profile for finding the bed shear stress.

The false bottom with the gravel bed was secured to the smooth acrylic channel using metal screws and in-floor inserts. The false bottom had a height of about 1.5 inches (38.1 mm) from the top of the rock to the bottom of the wood base. The channel width was 6 inches (152.4 mm) and the average discharge rate for the water flowing over the gravel bed was 0.158 $ft^3/s$ (4.5 L/s).

PIV measurements were taken at six different slopes in 11 tests to cover a wide range of bed shear stress values. Each test contained three or four consecutive runs. The PIV measurements were typically taken with the fixed gravel bed in the lower part of the PIV camera's FOV and the free surface just above the top of the captured images. Five of the six flow conditions were repeated, as shown in Table 4.2. Two hundred velocity vector fields were captured in each run except for Test 5 where 100 images were captured.

After the PIV images were taken for each test, the data were processed using the *INSIGHT 4G*$^{TM}$ software by TSI. An ensemble correlation velocity field was created with the dimensions of the interrogation regions equal to 64 pixels × 32 pixels with a 50% overlap. The spatial resolution was approximately 0.53 mm in the streamwise direction and 0.27 mm in the vertical direction. A plot of the measured velocity field created using Tecplot is shown in Figure 4.27. The ensemble correlation velocity field has 56 vector columns but only every three columns are displayed in Figure 4.27 for clarity. The dashed line marks the very top of the gravel bed in the camera's FOV. There was flow within the gravel bed below the dashed line. Missing vectors were interpolated from the neighboring vectors. The free surface in Figure 4.27 is located above but close to $y$ = 30 mm.

The different runs in each test performed during the experiment were averaged to obtain an ensemble- and space-averaged (average) velocity profile. Typically, the runs that were averaged had good repeatability and plotted similarly to one another.

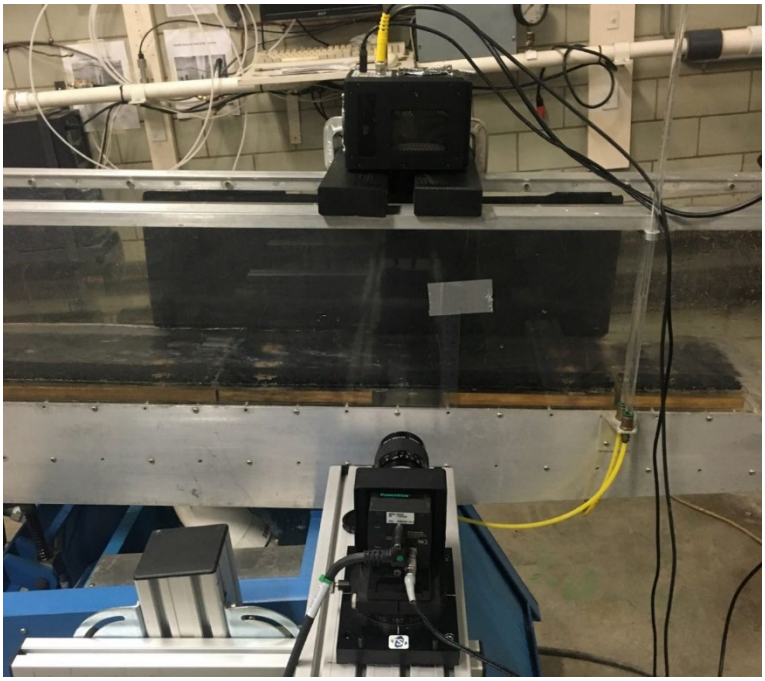

**Figure 4.25** Fixed gravel bed PIV measurement setup

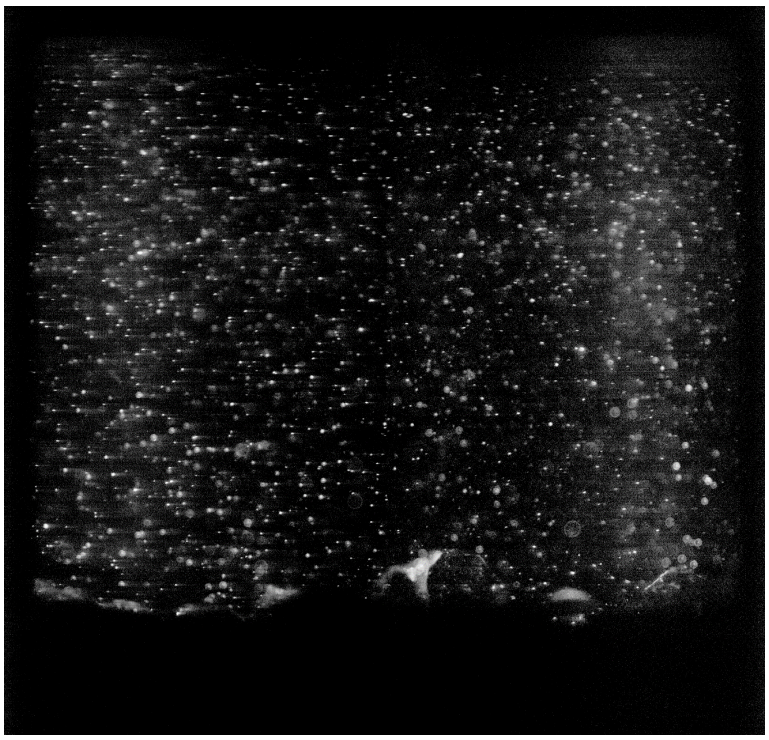

**Figure 4.26** Example PIV image from the fixed gravel bed experiment

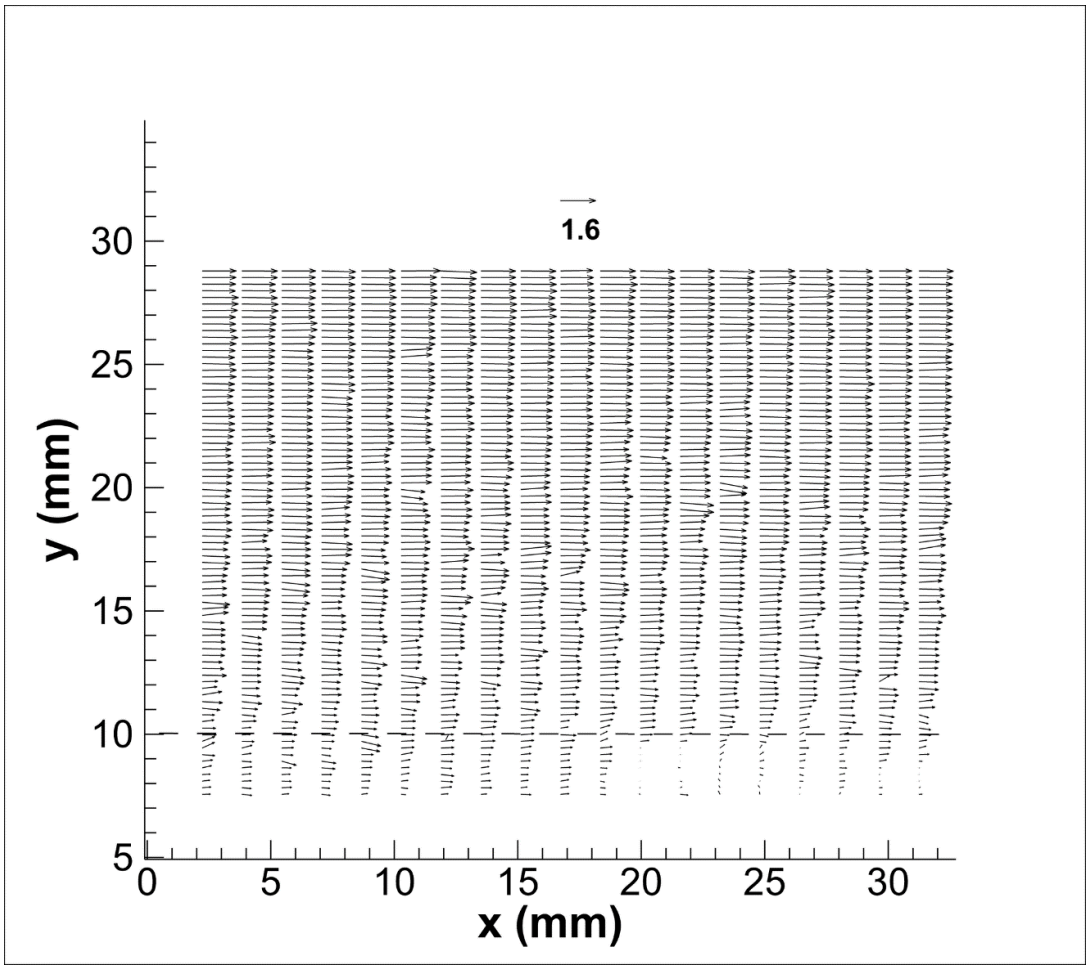


**Figure 4.27** Measured velocity profile from Test 8, Run 1

The side-wall correction method, described in Section 3.6 and the log-law method described below were employed to determine the equivalent roughness and bed shear stress in each test.

**Table 4.1** Summary of flow parameters for the fixed gravel bed experiments

| Test | $Q$ (L/s) | $S$ | $T$ (°C) | $h$ (mm) | $h_e$ (mm) | $V$ (m/s) | $V_1$ (m/s) | $f_b$ | $R_b$(mm) | $\tau_{b1}$ (N/m$^2$) |
|---|---|---|---|---|---|---|---|---|---|---|
| 1 (4) | 4.5 | 0.02 | 26 | 39.1 | 36.3 | 0.808 | 0.782 | 0.0764 | 31.8 | 6.22 |
| 2 (4) | 4.5 | 0.02 | 27 | 39.4 | 36.6 | 0.803 | 0.795 | 0.0782 | 32.1 | 6.28 |
| 3 (4) | 4.5 | 0.04 | 27 | 32.5 | 29.7 | 0.988 | 0.988 | 0.0866 | 26.9 | 10.53 |
| 4 (4) | 4.5 | 0.04 | 27 | 32.5 | 29.7 | 0.988 | 0.995 | 0.0866 | 26.9 | 10.53 |
| 5 (3) | 4.5 | 0.05 | 23.5 | 30.5 | 27.7 | 1.061 | NA | 0.0881 | 25.3 | 12.35 |
| 6 (4) | 4.5 | 0.06 | 27 | 29.6 | 26.8 | 1.096 | 1.098 | 0.0969 | 24.7 | 14.49 |
| 7 (4) | 4.5 | 0.06 | 27 | 29.6 | 26.8 | 1.096 | 1.103 | 0.0969 | 24.7 | 14.49 |
| 8 (4) | 4.5 | 0.08 | 24 | 26.8 | 24.00 | 1.223 | 1.139 | 0.0933 | 22.2 | 17.40 |
| 9 (4) | 4.5 | 0.08 | 28 | 26.9 | 24.1 | 1.22 | 1.18 | 0.0941 | 22.3 | 17.44 |
| 10 (4) | 4.5 | 0.10 | 27 | 25.4 | 22.6 | 1.299 | 1.309 | 0.0982 | 21.1 | 20.64 |
| 11 (4) | 4.5 | 0.10 | 27 | 24.4 | 22.6 | 1.299 | 1.304 | 0.0982 | 21.1 | 20.64 |

In Table 4.1, $V$ is the cross-sectional average velocity computed from the measured discharge and flow depth, and $V_1$ is the depth-averaged velocity obtained from the PIV measured velocity profile. In parentheses in the first column of Table 4.1 is the number of runs that were averaged in each test. The bed shear stress, $\tau_{b1}$, was found by:

$$\tau_{b1} = \rho g R_b S \tag{4.3}$$

where $\rho$ is the fluid density (kg/m$^3$), $g$ is the acceleration of gravity (m/s$^2$), $R_b$ is the bed-related hydraulic radius (m), and $S$ is the channel slope (m/m). Equation 4.3 was employed in steady, uniform flows. The sidewall correction method was used to estimate the bed related friction factor, $f_b$, and hydraulic radius, $R_b$, as described in Section 3.6.

The method described in Ting and Kern (2022) was used to determine the equivalent roughness $k_s$ of the gravel bed using the average velocity profile in conjunction with the bed shear stress obtained from the depth-slope method. The method assumes that the von Kármán constant is a universal constant with a value equal to 0.4. The procedure for finding $k_s$ is briefly described using Figures 4.28 through 4.30 and Tables 4.2 and 4.3. For more details about the procedure and discussion of the test results, the interested reader is referred to Ting and Kern (2022).

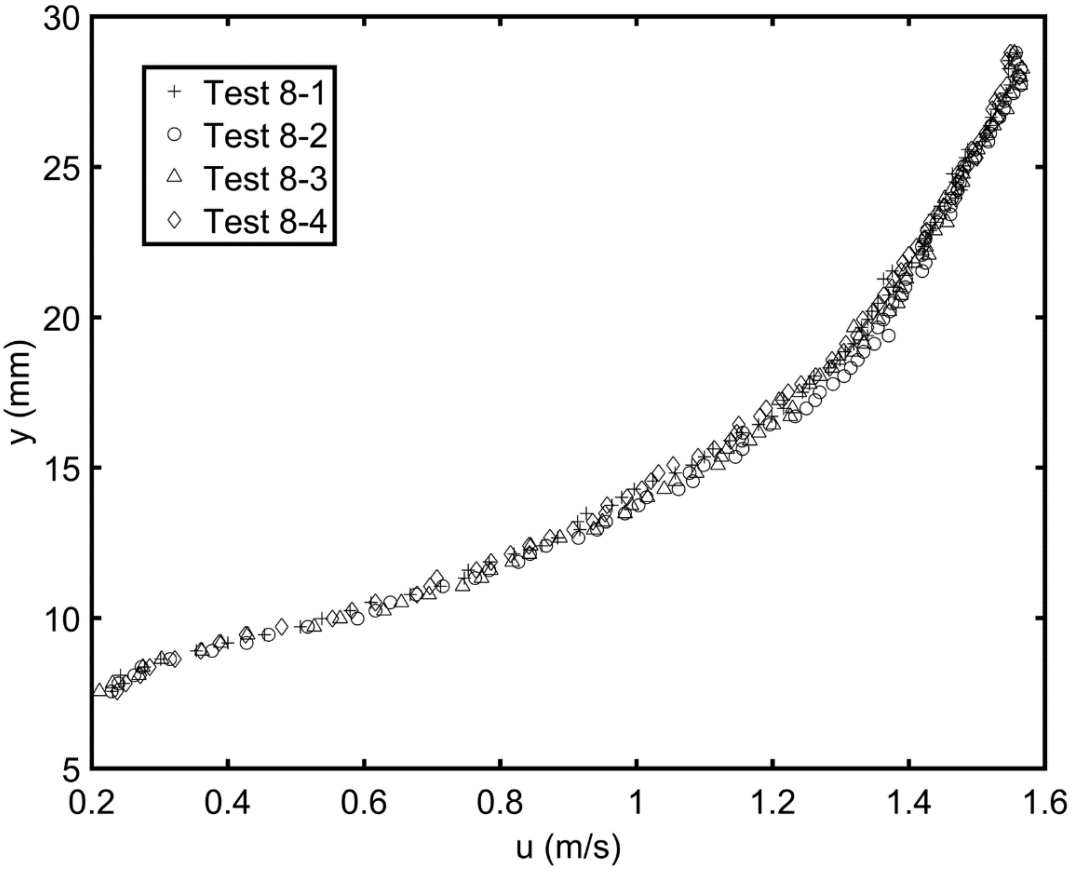


**Figure 4.28** Time- and space-averaged velocity profiles from Test 8, Runs 1 to 4

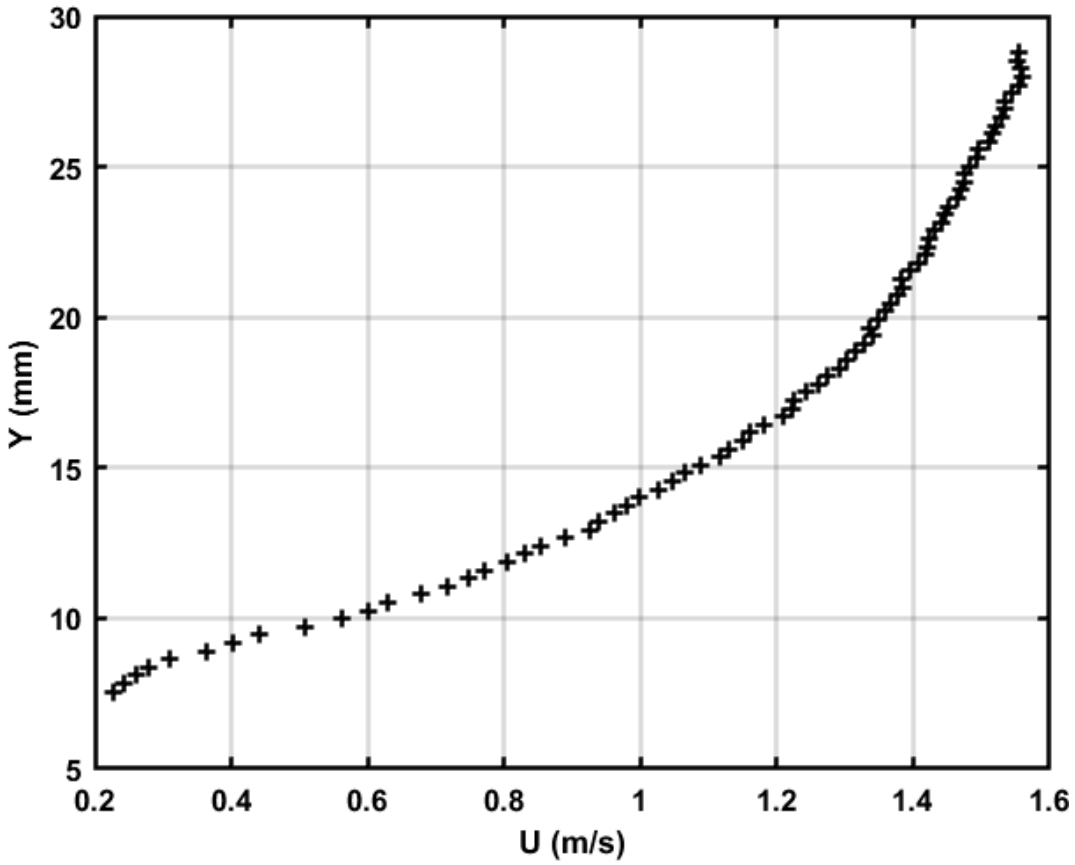


**Figure 4.29** Average profile from Runs 1 to 4 in Test 8

Figure 4.28 displays the time- and space-averaged velocity profiles from four runs conducted consecutively in Test 8. The measured velocity profiles show good repeatability and were averaged to produce a single average velocity profile, as shown in Figure 4.29.

The average velocity profile is then graphed on a $\ln(y - y_0)$ versus $u$ plot, as shown in Figure 4.30, and Eq. (4.4) is fitted to the logarithmic region:

$$\ln(y - y_0) = \frac{\kappa}{u^*}u + (\ln(k_s) - \kappa B) \tag{4.4}$$

In Eq. (4.4), $\kappa/u^*$ is the slope of the fitted straight line, $\ln(k_s) - kB$ is the $y$-intercept, and $B$ has a value of 8.5 for fully developed turbulent flow over a rough bed (e.g., Middleton and Southard, 1984).

Table 4.2 shows how the location of the virtual bottom is varied to find the correct bed shear stress using the average velocity profile shown in Figure 4.29. This test had a measured water temperature of 24°C and an average water depth of 1.055 inches (26.8 mm). Typically, the points used for the log-law curve fitting method are taken to be no higher than 20% to 30% of the flow depth above the rough bed. The lower bound is set away from any direct influence of the roughness of the bed. In Test 8, point number 30 was used as the conservative upper bound of the lower 30% of the log-law curve fitting. Test 8 also has part of its velocity profile plotted below the top of the gravel indicated by the dashed line at $y$ =10 mm in Figure 4.27. This eliminates the

lower 10 data points for use in curve fitting. Therefore, the log-law region was assumed to lie somewhere between points 10 and 30.

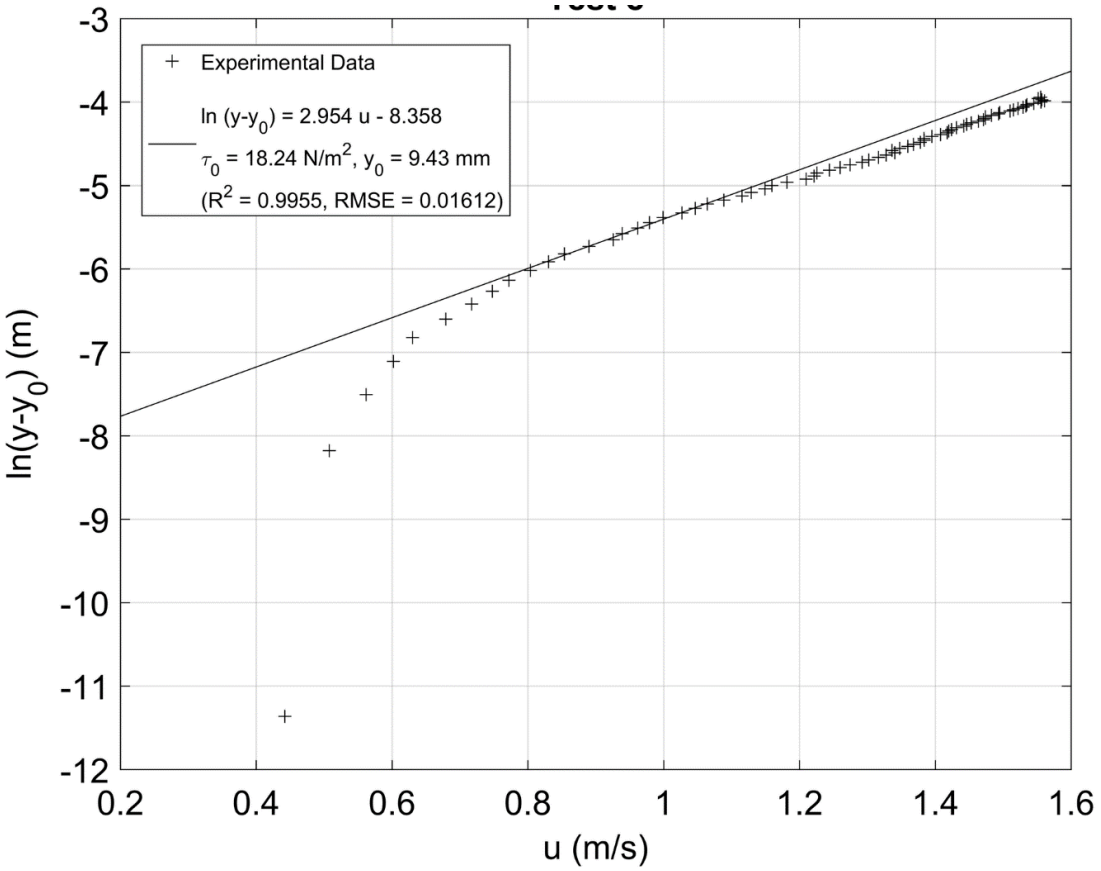


**Figure 4.30** Semi-log plot for Test 8

**Table 4.2** Test 8 log-law iteration results

| (1) $y_0$ (mm) | (2) $a = \kappa/u^*$ | (3) $b = ln(k_s) - 8.5k$ | (4) $u^* = \kappa/a$ (m/s) | (5) $k_s = e^{(8.5\kappa+b)}$ (mm) | **(6)** $\tau_{b2} = \rho u^{*2}$ (N/m$^2$) | (7) $R^2$ | (8) RMSE | (9) $k_s$ (mm) | (10) $\kappa = \frac{ln(k_s) - b}{8.5}$ | (11) $u^* = \kappa/a$ (m/s) | **(12)** $\tau_{b2} = \rho u^{*2}$ (N/m$^2$) |
|---|---|---|---|---|---|---|---|---|---|---|---|
| 9.1 | 2.718 | -8.051 | 0.1472 | 9.55 | **21.60** | 0.9957 | 0.01453 | 7 | 0.36 | 0.1337 | **17.83** |
| 9.2 | 2.786 | -8.139 | 0.1436 | 8.75 | **20.56** | 0.9956 | 0.01496 | 7 | 0.37 | 0.1342 | **17.95** |
| 9.3 | 2.856 | -8.232 | 0.1401 | 7.97 | **19.56** | 0.9956 | 0.01543 | 7 | 0.38 | 0.1347 | **18.10** |
| 9.4 | 2.931 | -8.328 | 0.1365 | 7.24 | **18.57** | 0.9955 | 0.01595 | 7 | 0.40 | 0.1351 | **18.21** |
| **9.43** | **2.954** | **-8.358** | **0.1354** | **7.03** | **18.29** | **0.9955** | **0.01612** | **7** | **0.40** | **0.1353** | **18.24** |
| 9.5 | 3.01 | -8.43 | 0.1329 | 6.54 | **17.61** | 0.9954 | 0.01652 | 7 | 0.41 | 0.1356 | **18.33** |
| 9.6 | 3.093 | -8.536 | 0.1293 | 5.88 | **16.68** | 0.9953 | 0.01717 | 7 | 0.42 | 0.1359 | **18.43** |
| 9.65 | 3.136 | -8.591 | 0.1276 | 5.57 | **16.23** | 0.9953 | 0.01752 | 7 | 0.43 | 0.1361 | **18.49** |
| 9.7 | 3.181 | -8.648 | 0.1257 | 5.26 | **15.77** | 0.9952 | 0.01788 | 7 | 0.43 | 0.1363 | **18.54** |
| 9.8 | 3.275 | -8.766 | 0.1221 | 4.67 | **14.88** | 0.9951 | 0.01869 | 7 | 0.45 | 0.1367 | **18.62** |
| 9.9 | 3.374 | -8.89 | 0.1186 | 4.13 | **14.02** | 0.9949 | 0.0196 | 7 | 0.46 | 0.1370 | **18.71** |

Table 4.2 summarizes the results of the iterative process for finding the bed shear stress using the traditional method and an alternative method adopted in this study. The value of $y_0$ is given in Column (1). For each $y_0$ value, a plot of $\ln(y - y_0)$ versus $u$ was constructed and a straight line was fitted to the velocity data. The slope, $a$, and $y$-intercept, $b$, of the best-fit line are shown in Column (2) and Column (3), respectively. Using Eq. (4.4), the friction velocity $u^*$ in Column (4) is obtained from the slope of the best-fit line assuming a value of 0.4 for $k$, and the equivalent roughness, $k_s$, in Column (5) is obtained from the $y$-intercept of the best-fit line. The $R^2$ value of the best-fit line is given in Column (7) and the RMSE in Column (8).

Figure 4.30 presents the semi-log plot of $\ln(y\text{-}y_0)$ versus $u$ with the best-fit lines drawn to points 18 to 28 with $y_0$ = 9.43. Columns (5) and (6) in Table 4.2 show how the traditional method of varying $y_0$ to find the best-fit line would produce a wide range of possible values for $\tau_b$ and $k_s$ that are difficult to assess. Table 4.2 shows that $\tau_b$ decreases from 21.6 to 14.02 N/m$^2$ and $k_s$ from 9.55 to 4.13 mm, when $y_0$ is increased from 9.1 to 9.9 mm. The correct value of $\tau_b$ and $k_s$ cannot be determined based on the $R^2$ and RMSE values because they are all very close.

A different method is used in this study to determine the value of $y_0$. The procedure is illustrated in columns 9 through 12 in Table 4.3. The method assumes a value of $k_s$ ($\mathbf{d}_{84}$ = 7 mm in this example) and varies $y_0$ systematically until the value of $\kappa$ found from the $y$-intercept of the best-fit line is equal to 0.4. The friction velocity $u^*$ is then found from the slope of the best-fit line. For $y_0$ = 9.43 mm, we have:

$$\kappa = \frac{\ln\left(\frac{k_s}{1000}\right) - b}{8.5} \tag{4.5}$$

$$\Rightarrow \frac{\ln\left(\frac{7}{1000}\right) - (-8.358)}{8.5} = 0.4$$

$$u^* = \frac{\kappa}{a} \tag{4.6}$$

$$\Rightarrow \frac{0.4}{2.954} = 0.1353$$

$$\tau_b = \rho(u^*)^2 \tag{4.7}$$

$$\Rightarrow 996.2 \times (0.1353)^2 = \mathbf{18.24\ N/m^2}$$

This method produces a narrow range of $\tau_b$ values as $y_0$ is varied, as seen in Column (12) in Table 4. The value of $\tau_b$ increases from 17.69 to 18.78 N/m$^2$ when $y_0$ is increased from 9.1 to 9.9 mm.

The method described above assumed that the value of the equivalent roughness was known. Table 4.3 shows the results of a sensitivity analysis where the value of $k_s$ was set equal to the $d_{50}$, $d_{65}$, and $d_{84}$ of the gravel bed. In Table 4.3, $y_0$ is the location of the virtual bottom, $y_1$ is the top of the gravel bed, and $y_2$ is the approximate location of the free surface. The sensitivity analysis was conducted for six different channel slopes. The table shows that the bed shear stress calculated using the $d_{84}$ value matches the value obtained from the measured flow depth and

channel slope given by $\tau_{b1}$well up to a channel slope of about 8%. The bed shear stress values obtained using the log law with $k_s$ equal to $d_{84}$ ($\tau_{b2}$) are within 10% of $\tau_{b1}$. The results obtained using $d_{65}$ also show good agreement when the slope of the channel is steeper, which results in a smaller flow-depth-to-grain-diameter ratio. The bed shear stress values obtained using the two different methods are plotted in Figure 4.31 with a line of perfect fit corresponding to $\tau_{b1} = \tau_{b2}$. This figure shows that there is a gradual shift to the smaller values of $k_s$ as $\tau_b$ increases and the $h/d_{90}$ ratio decreases. In Tests 1 to 7, the best agreement between the bed shear stress estimates obtained using the depth-slope method ($\tau_{b1}$) and the log law ($\tau_{b2}$) is found when $d_{84}$ is chosen as the equivalent roughness height. In Test 8, $d_{65}$ provides a better choice for $k_s$. In Tests 10 and 11 ($h/d_{90} = 3.4$), the desired value of $k_s$ is close to the $d_{50}$ (= 5.6 mm), which yields $k_s/d_{90} = 0.76$. The latter is close to the value of 0.78 obtained at $h/d_{90} = 3.0$ by Kamphuis (1974). The value of $k_s$ found for $h/d_{90} < 10$ is significantly smaller than the value of $2.5d_{90}$ found for the large $h/d_{90}$ ratios in his paper. Therefore, our results are consistent with the findings in previous studies (e.g., Kamphuis, 1974; Camenen et al., 2006).

To determine the bed shear stress on the soil surface, the equivalent roughness of the gravel bed was determined under a steady flow condition by matching the bed shear stress values obtained using the depth-slope method and the log law, as shown in Table 4.3. The same value of $k_s$ was then used with the measured velocity profile over the sediment recess to estimate the bed shear stress on the eroding soil. Note that although $\tau_{b2}$ varies with the value of $k_s$ chosen, the results are less sensitive (see Table 4.3) compared with when $k_s$ is determined together with $u^*$ in the traditional method (see Table 4.2).

**Table 4.3** Summary table for each slope comparing two methods to calculate bed shear stress

| Test | Slope | $y_0, y_1, y_2$ | $\tau_{b1} = \rho g R_b S$ | $\tau_{b2}$, log law (N/m$^2$) | | | | Percent difference | | |
|---|---|---|---|---|---|---|---|---|---|---|
| | $S$ | (mm) | (N/m$^2$) | $d_{50}$ | $d_{65}$ | $d_{84}$ | 95% CI | $d_{50}$ | $d_{65}$ | $d_{84}$ |
| 1 | 0.02 | 1.1, 4, 36.1 | 6.22 | 5.24 | 5.39 | 5.77 | ± 0.1 | 15.8% | 13.3% | **7.2%** |
| 2 | 0.02 | 1.7, 4, 36.4 | 6.28 | 5.62 | 5.82 | 6.2 | ± 0.4 | 10.5% | 7.3% | **1.3%** |
| 3 | 0.04 | 4.6, 7, 32.5 | 10.53 | 9.36 | 9.76 | 10.34 | ± 0.7 | 11.1% | 7.3% | **1.8%** |
| 4 | 0.04 | 4.8, 7, 32.5 | 10.53 | 6.59 | 10.02 | 10.63 | ± 1.0 | 37.4% | 4.8% | **-0.9%** |
| 5 | 0.05 | 12.3, 13.4, 36.5 | 12.35 | 11.38 | 11.87 | 12.79 | ± 1.0 | 7.9% | 3.9% | **-3.6%** |
| 6 | 0.06 | 4.3, 7, 29.6 | 14.49 | 12.45 | 12.98 | 13.72 | ± 0.6 | 14.1% | 10.4% | **5.3%** |
| 7 | 0.06 | 4.2, 7, 29.6 | 14.49 | 12.42 | 12.94 | 13.91 | ± 0.7 | 14.3% | 10.7% | **4.0%** |
| 8 | 0.08 | 9.4, 10, 29.8 | 17.4 | 16.26 | 16.98 | 18.27 | ± 1.9 | 6.6% | **2.4%** | -5.0% |
| 9 | 0.08 | 5.3, 6, 25.9 | 17.44 | 15.2 | 15.99 | 17.1 | ± 4.4 | 12.8% | 8.3% | **1.9%** |
| 10 | 0.10 | 10.6, 13.6, 31.9 | 20.64 | 21.19 | 22.1 | 23.67 | ± 1.8 | **-2.7%** | -7.1% | -14.7% |
| 11 | 0.10 | 10.6, 13.6, 31.9 | 20.64 | 21.87 | 21.75 | 23.29 | ± 1.7 | -6.0% | **-5.4%** | -12.8% |

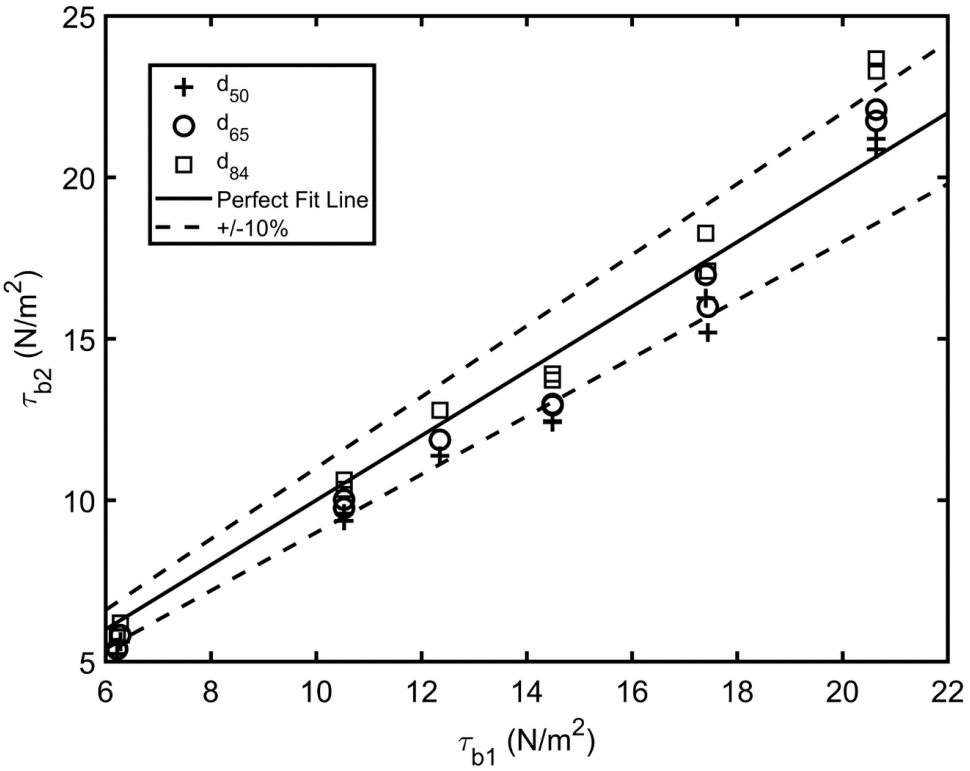


**Figure 4.31** Bed shear stress results plotted with a line of perfect agreement

## 4.3 Particle Image Velocimetry Measurements Over Cohesive Soil Sample

Using a similar procedure, particle image velocimetry (PIV) measurements were taken with a clay sample placed in the sediment recess in the fixed gravel bed. The measured data were used to estimate the average bed shear stress acting on the surface of the clay sample at different soil erosion depths.

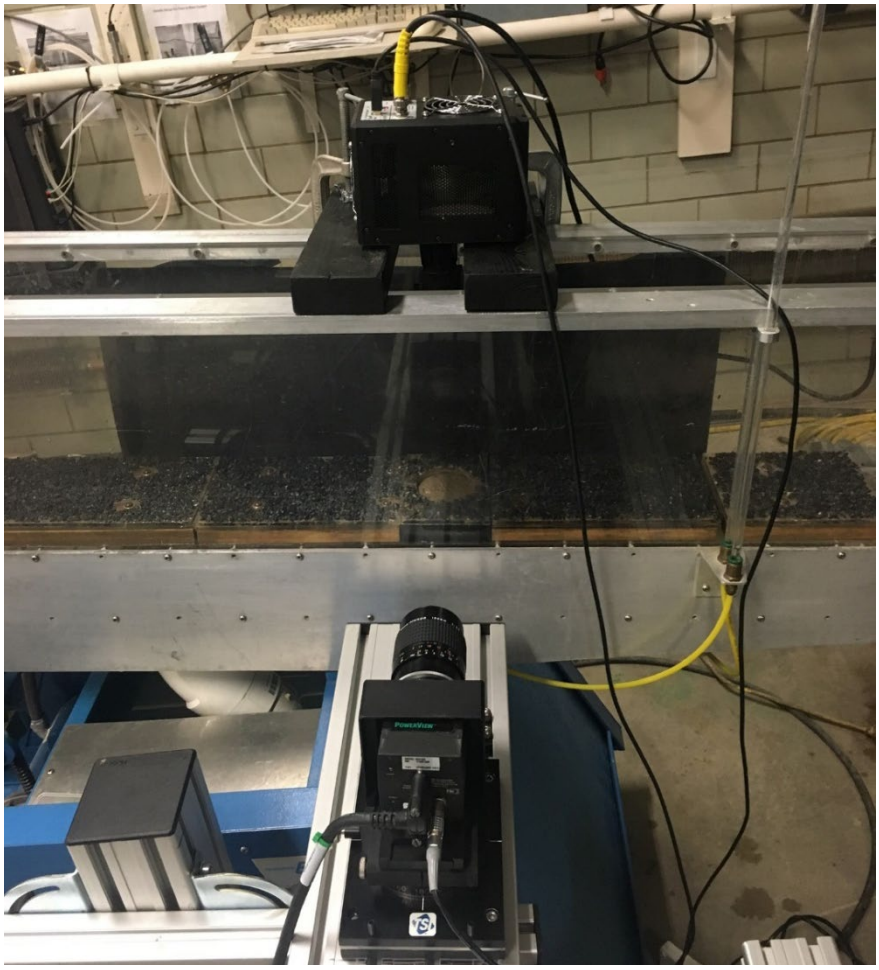

**Figure 4.32** Typical setup for PIV experiments with a clay sample

### 4.3.1 No Erosion

The objective of these tests was to measure the bed shear stress on a cohesive soil sample that was surrounded by a gravel bed. The top surface of the clay sample was smooth and at about the same elevation as the top of the surrounding gravel at the start of the test. Three tests were conducted for a constant discharge of 0.158 $ft^3$/sec (4.5 L/s) at a channel slope of 8% for comparison with the measurements obtained on the fixed gravel bed in the previous section.

The procedure for operating the camera, LED illuminator, and channel bed setup can be found in Section 3.7. The measurement plane was set at 75 mm from the side wall closest to the camera, along the center line of the channel. The water depth was measured at approximately 0.42 m

upstream from the soil sample. This water depth was used to calculate the bed shear stress ($\tau_{b1}$) using the depth-slope method. PIV measurements were taken after steady flow was established.

Figure 4.33 shows an example of the PIV image over the clay bed from Test 1 (see Table 4.4). The ensemble correlation velocity field is shown in Figure 4.34, and the ensemble- and space-averaged velocity profile is shown in Figure 4.35.

The average velocity profile was then graphed on a $\ln(y - y_0)$ versus $u$ plot. The displacement height, $y_0$, was found using the procedure described in Section 4.2. Figures 4.36, 4.37, and 4.38 show the semi-log plots for Tests 1, 2, and 3, respectively. These tests were conducted under the same flow conditions, and four runs were completed in each test to compute the average velocity profile. The test results are summarized in Table 4.4.

All the PIV erosion experiments were performed at an 8% slope. Bed shear stress over the clay sample was determined from the measured average velocity profile using the log law assuming an equivalent bed roughness $k_s$ of 6.1 mm. As discussed in Section 4.2, when the slope of the hydraulic channel is above 8%, the equivalent roughness of the gravel bed may be taken as the $d_{65}$ of the gravels. It is assumed that the same $k_s$ value may be applied to the clay bed. Because the time it took for the flowing water to pass over sediment recess was very brief (< 0.1 second), the structure of turbulence over the soil sample was dominated by the advection of boundary-layer turbulence generated on the gravel bed upstream, instead of locally generated turbulence on the clay bed. More discussion on flow over the soil sample and transition in bed roughness is given in Chapter 5.

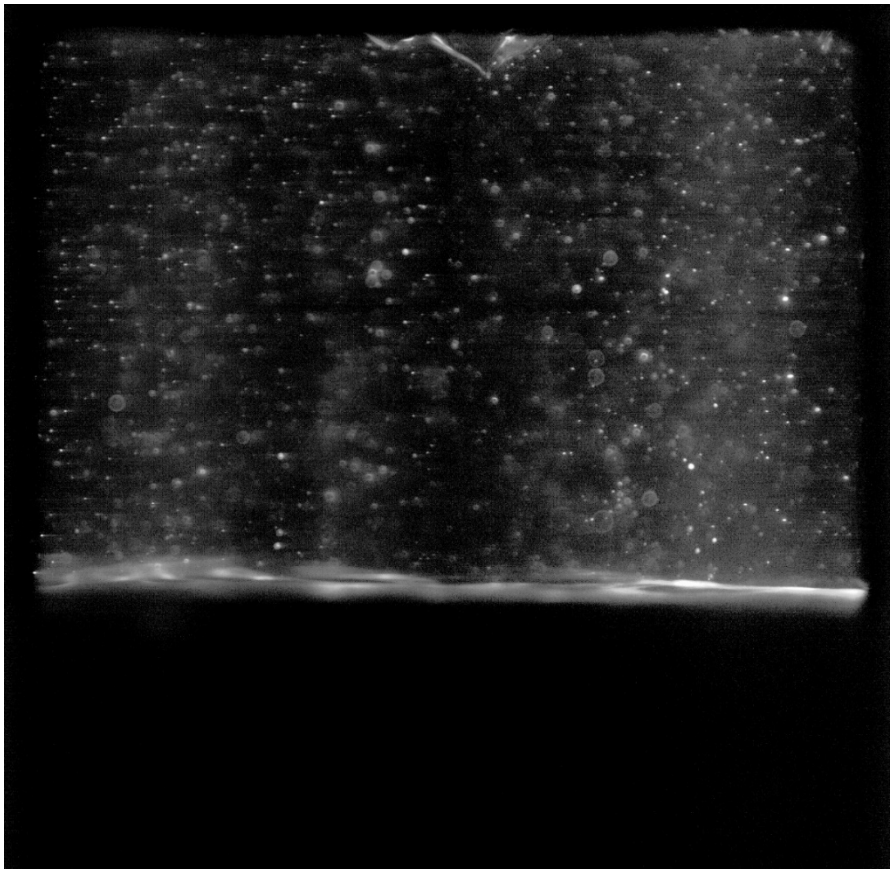

**Figure 4.33** An example of the PIV image from Test 1, Run 1

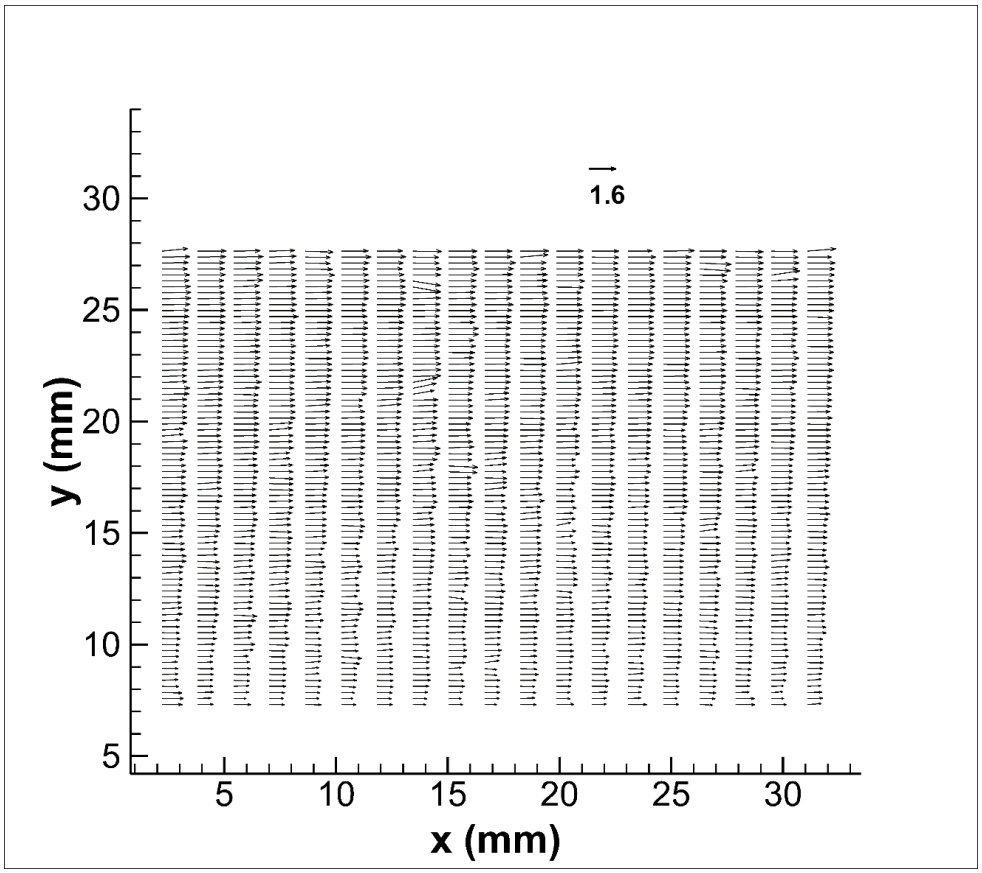


**Figure 4.34** Velocity profiles of the processed data from Test 1, Run 1

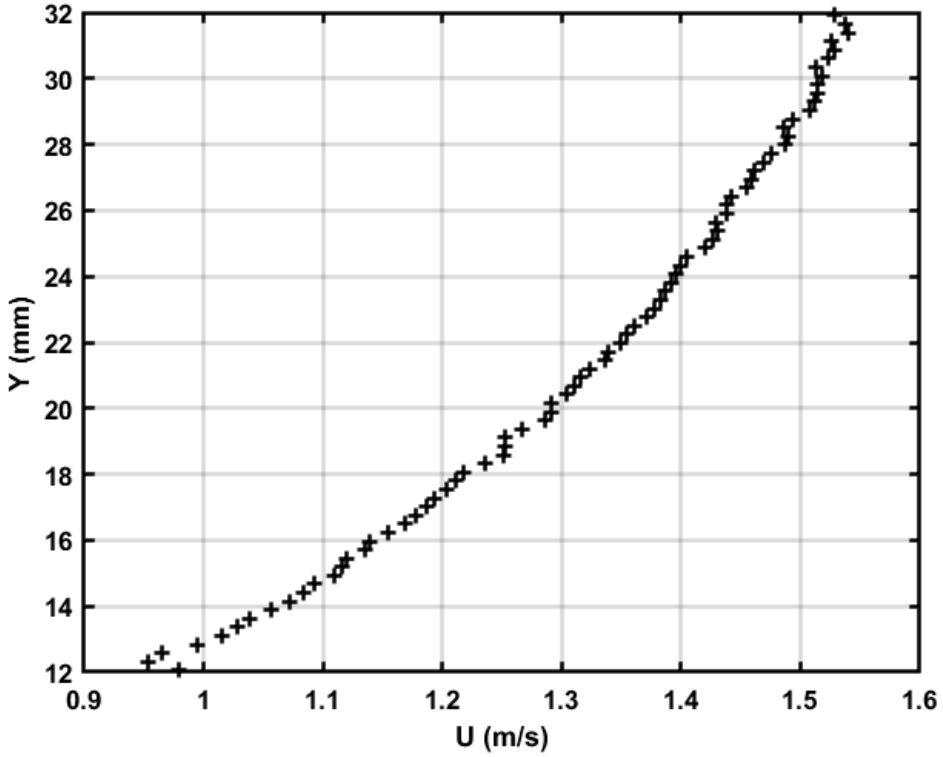


**Figure 4.35** Average velocity profile in Test 1

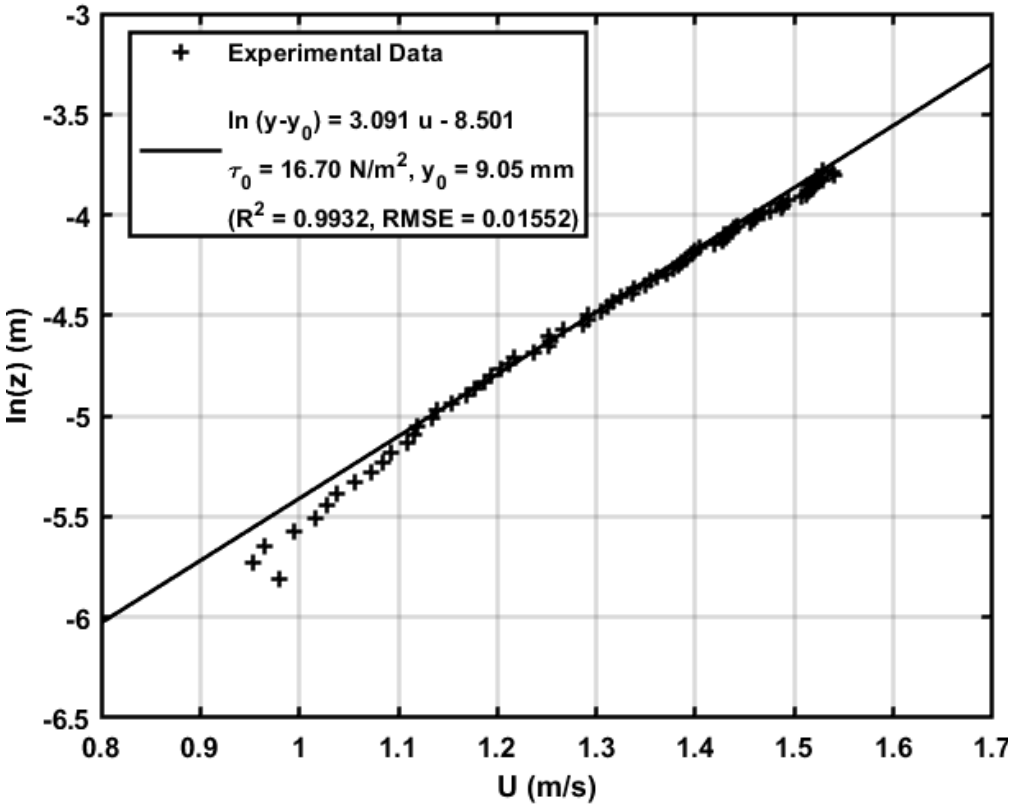


**Figure 4.36** Semi log plot of the average velocity profile in Test 1

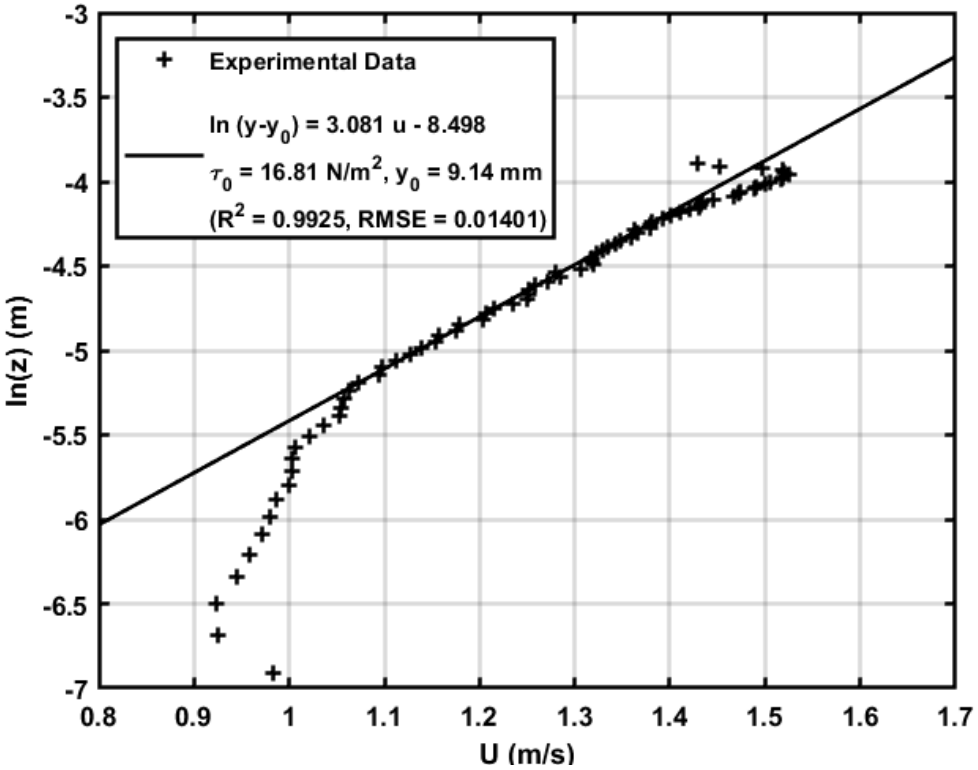


**Figure 4.37** Semi log plot of the average velocity profile in Test 2

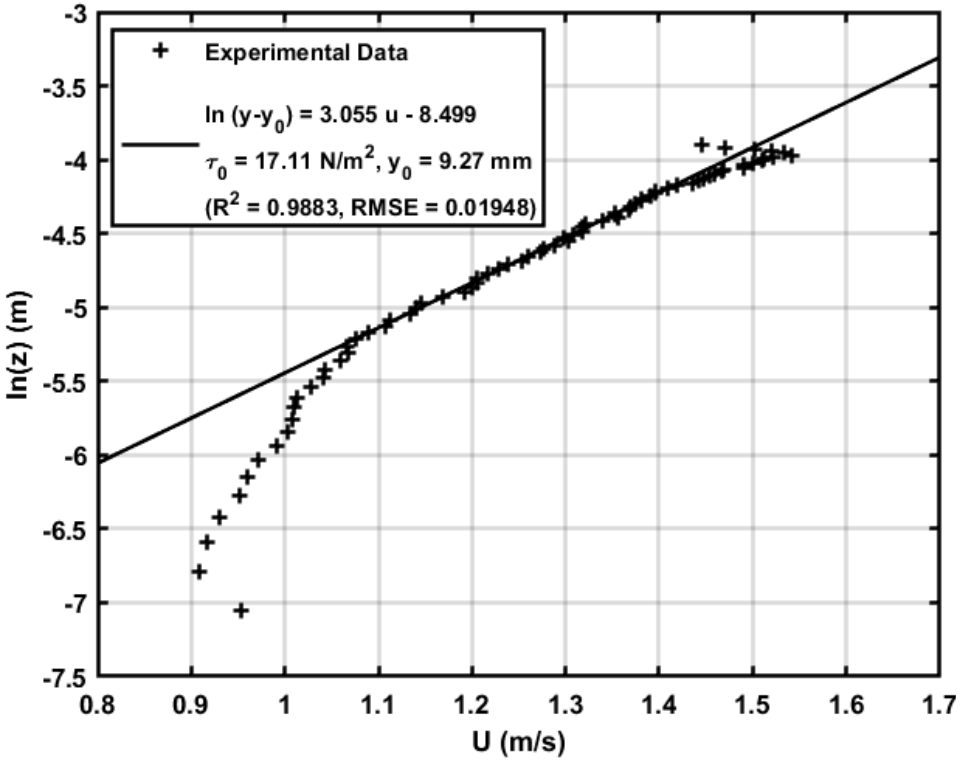


**Figure 4.38** Semi log plot of the average velocity profile in Test 3

**Table 4.4** Summary results of bed shear stress measurements with soil surface flush with top of gravel bed

| Test | $h$ (mm) | $h_c$ (mm) | $y_0, y_1, y_2$ (mm) | $V$ (m/s) | $V_1$ (m/s) | $\tau_{b1}$ (N/m²) | $\tau_{b2}$ (N/m²) | $\tau_{b2}$ [95% CI] | Percent Difference |
|---|---|---|---|---|---|---|---|---|---|
| 1 (4) | 26.80 | 24.00 | 9.05, 11.4, 26.8 | 1.22 | 1.22 | **17.40** | **16.70** | 14.22 - 19.73 | 4.0% |
| 2 (4) | 26.80 | 24.00 | 9.14, 9.5, 26.8 | 1.22 | 1.22 | **17.4** | **16.81** | 13.44 - 21.02 | 3.4% |
| 3 (4) | 26.80 | 24.00 | 9.27, 9.5, 26.8 | 1.22 | 1.23 | **17.4** | **17.11** | 13.26 - 22.07 | 1.6% |

Table 4.4 shows a summary of the bed shear stress measurements obtained in this set of experiments. The top of the cohesive sediment sample was about level with the top of the gravels fixed to the bed surrounding the sediment recess. These results show that the bed shear stress obtained from the measured velocity profile on the clay bed, $\tau_{b2}$, is slightly smaller than, but close to, the bed shear stress obtained from the depth-slope method on the gravel bed, $\tau_{b1}$.

### 4.3.2 Bed Shear Stress at Different Soil Erosion Depths

The soil specimen was trimmed to various depths below the top of the surrounding fixed gravel bed in the hydraulic channel. The soil specimen was trimmed rather than naturally eroded because the water would otherwise become too cloudy for good PIV measurements. The results indicate that as the erosion depth gets larger, the bed shear stress in the test area determined from the measured average velocity profile would eventually decrease.

An example of the captured PIV images from Test 4 (see Table 4.5) can be seen in Figure 4.39, and the corresponding ensemble correlation velocity field is shown in Figure 4.40. PIV images from other tests can be found in Appendix C.

Multiple runs were conducted in each test and the measured velocity profiles were averaged to obtain an average velocity profile to determine the bed shear stress. Figure 4.41 shows an example of the average velocity profile from Test 4. The average velocity profiles from other tests can be found in Appendix D.

Plots of $\ln(y - y_0)$ versus $u$ for the different tests are shown in Figures 4.42 through Figure 4.53 with the summary of bed shear stress results in Table 4.5. As in Section 4.3.1, the value of $y_0$ for the best-fit line in each plot was found assuming that the equivalent bed roughness height, $k_s$, is equal to 6.1 mm, or $d_{65}$ of the fixed gravel bed.

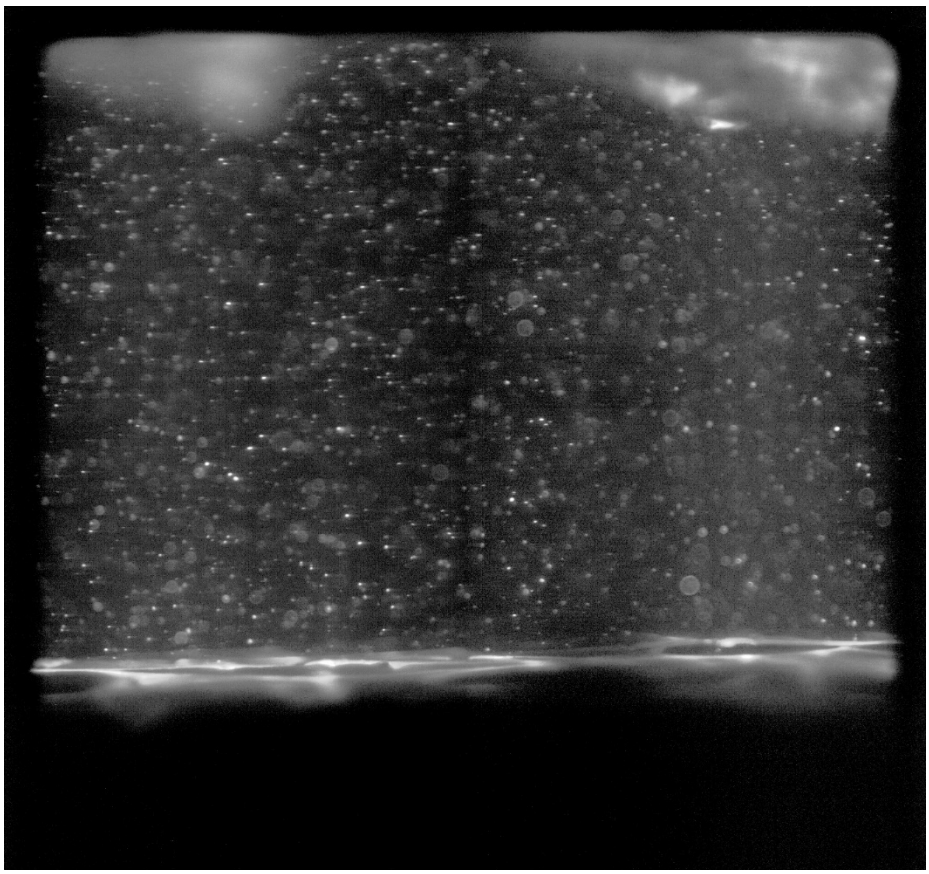

**Figure 4.39** Example of a raw PIV image from Test 4

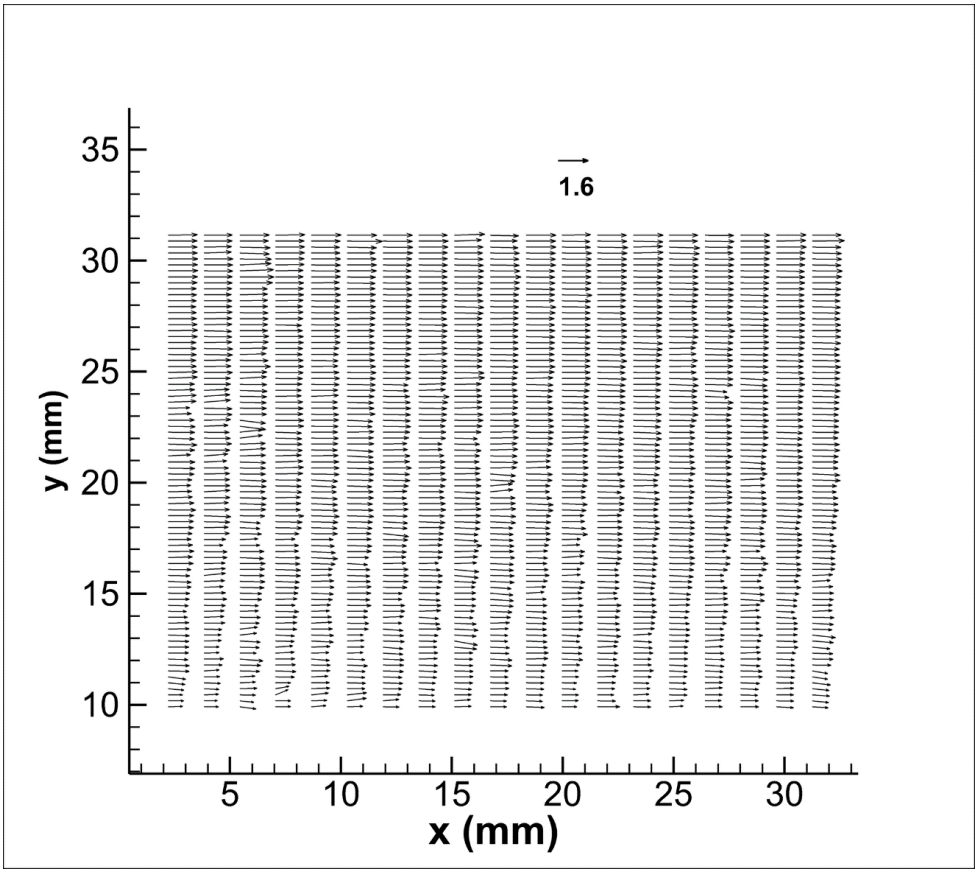


**Figure 4.40** Velocity profiles of processed data from Test 4

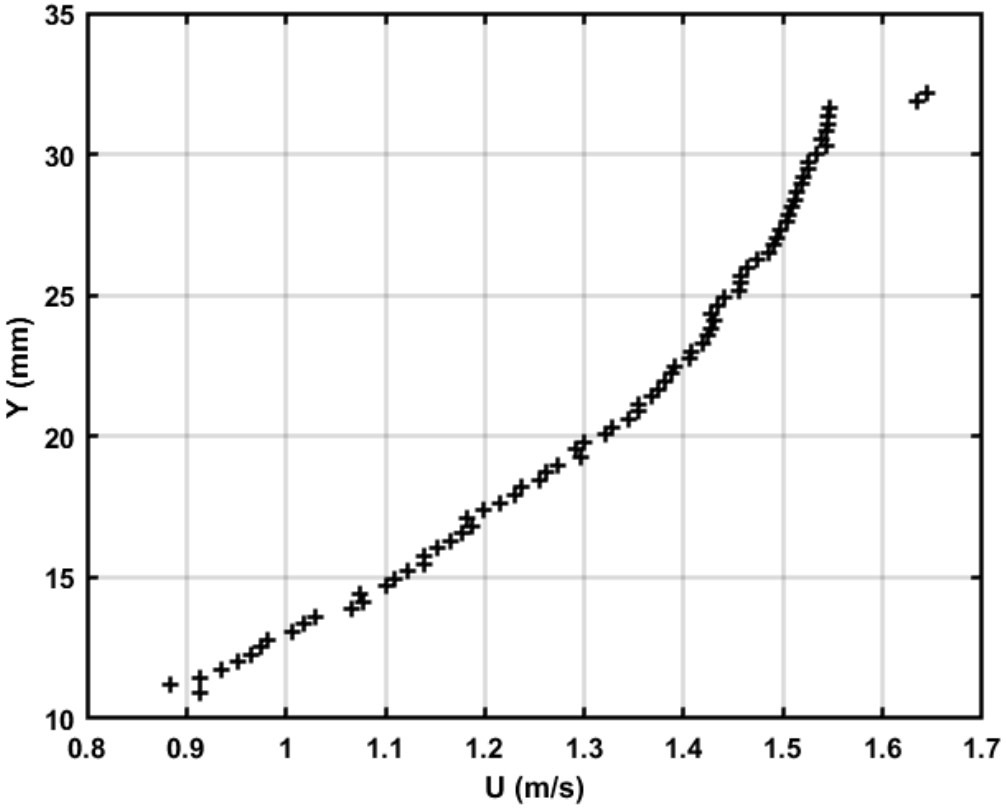


**Figure 4.41** Average velocity profile from Test 4

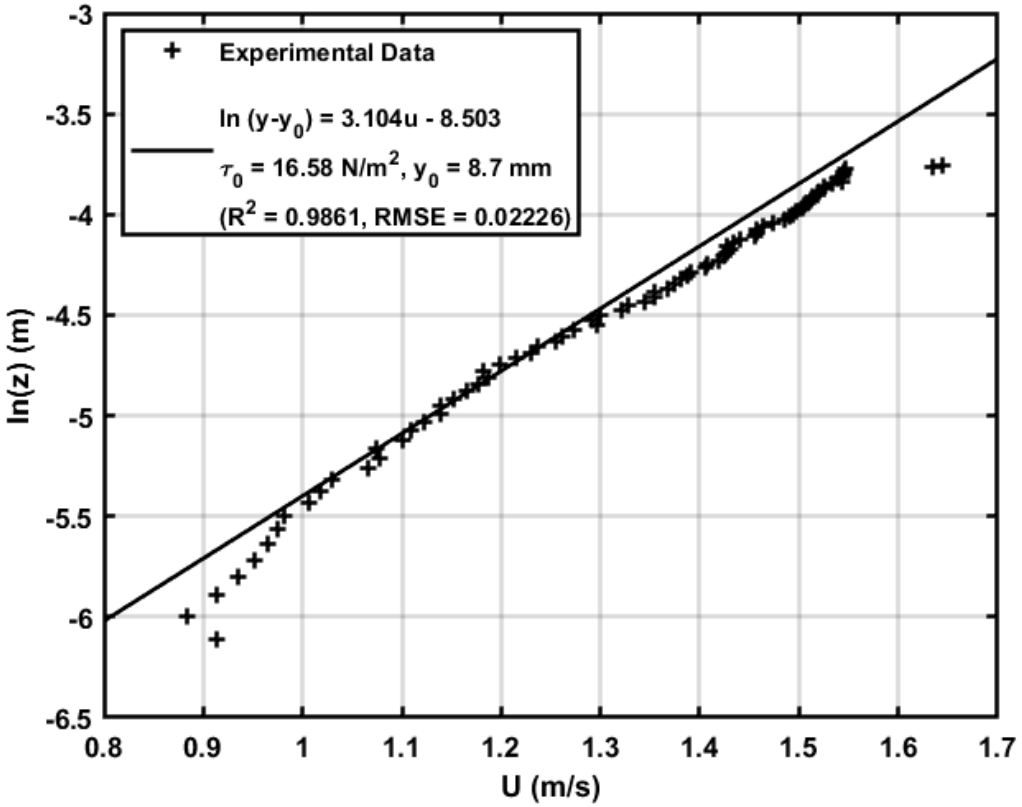


**Figure 4.42** Semi log plot of average velocity profile for 1.5 mm soil erosion depth from Test 4

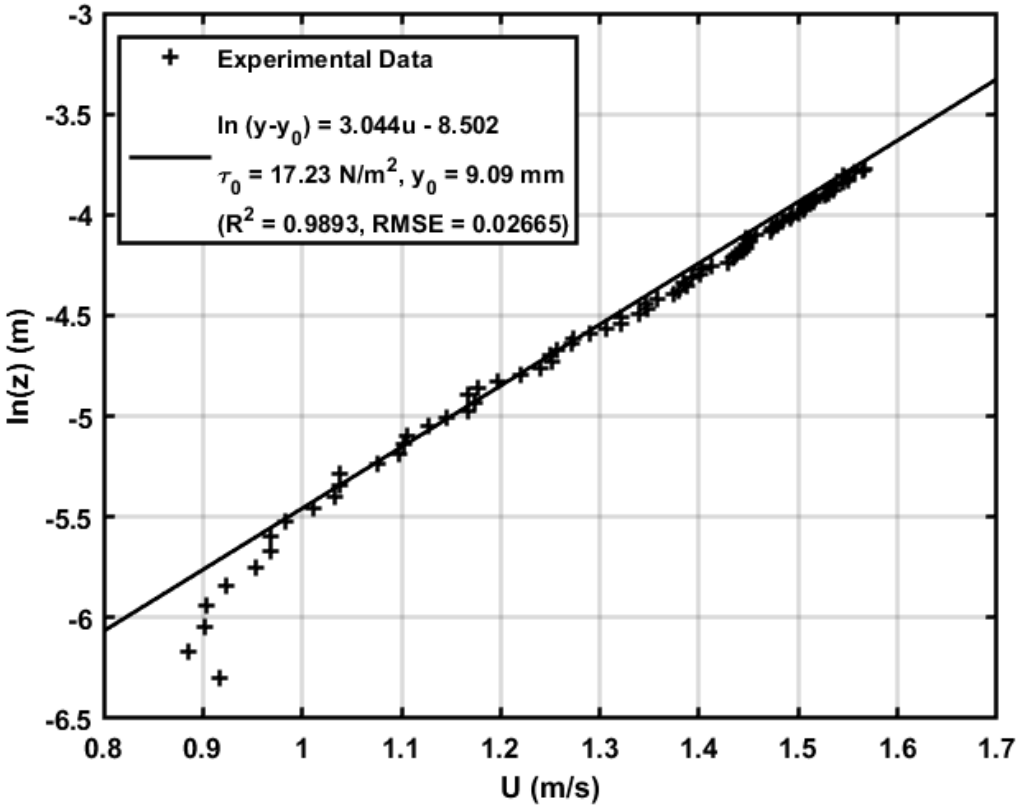


**Figure 4.43** Semi log plot of average velocity profile for 1.5 mm soil erosion depth from Test 5

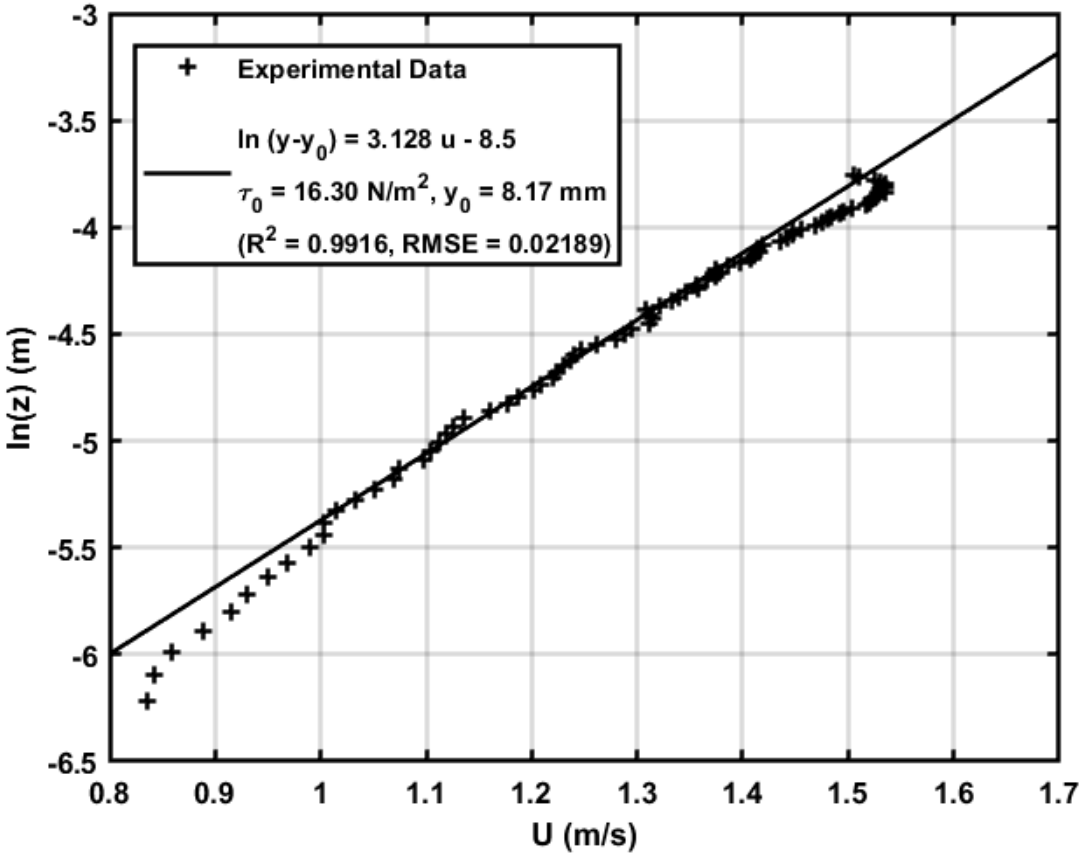


**Figure 4.44** T Semi log plot of average velocity profile for 1.6 mm soil erosion depth from Test 6

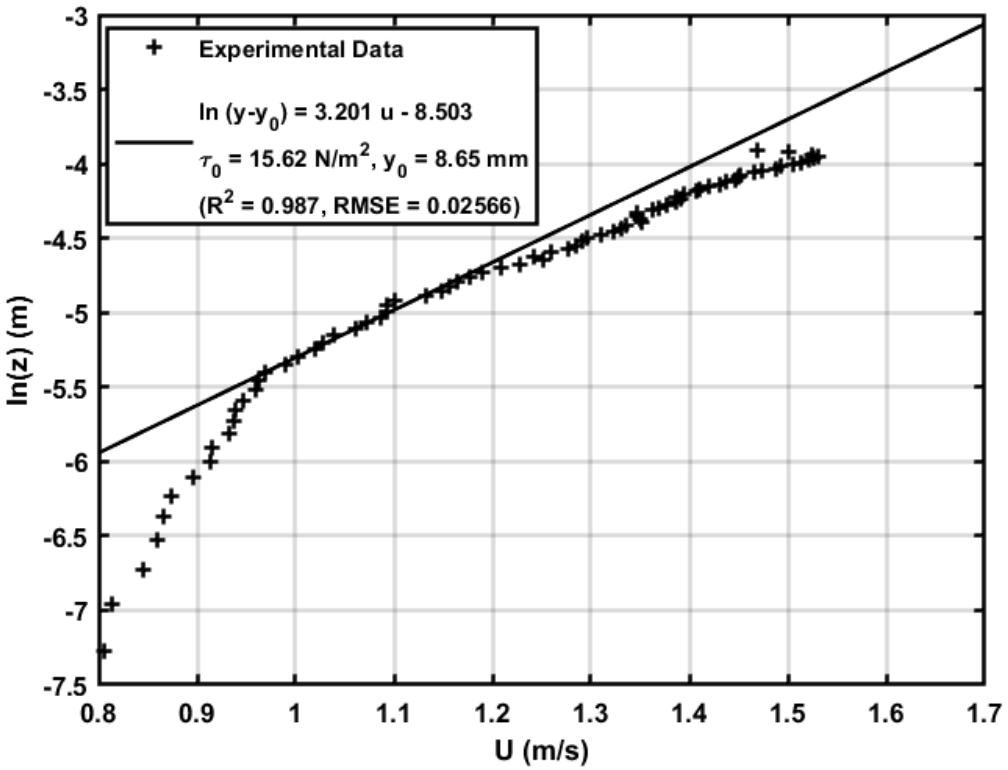


**Figure 4.45** Semi log plot of average velocity profile for 1.6 mm soil erosion depth from Test 7

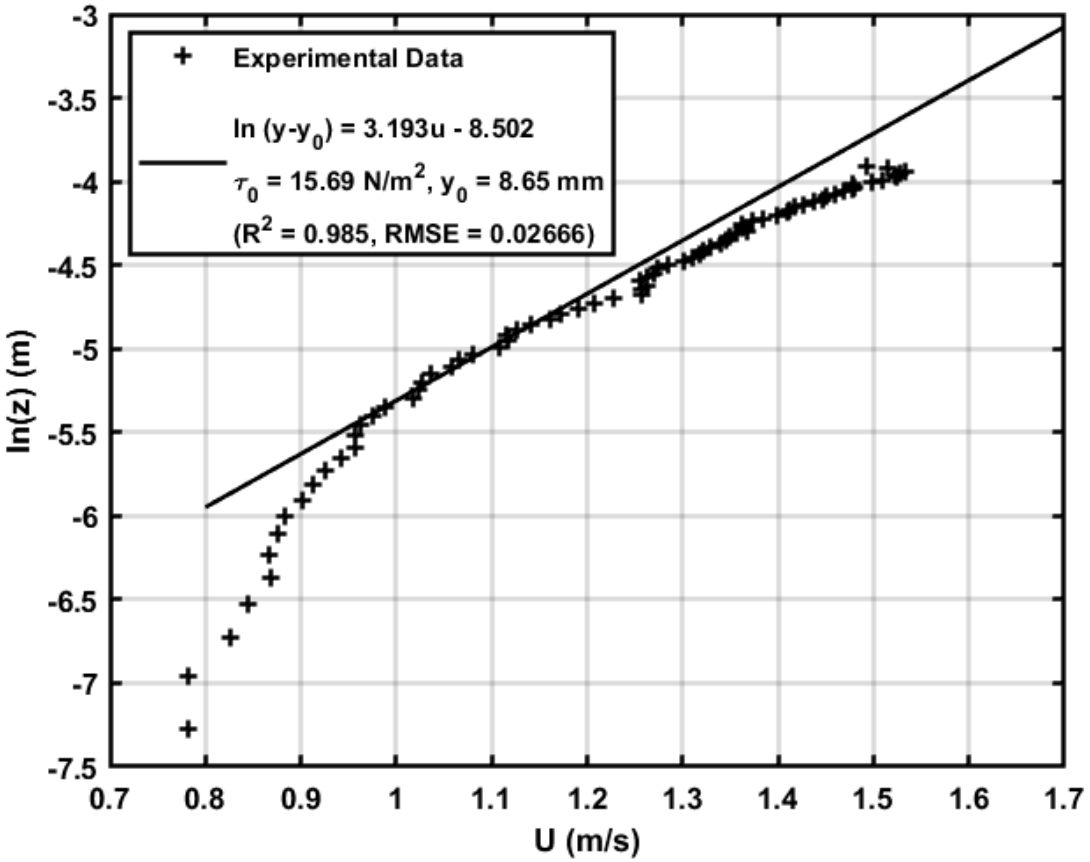


**Figure 4.46** Semi log plot of average velocity profile for 1.6 mm soil erosion depth from Test 8

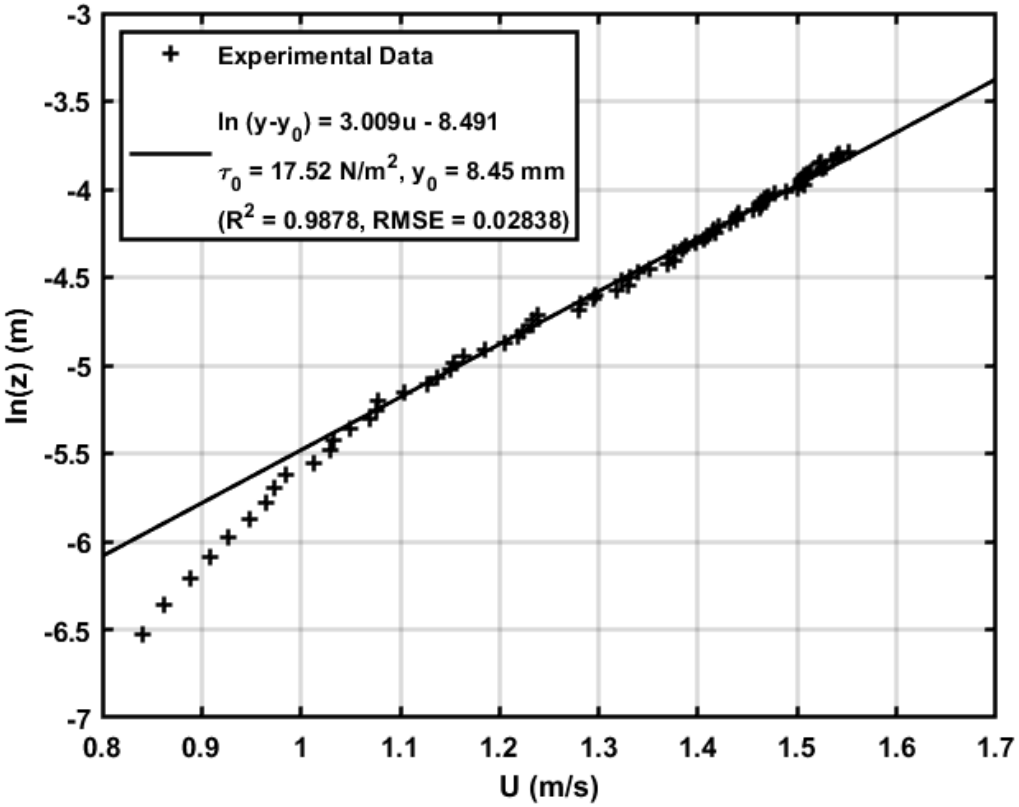


**Figure 4.47** Semi log plot of average velocity profile for 2.5 mm soil erosion depth from Test 9

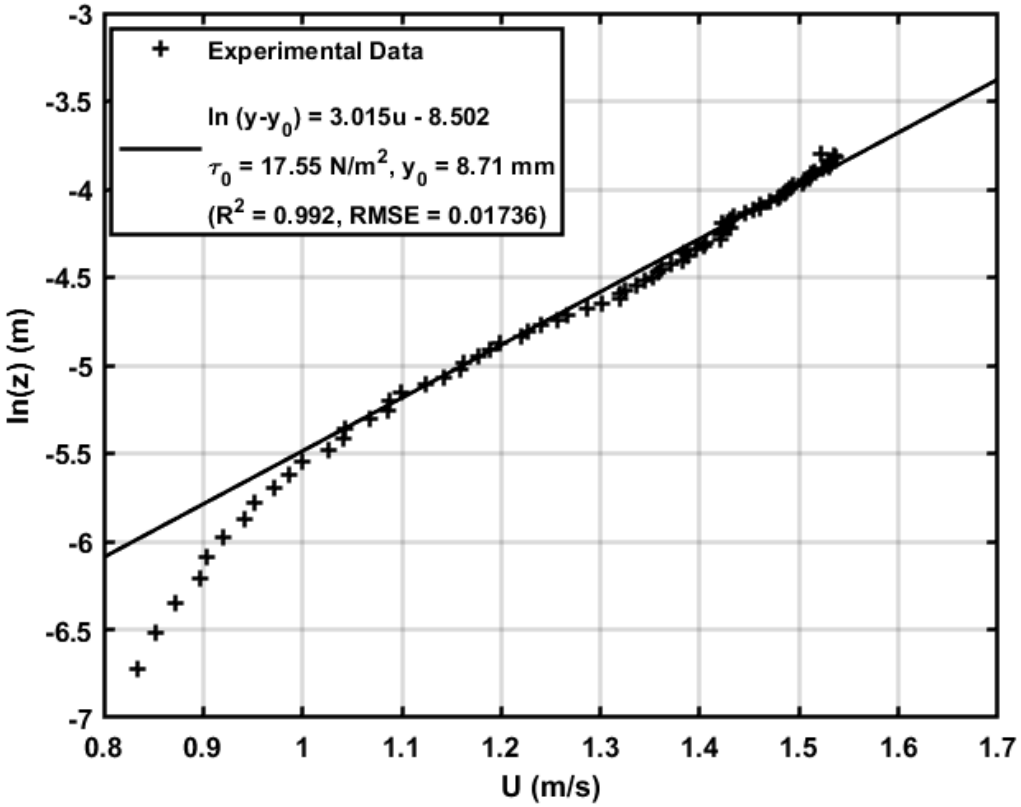


**Figure 4.48** Semi log plot of average velocity profile for 2.5 mm soil erosion depth from Test 10

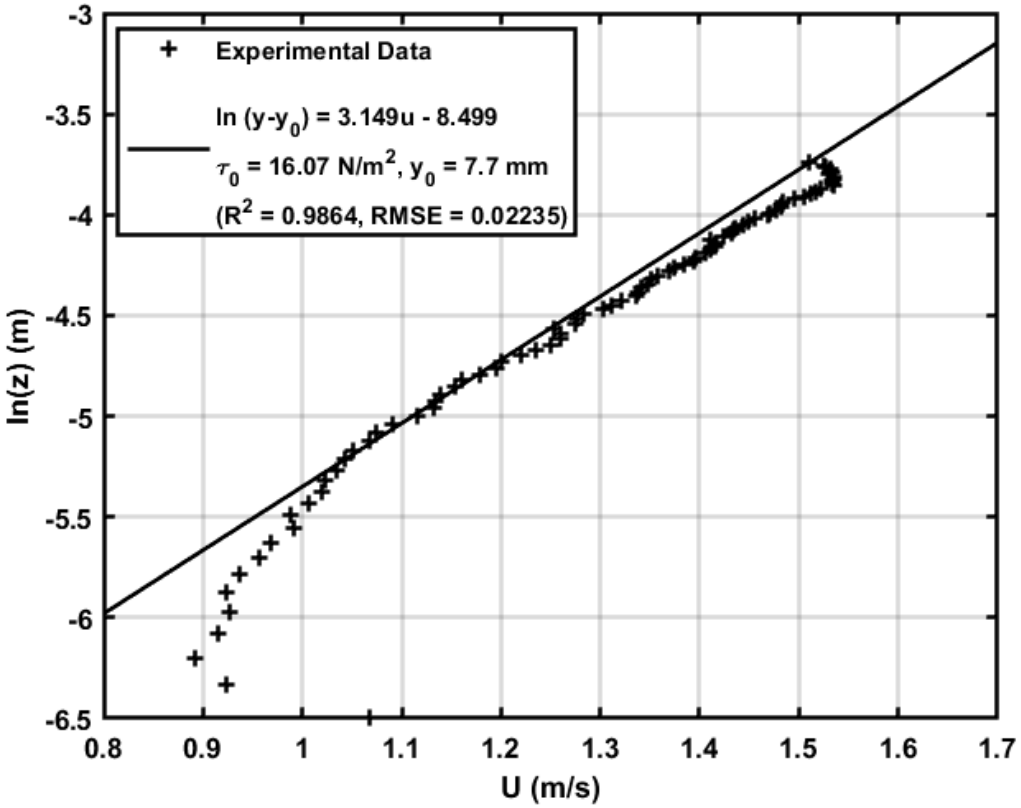


**Figure 4.49** Semi log plot of average velocity profile for 3 mm soil erosion depth from Test 11

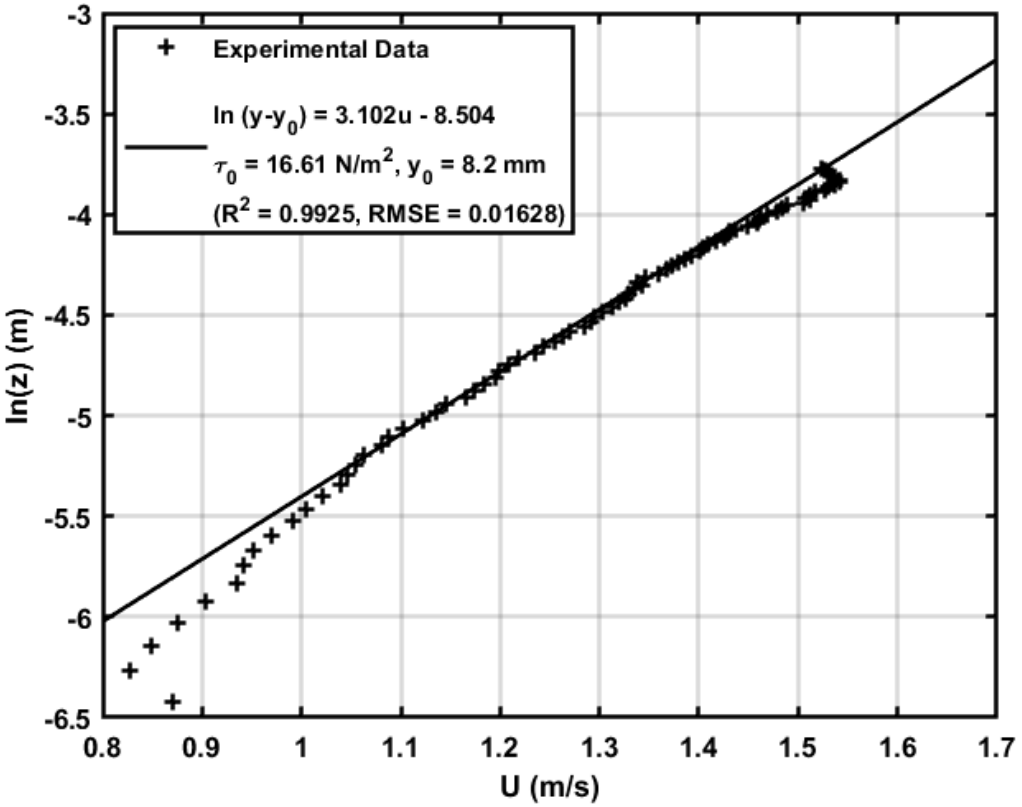


**Figure 4.50** Semi log plot of average velocity profile for 3 mm soil erosion depth from Test 12

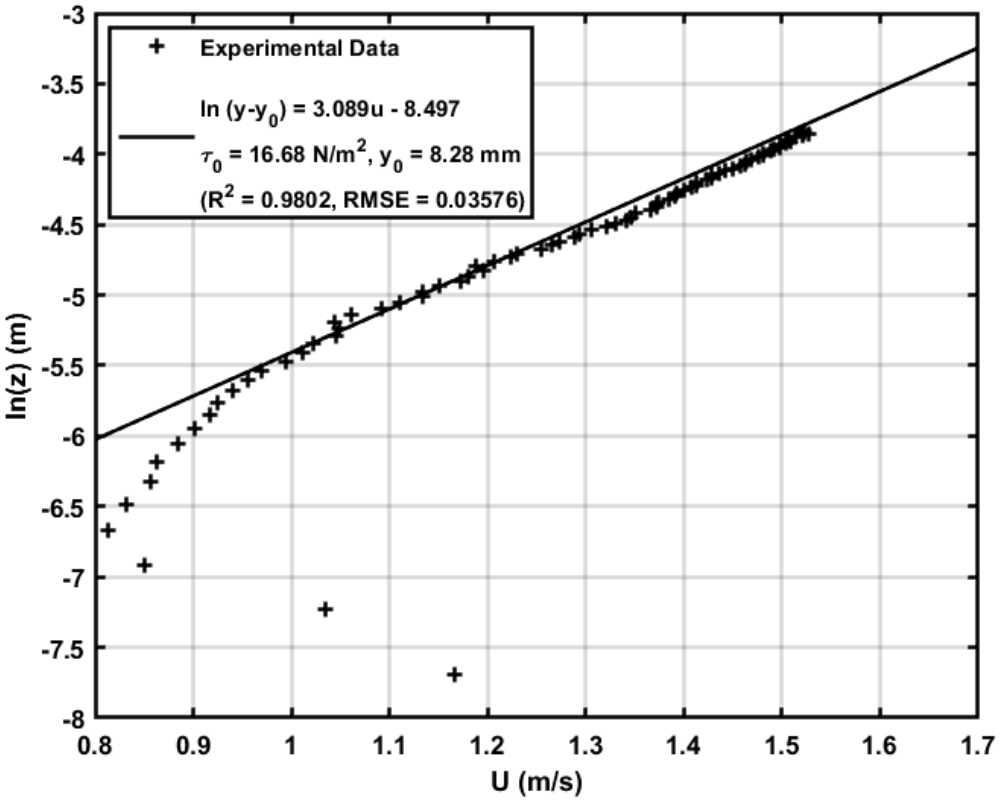


**Figure 4.51** Semi log plot of average velocity profile for 4 mm soil erosion depth from Test 13

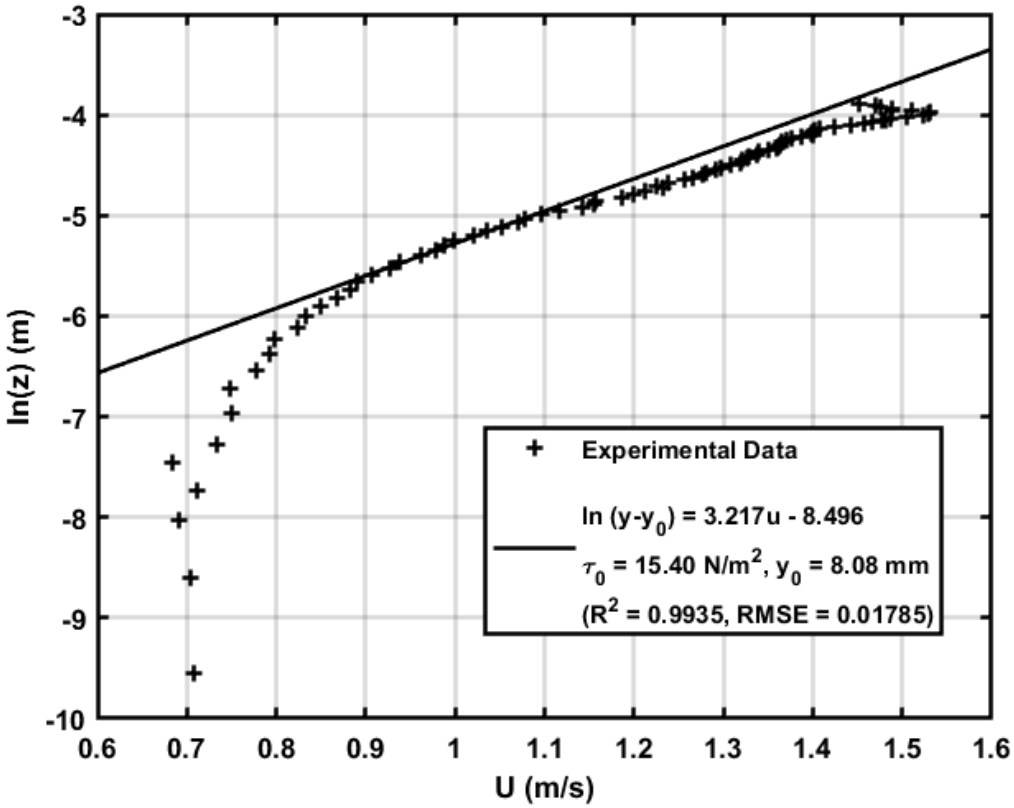


**Figure 4.52** Semi log plot of average velocity profile for 4 mm soil erosion depth from Test 14

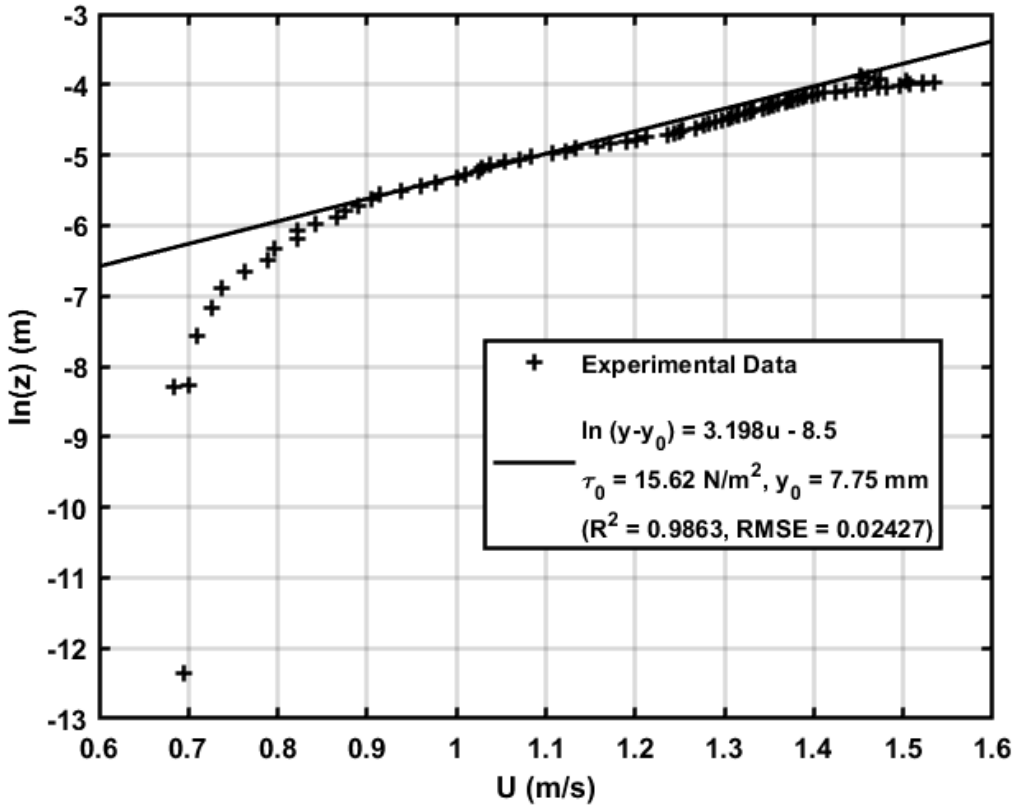


**Figure 4.53** Semi log plot of average velocity profile for 5 mm soil erosion depth from Test 15

**Table 4.5** Results of PIV measurements over different soil erosion depths

| (1) Test | (2) Erosion Depth (mm) | (3) $h$ (mm) | (4) $h_e$ (mm) | (5) $y_0, y_1, y_2$ (mm) | (6) $V$ (m/s) | (7) $V_1$ (m/s) | **(8) $\tau_{b1}$ (N/m$^2$)** | **(9) $\tau_{b2}$ (N/m$^2$)** | (10) $\tau_{b2}$ [95% CI] | (11) Percent Difference |
|---|---|---|---|---|---|---|---|---|---|---|
| 1 (4) | 0 | 26.80 | 24.00 | 9.05, 11.4, 26.8 | 1.22 | 1.22 | **17.40** | **16.70** | 14.22 - 19.73 | 4.0% |
| 2 (4) | 0 | 26.80 | 24.00 | 9.14, 9.5, 26.8 | 1.22 | 1.22 | **17.40** | **16.81** | 13.44 - 21.02 | 3.4% |
| 3 (4) | 0 | 26.80 | 24.00 | 9.27, 9.5, 26.8 | 1.22 | 1.23 | **17.40** | **17.11** | 13.26 - 22.07 | 1.6% |
| 4 (3) | 1.5 | 26.92 | 24.12 | 8.7, 9.5, 26.92 | 1.22 | 1.22 | **17.50** | **16.58** | 12.75 - 21.52 | 5.3% |
| 5 (3) | 1.5 | 26.80 | 24.00 | 9.09, 10.25, 26.8 | 1.22 | 1.24 | **17.40** | **17.23** | 14.28 - 20.77 | 1.0% |
| 6 (4) | 1.6 | 26.92 | 24.12 | 8.17, 9.3, 26.92 | 1.22 | 1.21 | **17.50** | **16.30** | 13.60 - 19.52 | 6.9% |
| 7 (4) | 1.6 | 26.67 | 23.87 | 8.65, 8.7, 26.67 | 1.23 | 1.18 | **17.30** | **15.62** | 12.23 - 19.95 | 9.7% |
| 8 (4) | 1.6 | 26.67 | 23.87 | 8.65, 8.7, 26.67 | 1.23 | 1.18 | **17.30** | **15.69** | 11.94 - 20.63 | 9.3% |
| 9 (3) | 2.5 | 26.80 | 24.00 | 8.45, 9.1, 26.8 | 1.22 | 1.25 | **17.40** | **17.52** | 14.17 - 21.63 | -0.7% |
| 10 (3) | 2.5 | 26.67 | 23.87 | 8.71, 9.1, 26.67 | 1.23 | 1.25 | **17.30** | **17.56** | 14.12 - 21.81 | -1.5% |
| 11 (4) | 3 | 26.80 | 24.00 | 7.7, 8.1, 26.8 | 1.22 | 1.20 | **17.40** | **16.07** | 12.22 - 21.13 | 7.7% |
| 12 (6) | 3 | 26.80 | 24.00 | 8.2, 8.1, 26.8 | 1.22 | 1.22 | **17.40** | **16.61** | 13.56 - 20.34 | 4.6% |
| 13 (4) | 4 | 26.92 | 24.12 | 8.28, 8.4, 26.924 | 1.22 | 1.22 | **17.51** | **16.68** | 12.45 - 22.32 | 4.7% |
| 14 (6) | 4 | 26.67 | 23.87 | 8.08, 6.1, 26.67 | 1.23 | 1.17 | **17.30** | **15.40** | 12.64 - 18.77 | 11.0% |
| 15 (6) | 5 | 26.67 | 23.87 | 7.75, 5.7, 26.67 | 1.23 | 1.18 | **17.30** | **15.62** | 11.67 - 20.91 | 9.7% |

Table 4.5 shows a summary of all the PIV experiment results over a cohesive sediment sample. The percent differences between $\tau_{b1}$ and $\tau_{b2}$ are small when the erosion depth in the sediment recess is zero (Tests 1 to 3), and they are within the uncertainties of the bed shear stress measurements. As seen in Table 4.5, Column (10), the bed shear stress differences are within the 95% confidence interval of the measurements.

Tests 11, 12, 13, 14, and 15 have a 3 to 5 mm erosion depth. The results show that $\tau_{b2}$ is consistently smaller than $\tau_{b1}$. This may be expected as the erosion depth increases, as with the bed shear stress at the bottom of a deepening scour hole. Larger erosion depth may result in a lower $\tau_{b2}$ value because the turbulence intensity in the sediment recess would eventually decrease. Tests 14 and 15 produce the lowest $\tau_{b2}$ values and the highest percent difference compared with $\tau_{b1}$.

It can also be seen in Table 4.5 that the velocity, $V$, calculated using the measured discharge and flow depth is close to the depth-averaged velocity, $V_1$, obtained from the measured velocity profile.

# 5. DISCUSSION

Two related research problems were investigated in this laboratory study. The first was to examine the correlations of unconfined compressive strength with the soil critical shear stress and erosion rate. The second was to test a different experimental setup for an EFA type device to determine the bed shear stress and measure the soil erosion rate. The velocity profiles over a rough bed and an embedded soil sample were measured to estimate the bed shear stress using the logarithmic law (log law). An improved procedure was developed to determine the displacement height that would reduce the uncertainty in finding the bed shear stress over a rough bed.

The EFA devices developed by Briaud et al. (2001a) and improved by Shan et al. (2012) measure the soil erosion rate and bed shear stress of a clay sample in a water tunnel with smooth walls. The device used in the present study was a tilting flume with a rough bed made of a single layer of gravel. The motivation for using a rough bed was to increase the intensity of the boundary-layer turbulence, which would increase the bed shear stress and thus the measurable soil erosion rates. In addition, the bed shear stress in a tilting flume can be determined relatively accurately using the measured flow depth and channel slope or measured velocity profile.

The flow over the sediment recess involves a step change in surface roughness (from rough-to-smooth-to-rough). Flow over a sudden change in surface roughness has been studied mainly in external (e.g., atmospheric boundary layer) and internal (e.g., close conduit) flows. A recent literature review can be found in Kadivar et al. (2021). When a flow encounters a sudden change in surface roughness, an internal boundary layer will start at the roughness transition and grow outward from the wall with distance downstream. If the surface downstream is of sufficient length, a new fully developed turbulent boundary layer will be established eventually. Previous studies indicate that the wall shear stress would attain its new equilibrium value promptly, but flow quantities outside the internal boundary layer are determined by conditions before the transition and would change only gradually with distance downstream. For a rough-to-smooth (RTS) transition, experimental and numerical studies have found that the wall shear stress would be underestimated if obtained from the mean velocity profile measured outside the internal layer (e.g., Antonia and Luxton, 1972; Loureiro et al. 2010; Li et al. 2019). This suggests that the log law may be applied with a measured velocity profile to provide a conservative estimate of the bed shear stress on the soil surface in the sediment recess.

In addition to the bed shear stress associated with the mean flow, the soil surface was also subject to strong near-bed turbulence. The time it took for the flowing water to pass over the sediment recess was very short (< 0.1 seconds). Consequently, the structure of turbulence over the soil sample, which determines the vertical turbulent transport of streamwise fluid momentum and shear stress distribution, would be controlled primarily by the boundary-layer turbulence generated on the gravel bed upstream. The “external” turbulence then impinges on the soil surface resulting in an increase in the instantaneous bed shear stress and erosion rate. On a smooth bed, this effect may be parameterized using an “apparent roughness” analogous to the equivalent roughness on a rough bed (see Fredsøe et al., 2003). In the experimental setup employed in this study, a logical choice of this apparent roughness would be the roughness of the gravel bed surrounding the clay sample. The latter is a reasonable assumption if the soil sample has a rough surface like the surrounding gravels, which may be accomplished by introducing artificial indentations in the clay sample.

In previous EFA studies, the soil sample was protruded into the flow by a piston system. The faster the piston advances, the larger the drag forces on the soil sample and thus the faster the erosion rate. Consequently, there are high uncertainties in the measured erosion rates. In the present study, the soil sample was set at a fixed height and eroded for a specific amount of time to minimize subjectivity that

could cause error from a human deciding when to advance the sample. The erosion rate was determined by weighing the soil sample before and after the test. The disadvantage of this method is that only one erosion rate can be measured for each soil sample tested, so that the same procedure must be repeated many times to establish the erosion-rate-versus-shear-stress curve. The results from these tests showed that as the bed shear stress increased, so did the measured average erosion rate.

The erosion rate of cohesive soil has been found to be related to the unconfined compressive strength in previous studies. Similar results were found in this study. The results show that as the soil unconfined compressive strength increased, the erosion rate decreased. Although there was much scatter in the measured data, the resulting trend was like those found in previous studies. Because the unconfined compressive strength was varied in this study by changing the water content only, the water content may be used instead of the unconfined compressive strength to determine the soil erodibility.

The erosion pattern of cohesive soils is unpredictable, and the soil surface developed a rough texture as chunks eroded from the specimen. Crowley et al. (2012, 2014) showed that the shear stress over a cohesive soil increases as the soil surface erodes. Thus, the bed shear stress cannot be determined accurately using indirect methods such as the Colebrook equation for pipe flows; it must be measured directly on the eroding sample. A rough bed was installed in a tilting flume to investigate if the bed shear stress acting on a clay bed could be controlled more carefully in open-channel flows. The rough bed results, presented in Section 4.2 and 4.3, show no significant differences between the estimated bed shear stress on the eroding clay sample and the surrounding gravel bed when the same equivalent roughness is used. These results suggest that the bed shear stress acting on an eroded clay sample may be controlled by changing the channel slope and roughness of the surrounding rough bed and measured using methods developed for open-channel flows.

It is well known that soil erodes in flowing water until the bed shear stress ($\tau_b$) is equal to the soil's critical shear stress ($\tau_c$). This implies that the time-rate-of-scour would decrease as the surface of the soil sample recedes deeper into the surrounding bed. This was observed in Shan et al. (2012). His measurements show, using direct force measurements, that the measured shear stress decreases with increasing erosion depth. Similar results were found in this present study. Velocity profile over the soil sample was measured using the PIV technique, and the log law was used to estimate the bed shear stress. Table 4.5 shows that there were no significant changes in the resulting bed shear stress obtained from the measured average velocity profile until the erosion depth was greater than about 3 to 4 mm.

The modified logarithmic law method used in this study to determine bed shear stress can produce more consistent results than the traditional method. The alternative method assumes a value for the equivalent roughness, $k_s$, which remains constant for a given flow-depth-to-grain-diameter ratio. Various $k_s$ values for the gravel bed were evaluated. The resulting bed shear stress shows that a $k_s$ value of $d_{84} = 7$ mm produced the best agreement with the bed shear stress calculated using the measured flow depth and channel slope in most cases, while the $d_{65}$ may be a better choice for the equivalent roughness height at smaller flow-depth-to-grain-diameter-ratios.

The method adopted in this study to determine the bed shear stress from a measured velocity profile assumes that the value of $k_s$ is known. The $k_s$ value can be found by comparing the results with the bed shear stress calculated from the measured flow depth and channel slope in a uniform flow. Kamphuis (1973) used this approach to determine the equivalent roughness for a wide range of $h/d_{90}$ ratios. His results show that the ratio of $k_s/d_{90}$ may be taken as 2.5 when the $h/d_{90}$ ratio is greater than 20. The value decreases rapidly when the $h/d_{90}$ ratio is less than 10, which suggests that the flow depth is an important factor in determining the equivalent roughness at the small $h/d_{90}$ ratios. In this study, new experiments were performed to determine the $k_s/d_{90}$ values over a range of $h/d_{90}$ ratios between 3.6 and 5.6. The results show that the value of $k_s/d_{90}$ is around 0.76 at the low end of the $h/d_{90}$ ratio in good agreement with the findings by Kamphuis (1973).

# 6. SUMMARY AND CONCLUSIONS

This study has examined several modifications to the existing EFA type devices and presented an alternative method for finding the bed shear stress on a rough bed by using a measured velocity profile and the logarithmic law. The major findings and main conclusions of the study are given as follows.

Several EFA type devices have been developed by researchers to measure soil erosion rates. These devices use a water tunnel or open channel with smooth walls, which may not simulate the actual turbulent flow conditions over an eroding soil surface in rivers and streams. The hydraulic channel in the present study used a fixed gravel bed to simulate the turbulent flow environment on a more natural channel bottom. The flow measurements conducted in this study showed that the bed shear stress increased substantially when bed roughness was introduced. Two different methods were used to determine the bed shear stress, the depth-slope method with sidewall correction described in Section 3.6 and the log law method described in Sections 4.2 and 4.3, and the results were compared. When the measured velocity profiles were used with the same equivalent roughness and the log law method to determine the bed shear stresses on the clay sample and surrounding gravels, the results were found to be similar for soil recess depth up to about the grain diameter of the gravels. Thus, the bed shear stress acting on a clay sample may be increased using artificial roughness in an open-channel flume and varied by adjusting the channel slope and/or flow velocity.

In previous studies, the soil property found to have a significant effect on erosion rate was the unconfined compressive strength, $Q_u$. This study focused on varying this parameter while holding other soil properties mostly unchanged. The results showed much scatter, but the trend showed that as $Q_u$ decreased the average erosion rate of the soil increased. Since the unconfined compressive strength is closely related to the water content, the latter is an important parameter in determining the erodibility of cohesive soils.

The alternative method developed for finding bed shear stress from the measured velocity profile assumes that the von Kármán constant ($\kappa$-value) is a universal constant with a value around 0.4 and the equivalent grain roughness ($k_s$) is known. Using the PIV technique, the time-averaged velocity profile was measured and graphed on a plot of $\ln(y\text{-}y_0)$ versus $u$. The displacement height, $y_0$, was varied until the $\kappa$ value obtained from the $y$-intercept of the best straight-line fit was equal to 0.4. The friction velocity, $u^*$, was then found from the slope of the best-fit line. This method reduces the variations in bed shear stress determined by varying $y_0$ and $k_s$ simultaneously. The traditional method of optimizing the log-law fitting by trial and error can produce a wide range of bed shear stress and equivalent roughness heights. The alternative method converges rapidly with a smaller range of bed shear stress variations. The method was applied to a steady, uniform flow over a fixed gravel bed where the $h/d_{90}$ ratio was varied between 3 and 6. It was found that the log law represented the measured velocity profile through almost the entire flow depth. The bed shear stress values obtained using the modified log law method and calculated from the measured flow depth and channel slope were compared, and it was found that $k_s$ can be approximated by $d_{84}$ or smaller diameter ($d_{65}$) for small values of the $h/d_{90}$ ratio, in agreement with the experimental results of Kamphuis (1974).

The modified log law method was used to find the bed shear stress on a sudden, short transition of bed roughness created by placing a clay sample in a sediment recess in a fixed gravel bed. The same procedure was followed, and the results showed that the bed shear stress determined using the measured velocity profile did not change significantly over the clay sample when the equivalent roughness was held at the same value as the surrounding gravels. PIV measurements were then conducted over recessed clay samples trimmed to different specified depths. It was found that the bed shear stress on the clay sample was about 5% to 10% smaller than the bed shear stress on the gravel bed upstream for soil recess depths up to about 5.6 mm, or $d_{50}$, of the fixed gravel bed.

# 7. RECOMMENDATIONS FOR FUTURE RESEARCH

This study has investigated a different experimental setup to measure the erosion rate of cohesive soils. The design used a tilting flume with a circular recess in a gravel bed to accommodate a cylindrical soil sample 1.5 in. high and 2.75 in. in diameter. The velocity profiles over the gravel bed and soil sample were measured to determine the bed shear stress using the logarithmic law (log law) method. The motivation for using a rough bed instead of a channel with smooth walls was to increase the level of turbulence in the flow, which would in turn increase the bed shear stress that can be exerted on the soil sample. The study raised the fundamental question of how the bed shear stress would develop in a sudden transition of bed roughness in flows with a free surface. The problem had received little attention until the recent work of Jamil (2023), which examines the variations of bed shear stress in rough-to-smooth (RTS) and smooth-to-rough (STR) transitions under various composite water surface profiles. His experimental study shows that bed shear stress variations after roughness transitions consistent with published data can be obtained when the $k_s/d_{90}$ ratio is determined as a function of the $h/d_{90}$ ratio, as described in this report. Future work will study the momentum and turbulent energy balance to gain a deeper understanding of the growth of the internal boundary layer through roughness transitions, including the installation of bed shear stress sensors on the smooth bed after an RTS transition to verify the bed shear stress values obtained using other methods.

The present study has investigated an experimental setup to induce the bed shear stress over a cohesive soil sample using an open channel flume and a rough bed. The experimental setup was tested using soil samples prepared from Nora Moody clay. Future work would include testing actual soil samples collected from bridge sites and using the measured soil erosion functions to evaluate bridges for scouring. A wide range of bed shear stresses may be produced to induce soil erosion by adjusting the flow discharge and slope of the hydraulic channel.

# 8. REFERENCES


Antonia, R. A., and Luxton, R. E. (1972). "The response of a turbulent boundary layer to a step change in surface roughness. Part 2. Rough-to-smooth." *Journal of Fluid Mechanics*, 63(4), 737-757.

Arneson, L. A., Zevenbergen, L. W., Legasse, P. F., and Clopper, P. E. (2012). "Evaluating scour at bridges." Fifth Edition, *Hydraulic Engineering Circular No. 18*, Federal Highway Administration, Washington, D. C.

ASTM (1997). "ASTM D422 – 63: "Standard Test Method for Particle Size Analysis of Soils." *American Society of Testing Materials* (ASTM), 1997.

ASTM (1997). "ASTM D698 – 91: "Test Method for laboratory Compaction Characteristics of Soil Using Standard Effort (12,400 ft-lbf/ft$^3$ (600kN-m/m$^3$))." *American Society of Testing Materials* (ASTM), 1997.

ASTM (1997). "ASTM D2166 – 91: "Standard Test Method for Unconfined Compressive Strength of Cohesive Soil." *American Society of Testing Materials* (ASTM), 1997.

ASTM (1997). "ASTM D1140 – 92: Standard Test Method for Amount of Material in Soils Finer than the No. 200 (75μm) Sieve." *American Society of Testing Materials* (ASTM), 1997.

Briaud, J.-L., Ting, F., Chen, H.C., Cao, Y., Han, S.W., and Kwak, K.W, (2001a) "Erosion Function Apparatus for Scour Rate Predictions." *Journal of Geotechnical and Environmental Engineering*, ASCE Vol 127, No.2, 105-113.

Briaud, J.-L., Chen, H.C., Kwak K., Han, S.W., and Ting, F.C.K, (2001b) "Multiflood and Multilayer Method for Scour Rate Predictions at Bridge Piers." *Journal of Geotechnical and Environmental Engineering*, ASCE Vol 127, No.2, 105-113.

Briaud, J.-L., Chen, H. C., Li, Y., Nurtjahyo, P., and Wang, J. (2005). "SRICOS-EFA method for contraction scour in fine-grained soils." *Journal of Geotechnical and Geoenvironmental Engineering*, 10.1061/(ASCE)1090-0241(2005)131:10(1283).

Camenen, B., Bayram, A., and Larson, M. (2006). "Equivalent roughness height for plane bed under steady flow." *Journal of Hydraulic Engineering* 132:1146-1158. https://doi.org/10.1061/(ASCE)0733-9429(2006)132:11(1146)

Cheng, N-S (2011). "Revisited Vanoni-Brooks sidewall correction." *International Journal of Sediment Research*., 26, 524-528.

Chow, V. T. (1959). *Open-Channel Hydraulics*. McGraw-Hill Book Company, New York.

Crowley, R. W., Bloomquist, D. B., Hayne, J. R., Holst, C. M., and Shah, F. D. (2012a). "Estimation and measurement of bed material shear stresses in erosion rate testing devices." *Journal of Hydraulic Engineering,* 10.1061/(ASCE)HY.1943-7900.0000608, 990–994.

Crowley, R. W., Bloomquist, D. B., Shah, F. D., and Holst, C. M. (2012b)."The sediment erosion rate flume (SERF): A new testing device for measuring erosion rate and shear stress." *Geotechnical Testing Journal,* 35(4),649–659.

Crowley, R. W., Robeck, C., and Thieke, R. J. (2014)."Computational Modeling of Bed Material Shear Stresses in Piston-Type Erosion Testing Devices." *Journal of Hydraulic Engineering*, American Society of Civil Engineers, Reston, VA.

Fredsøe, J., Sumer, B. M., Kozakiewicz, A., Chua, L. H. C., and Deigaard, R. (2003). "Effect of externally generated turbulence on wave boundary layer." *Coastal Engineering*, 49, 155-183.

Frings, R. M., Schüttrumpf, H., and Vollmer, S. (2011). "Verification of porosity for fluvial and sand-gravel deposits." *Water Resources Research.* 47, W07527, doi: 10.1029/2010WR009690.

INSIGHT 4G™ User's Guide (2011). Insight 4G Global Imaging, Acquisition, Analysis and Display Software. TSI Incorporated.

Jamil, M.F. (2023) "Response of bed shear stress in open-channel flow to a sudden change in bed roughness." M. S. Thesis, Department of Civil and Environmental Engineering, South Dakota State University, Brookings, South Dakota, USA

Kamphuis, J. W. (1973). "Determination of sand roughness for fixed beds." *Journal of Hydraulic Research*, https://doi.org/10.1080/00221687409499737.

Kadivar, M., Tormey, D., and McGranaghan, G. (2021). "A review on turbulent flow over rough surfaces: Fundamentals and theories." *International Journal of Thermofluids*, 10, 1000777.

Li, M., de Silva, C. N., Rouhi, A., Baidya, R., Chung, D., Marusic, I., and Hutchins, N. (2019). "Recovery of wall-shear stress to equilibrium flow conditions after a

rough-to-smooth step change in turbulent boundary layers." *Journal of Fluid Mechanics*, 8 72, 472-491.

Loureiro, J. B. R., Sousa, F. B. C. C., Zotin, J. K. Z., and Silva Freire, A. P. (2010). "The distribution of wall shear stress downstream of a change in roughness." *International Journal of Heat and Fluid Flow*, 31, 785-793.

Middleton, G. V., and Southard, J. (1984). "Mechanics of Sediment Movement." *SEPM for Sedimentary Geology Short Course Number 3*, 2nd edition.

Nikuradse, J. (1933). "Strömungsgesetze in rauhen Rohren." *VDI-Forschungsheft*; English trans., NACA Tech. Mem. 1292.

Shan H., Kerenyi K., Guo J., Shen J., Wagner A., and Xie. Z., (2012). "An ex-situ scour testing device for characterizing erosion of cohesive soils." 6th International Conference on Scour and Erosion (ICSE-6).

Shan H., Shen J., Kilgoe R., and Kerenyi K., (2015). "Scour in Cohesive Soils." U.S. Department of Transportation Federal Highway Administration. McLean, VA.

Straub, T.D., and Over, T.M. (2010). "Pier and Contraction Scour Prediction in Cohesive Soils at Selected Bridges in Illinois." Illinois Center for Transportation, Research Report ICT-10-074, Rantoul, IL.

Ting, F. C. K., and Kern, G. (2022). "Finding the bed shear stress on a rough bed using the log law." *Journal of Waterway, Port, Coastal, and Ocean Engineering* 148(4), 04022008.

Ting, F. C. K., and Kidd, B. (2022). "Flood hydrology generation for predicting bridge scour in cohesive soils." MPC-22-459. Mountain-Plains Consortium.

Validyne Engineering Corp. "Differential Pressure Transducer User Manual."

# 9. APPENDIX A. PROCEDURE FOR FINDING THE FLOW RATE IN A-8 HYDRAULIC CHANNEL

The discharge in the A-8 hydraulic channel with a gravel bed installed was measured using a 7.62-cm diameter orifice that had been calibrated in the factory using a V-notch weir. The flow discharge is related to the differential pressure head:

$$Q = k\sqrt{\Delta h}$$

where $k$ is the discharge coefficient (= 0.2887); $\Delta h$ is the differential pressure head, ft; and $Q$ is the discharge rate, $ft^3/s$.

**Figure A.1** A-8 hydraulic channel

The differential pressure across the orifice was measured using a low range differential pressure transducer manufactured by Validyne with a pressure range of 5.5-inch $H_2O$ (0.2 psi)

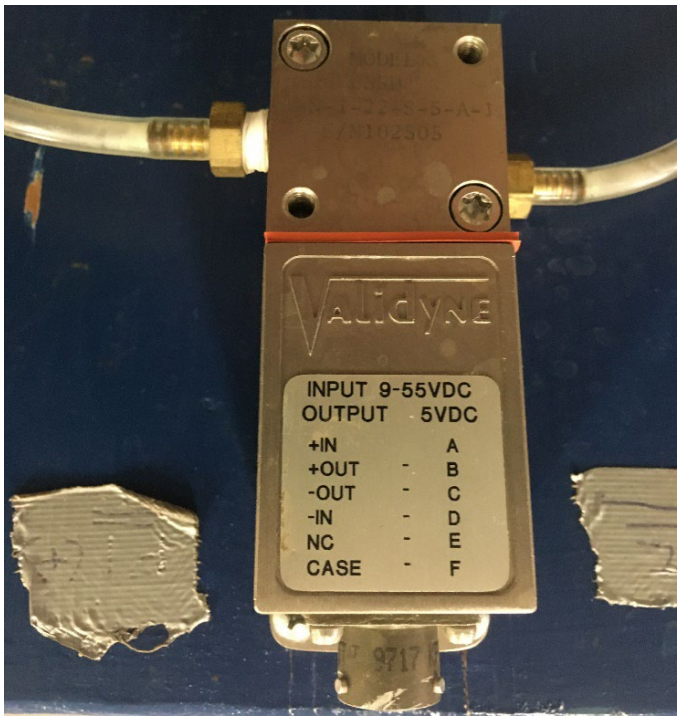


**Figure A.2** Differential pressure transducer

The differential pressure transducer was calibrated using two static manometer columns to obtain a calibration curve between the differential pressure head ($\Delta h$) and the measured voltage (volt). The calibration procedure is described below.


**Figure A.3** Static manometer setup

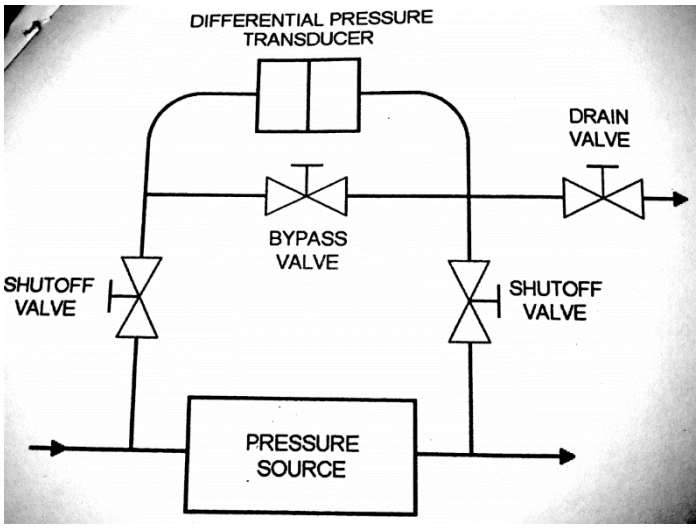


**Figure A.4** Schematic of differential pressure transducer setup (Validyne Engineering Corp.)

1. The differential pressure transducer was connected to pressure taps on the manometers using the setup shown in Figures A.3 and A4.
2. The tubing was flooded with water and trapped air was bled from the system through two bleed holes on the sides of the pressure transducer.
3. Once water had completely flooded the tubing system connected to the differential pressure transducer, the water levels in both manometer tubes were filled to the same height.
4. A voltage output from the differential pressure transducer was sampled at 50 Hz for 1 minute (3,000 data points) using a data acquisition system and averaged. The procedure was repeated with different differential pressure heights, $\Delta h$, over the full range of the pressure transducer to establish a calibration curve

$$\Delta h \text{ (ft)} = 0.1003 * (\text{voltage output}) + 0.00710$$

5. The differential pressure transducer was disconnected from the manometer tubes and connected to pressure taps on each side of the large orifice in the A-8 hydraulic channel.

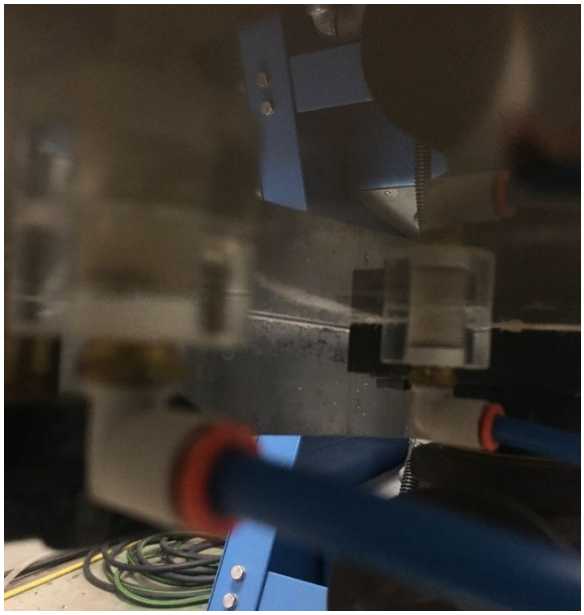

**Figure A.5** Pressure taps on each side of orifice in hydraulic channel (bottom view)

6. The hydraulic channel was set to a 1% slope and the pump was turned on at maximum discharge.
7. After a uniform flow was established, voltage readings were taken over a one-minute period at a sample rate of 50 Hz and averaged. Two water depth measurements were also taken using a point gauge, at $^2/_3$ and ¾ length along the flume, and averaged.
8. The averaged voltage reading was then used with the calibration curve to determine $\Delta h$. The measured $\Delta h$ was corrected for the difference in the elevation of the pressure taps due to the slope of the flume.
9. The corrected $\Delta h$ was used in the factory calibrated orifice equation to calculate the discharge.

$$Q = 0.2887\sqrt{\Delta h}$$

10. Steps 9-12 were then repeated at slopes of 2% to 12%.

**Table A.1** Measured flow depth and discharge over a fixed gravel bed at different slopes in A-8 hydraulic channel

| Slope | Measured $Q$ ($ft^3/s$) | Measured Water Depth (in) |
|---|---|---|
| 0.01 | 0.1585 | 1.815 |
| 0.02 | 0.1580 | 1.545 |
| 0.03 | 0.1607 | 1.395 |
| 0.04 | 0.1599 | 1.270 |
| 0.05 | 0.1569 | 1.215 |
| 0.06 | 0.1566 | 1.16 |
| 0.07 | 0.1567 | 1.115 |
| 0.08 | 0.1563 | 1.065 |
| 0.09 | 0.1585 | 1.03 |
| 0.1 | 0.1594 | 1.005 |
| 0.11 | 0.1578 | 0.985 |
| 0.12 | 0.1576 | 0.96 |

# 10. APPENDIX B. SOIL EROSION TEST RESULTS

**Table B.1** Hydraulic channel erosion test results for bed shear stress < 16 N/m$^2$

| Slope (%) | Initial $w$ (%) | Final $w$ (%) | Time (min) | SA (in$^2$) | $H_0$ (in) | $M_{0,\text{wet}}$ (g) | $M_{f,\text{wet}}$ (g) | $M_{0,\text{dry}}$ (g) | $M_{f,\text{dry}}$ (g) | $Y$ US sample (in) | $Y$ at Sample (in) | $Y$ DS Sample (in) | Avg. Water Depth (in) | Difference Soil Mass (g) | Percent of Sample | Erosion Rate (in/min) | **Erosion Rate (mm/h)** | $\tau_b$ (N/m$^2$) | $Q_u$ (psi) |
|---|---|---|---|---|---|---|---|---|---|---|---|---|---|---|---|---|---|---|---|
| 1 | 19.45% | 21.44% | 250 | 2.16 | 1.625 | 281.51 | 284.12 | 235.67 | 233.96 | 2.00 | 1.96 | 1.81 | 1.923 | 1.71 | 0.7% | 4.7E-05 | **0.07** | 3.8034 | 33.137 |
| 2 | 19.45% | 20.93% | 250 | 2.16 | 1.75 | 311.61 | 313.74 | 260.87 | 259.43 | 1.56 | 1.66 | 1.39 | 1.537 | 1.44 | 0.6% | 3.9E-05 | **0.06** | 6.2041 | 33.137 |
| 4 | 24.23% | 29.27% | 249 | 2.16 | 1.375 | 270.89 | 280.50 | 218.06 | 216.98 | 1.24 | 1.35 | 1.17 | 1.253 | 1.08 | 0.5% | 2.72E-05 | **0.04** | 10.2461 | 14.977 |
| 5 | 24.96% | 28.10% | 540 | 2.16 | 1.4375 | 280.94 | 227.82 | 224.82 | 177.84 | 1.21 | 1.16 | 1.20 | 1.190 | 46.98 | 20.9% | 5.56E-04 | **0.85** | 12.2264 | 9.975 |
| 5 | 20.69% | 25.01% | 374 | 2.16 | 1.375 | 265.13 | 262.60 | 219.679 | 210.07 | 1.21 | 1.20 | 1.21 | 1.207 | 9.61 | 4.4% | 1.61E-04 | **0.25** | 12.4457 | 21.756 |
| 5 | 25.64% | 28.26% | 120 | 2.16 | 1.625 | 318.49 | 316.96 | 253.49 | 247.12 | 1.16 | 1.31 | 1.16 | 1.210 | 6.37 | 2.5% | 3.41E-04 | **0.52** | 12.4844 | 9.223 |
| 5 | 24.63% | 26.18% | 420 | 2.16 | 1.4375 | 283.05 | 236.33 | 227.11 | 187.3 | 1.23 | 1.25 | 1.23 | 1.237 | 39.81 | 17.5% | 6.00E-04 | **0.91** | 12.8322 | 15.389 |
| 6 | 24.63% | 28.29% | 235 | 2.16 | 1.4375 | 270.47 | 218.72 | 217.02 | 170.49 | 1.16 | 1.15 | 1.15 | 1.153 | 46.53 | 21.4% | 1.31E-03 | **2.00** | 14.2976 | 15.389 |
| 6 | 24.57% | 26.78% | 185 | 2.16 | 1.375 | 262.99 | 249.68 | 211.12 | 196.94 | 1.17 | 1.13 | 1.17 | 1.153 | 14.18 | 6.7% | 4.99E-04 | **0.76** | 14.2976 | 15.796 |
| 7 | 24.23% | 27.56% | 280 | 2.16 | 1.375 | 265.66 | 269.16 | 213.85 | 211.01 | 1.00 | 1.12 | 1.01 | 1.043 | 2.84 | 1.3% | 6.51E-05 | **0.10** | 14.8744 | 14.977 |
| 7 | 24.96% | 29.03% | 240 | 2.16 | 1.5 | 275.14 | 191.15 | 220.18 | 148.14 | 1.05 | 1.04 | 1.07 | 1.052 | 72.04 | 32.7% | 2.04E-03 | **3.12** | 15.0366 | 9.975 |

Note: Green highlighted tests conducted with PIV measurements

**Table B.2** Hydraulic channel erosion test results for bed shear stress 16 N/m$^2$ – 19.5 N/m$^2$

| Slope (%) | Initial $w$ (%) | Final $w$ (%) | Time (min) | SA (in$^2$) | $H_0$ (in) | $M_{0,\text{ wet}}$ (g) | $M_{\text{f, wet}}$ (g) | $M_{0,\text{dry}}$ (g) | $M_{\text{f, dry}}$ (g) | $Y$ US sample (in) | $Y$ at Sample (in) | $Y$ DS Sample (in) | Avg. Water Depth (in) | Difference Soil Mass (g) | Percent of Sample | Erosion Rate (in/min) | **Erosion Rate (mm/h)** | $\tau_{b1}$ (N/m$^2$) | $Q_u$ (psi) |
|---|---|---|---|---|---|---|---|---|---|---|---|---|---|---|---|---|---|---|---|
| 7 | 24.06% | 26.83% | 180 | 2.16 | 1.375 | 254.38 | 220.66 | 205.05 | 173.98 | 1.12 | 1.10 | 1.11 | 1.108 | 31.07 | 15.2% | 1.16E-03 | **1.76** | 16.0443 | 15.046 |
| 7 | 20.69% | 24.02% | 335 | 2.16 | 1.5625 | 307.38 | 289.68 | 254.686 | 233.58 | 1.10 | 1.14 | 1.11 | 1.115 | 21.11 | 8.3% | 3.87E-04 | **0.59** | 16.1700 | 21.756 |
| 7 | 24.17% | 27.47% | 160 | 2.16 | 1.4375 | 293.75 | 243.73 | 236.57 | 191.2 | 1.13 | 1.12 | 1.12 | 1.123 | 45.37 | 19.2% | 1.72E-03 | **2.63** | 16.3136 | 15.321 |
| 8 | 25.64% | 31.00% | 79 | 2.16 | 1.5 | 300.53 | 260.04 | 239.20 | 198.51 | 1.02 | 1.06 | 1.00 | 1.027 | 40.69 | 17.0% | 3.23E-03 | **4.92** | 16.8295 | 9.223 |
| 7 | 19.01% | 20.87% | 280 | 2.16 | 1.5 | 315.07 | 288.45 | 264.74 | 238.64 | 1.17 | 1.18 | 1.17 | 1.173 | 26.10 | 9.9% | 5.3E-04 | **0.80** | 17.2100 | 34.918 |
| 8 | 23.64% | 26.71% | 370 | 2.16 | 1.4375 | 284.79 | 223.66 | 230.34 | 176.51 | 1.07 | 1.02 | 1.05 | 1.047 | 53.83 | 23.4% | 9.08E-04 | **1.38** | 17.2402 | 16.187 |
| 8 | 22.85% | 24.66% | 210 | 2.16 | 1.625 | 326.08 | 273.20 | 265.43 | 219.15 | 1.07 | 1.04 | 1.03 | 1.047 | 46.28 | 17.4% | 1.35E-03 | **2.06** | 17.2402 | 18.3 |
| 8 | 22.40% | 31.37% | 300 | 2.16 | 1.3750 | 257.81 | 230.17 | 210.63 | 175.21 | 1.05 | 1.07 | 1.05 | 1.053 | 35.42 | 16.8% | 7.71E-04 | **1.17** | 17.3633 | 16.812 |
| 8 | 24.96% | 28.08% | 276 | 2.16 | 1.4375 | 251.61 | 209.20 | 201.35 | 163.33 | 1.06 | 1.06 | 1.05 | 1.057 | 38.02 | 18.9% | 9.84E-04 | **1.50** | 17.4454 | 9.975 |
| 8 | 23.64% | 25.41% | 310 | 2.16 | 1.4375 | 277.37 | 213.67 | 224.34 | 170.38 | 1.06 | 1.06 | 1.06 | 1.057 | 53.96 | 24.1% | 1.12E-03 | **1.70** | 17.4454 | 16.187 |
| 8 | 24.06% | 25.04% | 160 | 2.16 | 1.4375 | 270.42 | 188.59 | 217.98 | 150.82 | 1.07 | 1.07 | 1.06 | 1.063 | 67.16 | 30.81% | 2.77E-03 | **4.22** | 17.5684 | 15.046 |
| 8.2 | 20.02% | 22.50% | 302 | 2.16 | 1.5 | 264.28 | 266.36 | 220.197 | 217.43 | 1.06 | 1.05 | 1.06 | 1.053 | 2.77 | 1.3% | 6.24E-05 | **0.10** | 17.8254 | 27.423 |
| 8 | 20.69% | 25.76% | 340 | 2.16 | 1.5625 | 297.39 | 278.60 | 246.408 | 221.53 | 1.07 | 1.11 | 1.08 | 1.083 | 24.88 | 10.1% | 4.64E-04 | **0.71** | 17.9783 | 21.756 |
| 8 | 19.01% | 20.80% | 285 | 2.16 | 1.75 | 359.47 | 362.37 | 302.05 | 299.97 | 1.10 | 1.12 | 1.10 | 1.107 | 2.08 | 0.7% | 4.2E-05 | **0.06** | 18.4696 | 34.918 |
| 9 | 24.06% | 26.36% | 120 | 2.16 | 1.375 | 268.15 | 248.76 | 216.15 | 196.87 | 1.03 | 1.02 | 1.02 | 1.023 | 19.28 | 8.92% | 1.02E-03 | **1.56** | 18.9842 | 15.046 |
| 9 | 21.93% | 21.71% | 314 | 2.16 | 1.625 | 335.85 | 302.08 | 275.445 | 240.3 | 1.03 | 1.02 | 1.03 | 1.027 | 35.14 | 12.8% | 6.60E-04 | **1.01** | 19.0764 | 21.725 |
| 9 | 24.63% | 26.83% | 185 | 2.16 | 1.4375 | 281.23 | 239.97 | 225.65 | 189.2 | 1.04 | 1.05 | 1.04 | 1.043 | 36.45 | 16.2% | 1.26E-03 | **1.91** | 19.4448 | 15.389 |

Note: Green highlighted tests conducted with PIV measurements

**Table B.3** Hydraulic channel erosion test results for bed shear stress > 19.5 N/m$^2$

| Slope (%) | Initial $w$ (%) | Final $w$ (%) | Time (min) | SA (in$^2$) | $H_0$ (in) | $M_{0,\text{wet}}$ (g) | $M_{f,\text{wet}}$ (g) | $M_{0,\text{dry}}$ (g) | $M_{f,\text{dry}}$ (g) | $Y$ US sample (in) | $Y$ at Sample (in) | $Y$ DS Sample (in) | Avg. Water Depth (in) | Difference Soil Mass (g) | Percent of Sample | Erosion Rate (in/min) | **Erosion Rate (mm/h)** | $\tau_{b1}$ (N/m$^2$) | $Q_u$ (psi) |
|---|---|---|---|---|---|---|---|---|---|---|---|---|---|---|---|---|---|---|---|
| 10 | 23.33% | 27.09% | 246 | 2.16 | 1.625 | 326.26 | 259.13 | 264.54 | 203.9 | 0.95 | 0.95 | 0.99 | 0.963 | 60.64 | 22.9% | 1.51E-03 | **2.31** | 19.6889 | 16.145 |
| 9 | 22.85% | 24.72% | 180 | 2.16 | 1.625 | 324.48 | 301.76 | 264.13 | 241.95 | 1.06 | 1.07 | 1.04 | 1.057 | 22.18 | 8.4% | 7.58E-04 | **1.16** | 19.7670 | 18.3 |
| 9 | 18.93% | 21.94% | 375 | 2.16 | 1.625 | 315.04 | 316.22 | 264.895 | 259.33 | 1.06 | 1.09 | 1.05 | 1.067 | 5.57 | 2.1% | 9.10E-05 | **0.14** | 19.9970 | 25.54 |
| 10 | 22.85% | 27.31% | 153 | 2.16 | 1.625 | 320.02 | 256.74 | 260.50 | 201.66 | 1.03 | 0.93 | 0.97 | 0.977 | 58.84 | 22.6% | 2.40E-03 | **3.66** | 20.0475 | 18.3 |
| 9 | 19.01% | 22.88% | 212 | 2.16 | 1.375 | 277.96 | 241.11 | 233.56 | 196.22 | 1.08 | 1.06 | 1.07 | 1.070 | 37.34 | 16.0% | 1.0E-03 | **1.58** | 20.066 | 34.918 |
| 10 | 24.17% | 27.15% | 165 | 2.16 | 1.375 | 262.31 | 185.06 | 211.25 | 145.55 | 1.01 | 1.00 | 1.01 | 1.005 | 65.70 | 31.1% | 2.59E-03 | **3.95** | 20.7637 | 15.321 |
| 10 | 24.57% | 27.27% | 160 | 2.16 | 1.375 | 253.17 | 205.55 | 203.24 | 161.51 | 1.02 | 1.01 | 1.01 | 1.012 | 41.73 | 20.5% | 1.76E-03 | **2.69** | 20.9426 | 15.796 |
| 11 | 23.33% | 27.87% | 230 | 2.16 | 1.625 | 327.44 | 256.47 | 265.50 | 200.57 | 0.95 | 0.94 | 0.96 | 0.950 | 64.93 | 24.5% | 1.73E-03 | **2.63** | 21.4152 | 16.145 |
| 10 | 24.18% | 25.84% | 120 | 2.16 | 1.625 | 321.23 | 269.34 | 258.68 | 214.04 | 1.05 | 0.98 | 1.06 | 1.030 | 44.64 | 17.3% | 2.34E-03 | **3.56** | 21.4023 | 11.901 |
| 11 | 23.64% | 28.05% | 165 | 2.16 | 1.4375 | 290.06 | 225.99 | 234.60 | 176.46 | 0.99 | 0.96 | 0.99 | 0.980 | 58.14 | 24.8% | 2.16E-03 | **3.29** | 22.2586 | 16.187 |
| 11 | 24.17% | 29.38% | 136 | 2.16 | 1.375 | 267.37 | 208.82 | 215.33 | 161.4 | 0.98 | 0.99 | 0.98 | 0.982 | 53.93 | 25.0% | 2.53E-03 | **3.86** | 22.2147 | 15.321 |
| 11 | 20.36% | 25.13% | 271 | 2.16 | 1.5625 | 309.26 | 248.49 | 256.95 | 198.58 | 0.99 | 0.97 | 1.01 | 0.990 | 58.37 | 22.7% | 1.3E-03 | **2.00** | 22.5394 | 25.763 |
| 11 | 18.93% | 23.92% | 242 | 2.16 | 1.5 | 308.48 | 223.32 | 259.38 | 180.21 | 1.04 | 0.92 | 1.02 | 0.993 | 79.17 | 30.5% | 1.89E-03 | **2.88** | 22.6236 | 25.54 |
| 11 | 19.91% | 21.06% | 330 | 2.16 | 1.625 | 330.44 | 324.64 | 275.57 | 268.16 | 0.99 | 1.01 | 0.99 | 0.997 | 7.41 | 2.7% | 1.3E-04 | **0.20** | 22.7358 | 29.924 |
| 12 | 20.36% | 26.24% | 300 | 2.16 | 1.625 | 330.73 | 226.23 | 274.78 | 179.2 | 0.96 | 1.01 | 0.93 | 0.967 | 95.58 | 34.8% | 1.9E-03 | **2.87** | 23.997 | 25.763 |
| 12 | 18.76% | 21.08% | 317 | 2.16 | 1.5 | 305.95 | 307.37 | 257.62 | 253.85 | 0.97 | 1.00 | 0.96 | 0.977 | 3.77 | 1.5% | 6.9E-05 | **0.11** | 24.3029 | 37.667 |
| 12 | 18.93% | 22.04% | 240 | 2.16 | 1.625 | 326.16 | 306.23 | 274.245 | 250.92 | 0.98 | 1.03 | 0.98 | 0.997 | 23.33 | 8.5% | 5.76E-04 | **0.88** | 24.9143 | 25.54 |
| 12 | 18.76% | 21.17% | 247 | 2.16 | 1.625 | 349.92 | 311.47 | 294.64 | 256.78 | 0.98 | 1.04 | 0.97 | 0.997 | 37.86 | 12.9% | 8.5E-04 | **1.29** | 24.9143 | 37.667 |

# 11. APPENDIX C. RAW PIV IMAGES OVER COHESIVE SOIL BED

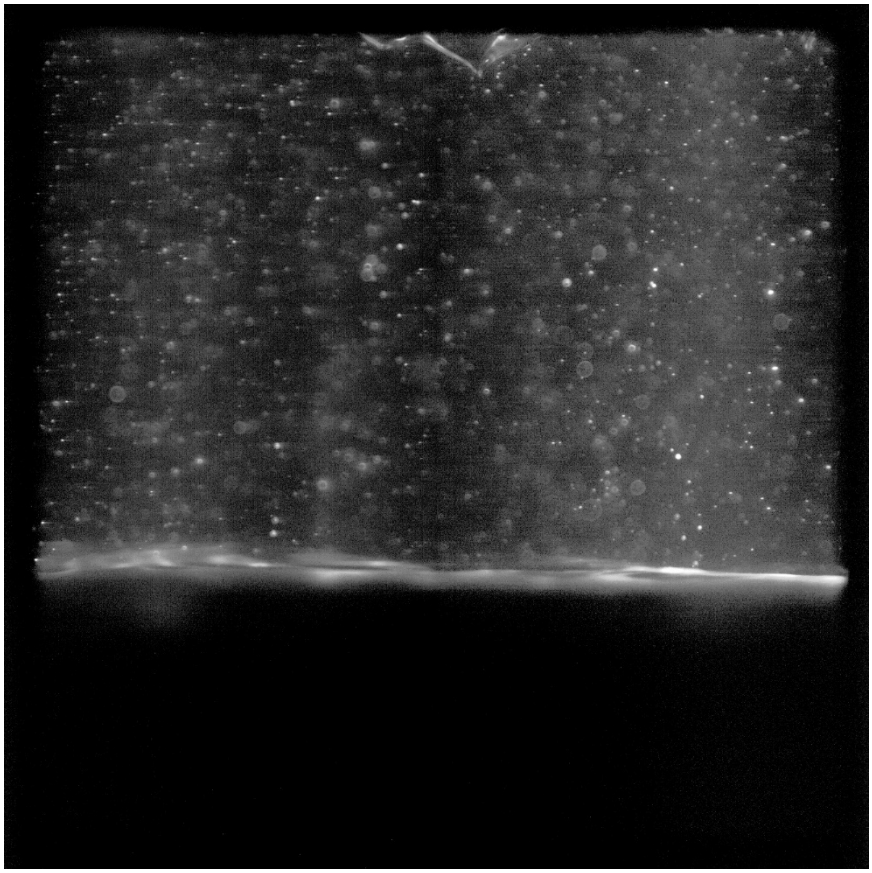

**Figure C.1** Raw PIV image for Test 2

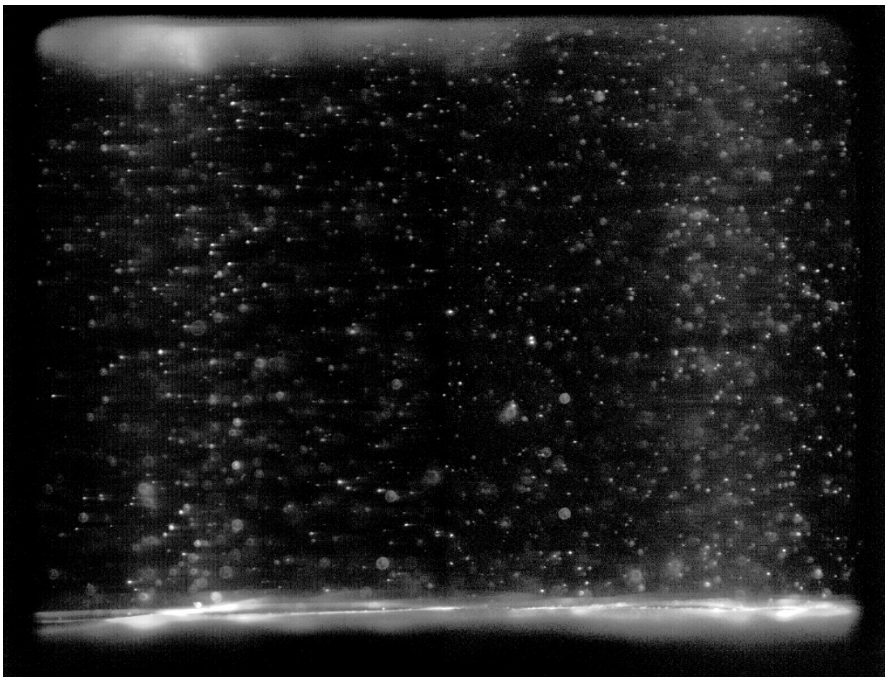

**Figure C.2** Raw PIV image for Test 3

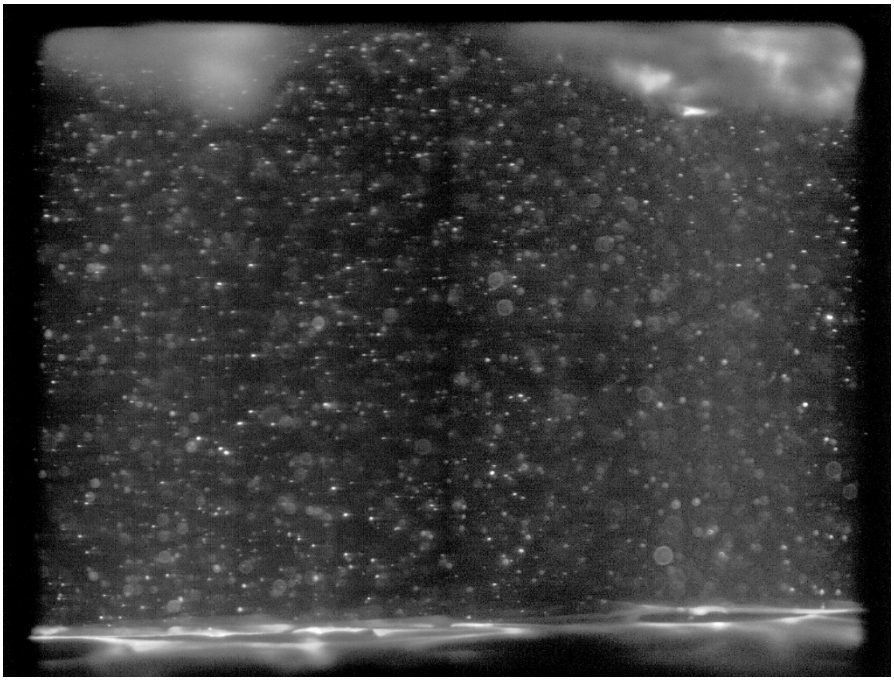

**Figure C.3** Raw PIV image for Test 4

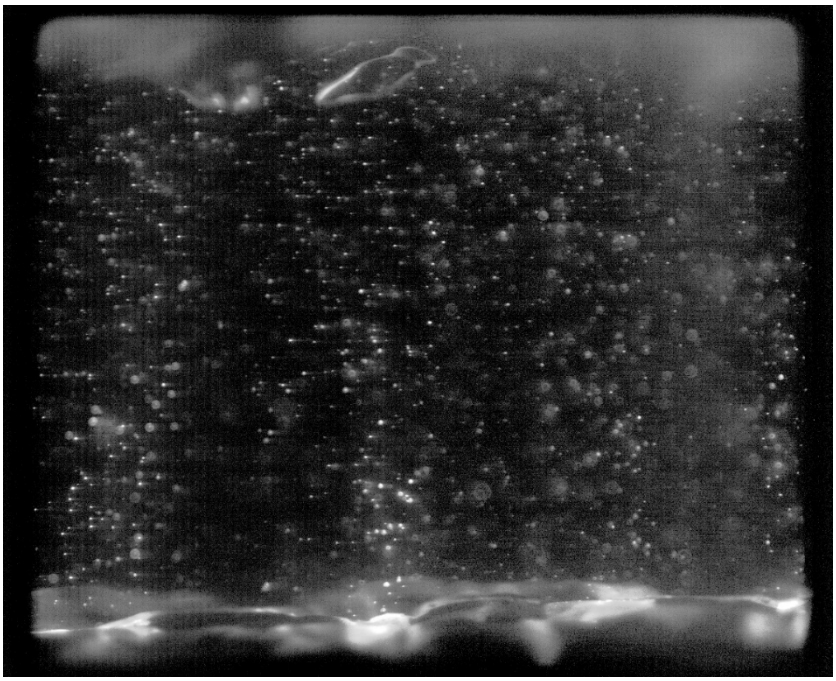

**Figure C.4** Raw PIV image for Test 5

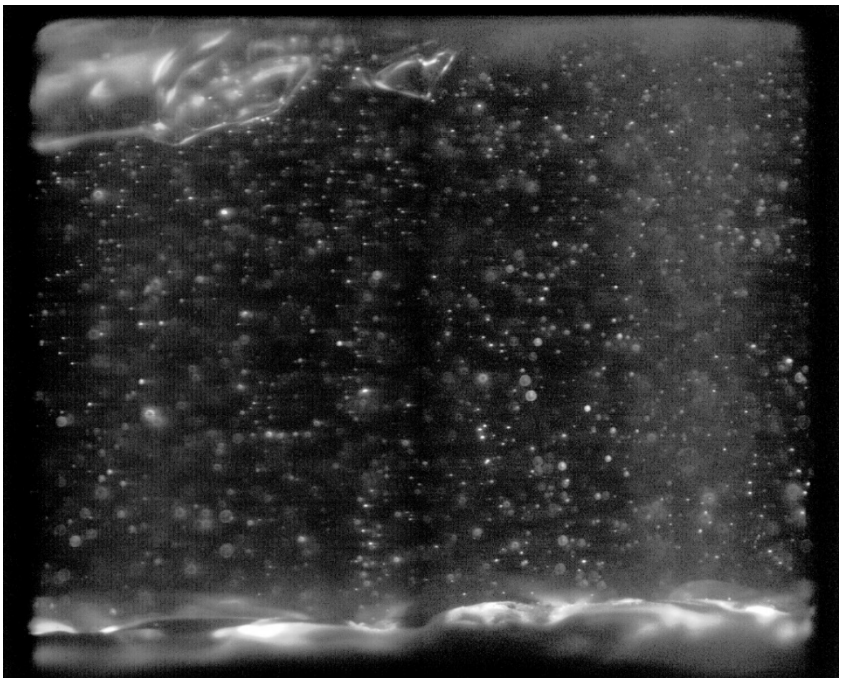

**Figure C.5** Raw PIV image for Test 6

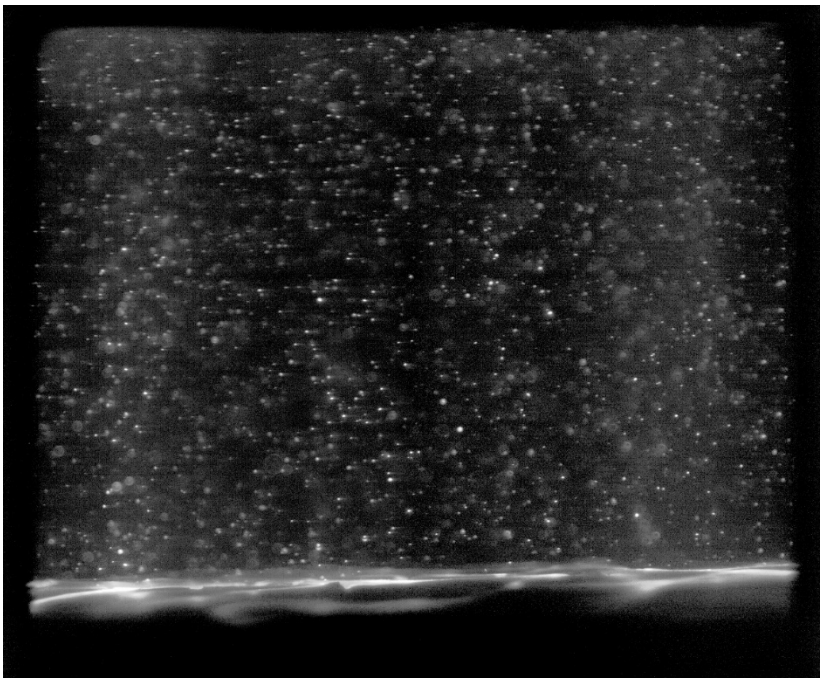

**Figure C.6** Raw PIV image for Test 7

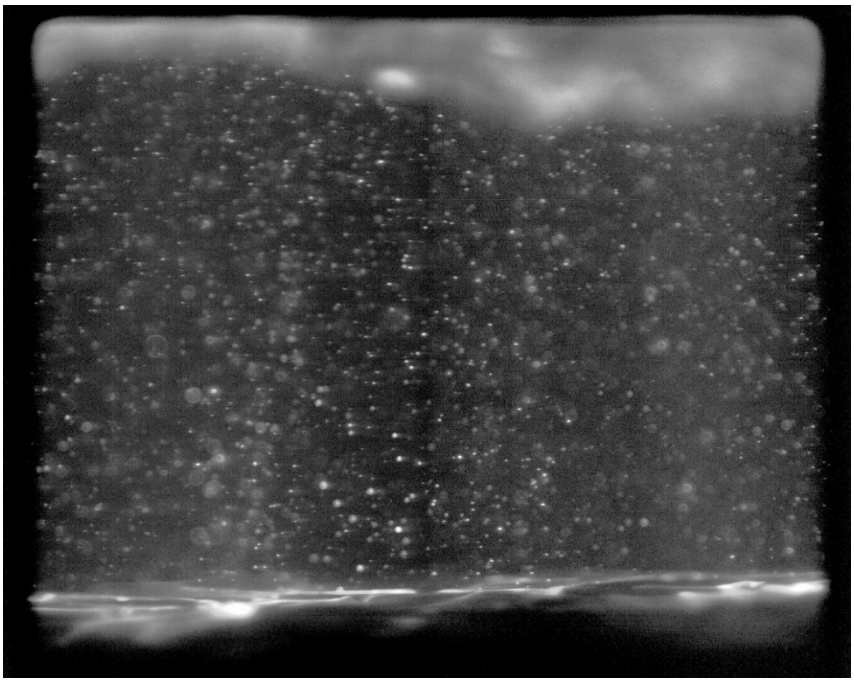

**Figure C.7** Raw PIV images for Test 8

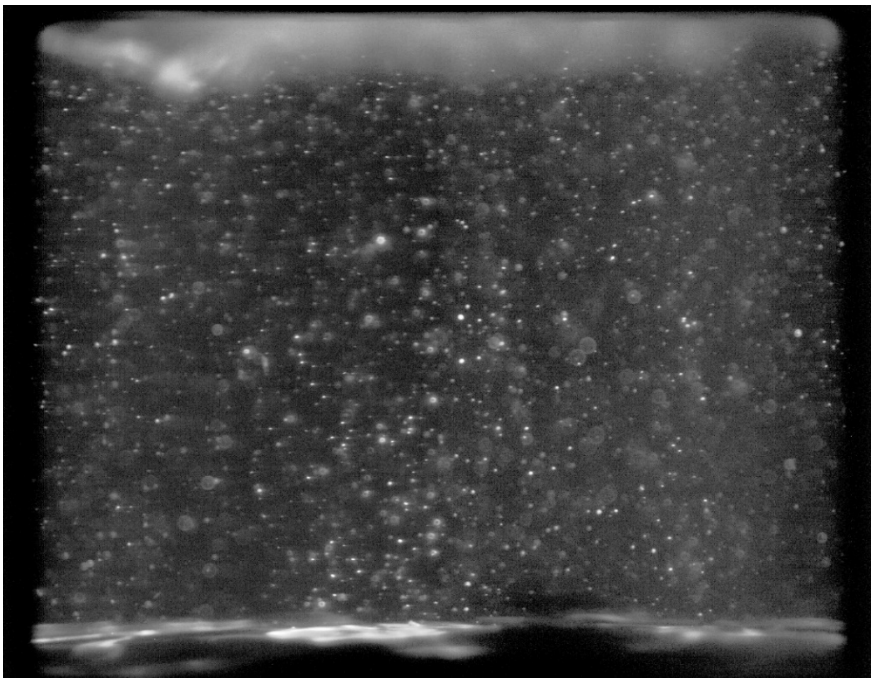

**Figure C.8** Raw PIV image for Test 9

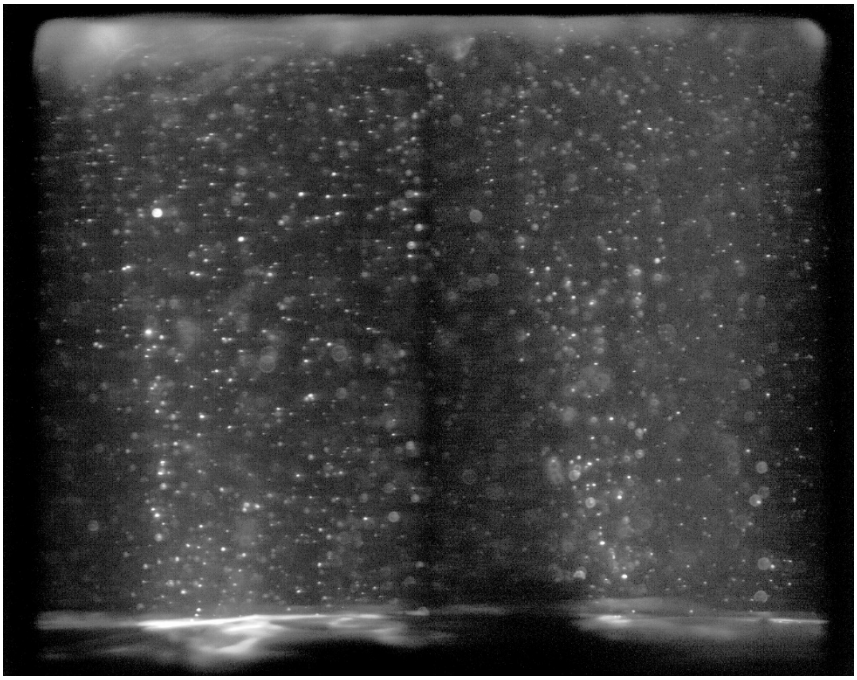

**Figure C.9** Raw PIV image for Test 10

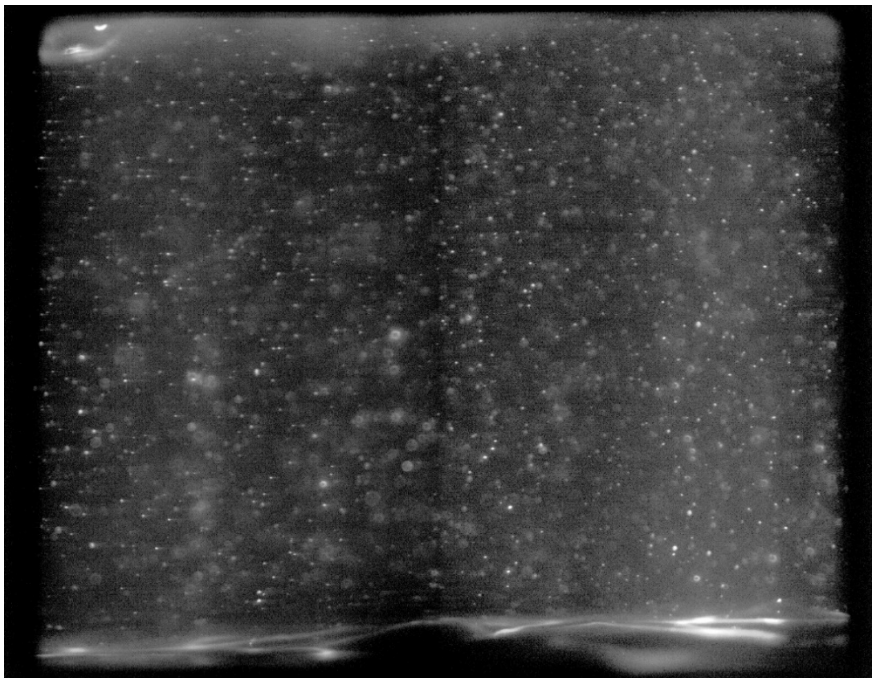

**Figure C.10** Raw PIV image for Test 11

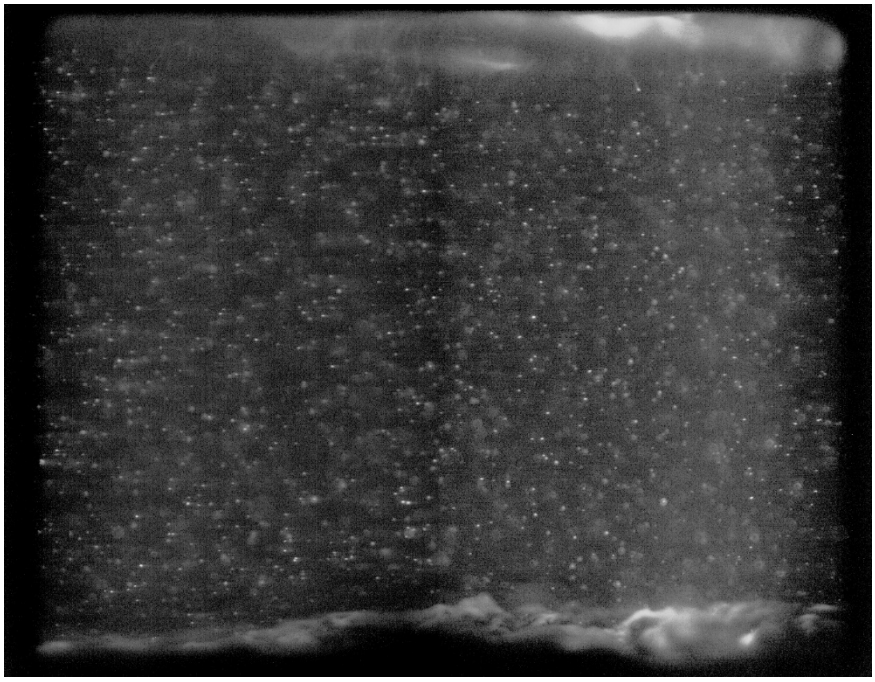

**Figure C.11** Raw PIV image for Test 12

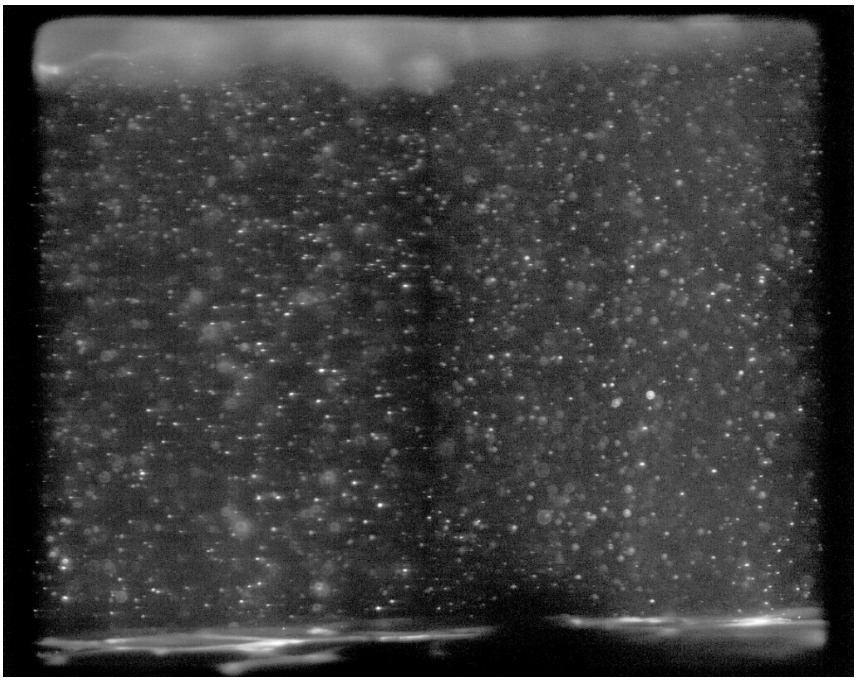

**Figure C.12** Raw PIV image for Test 13

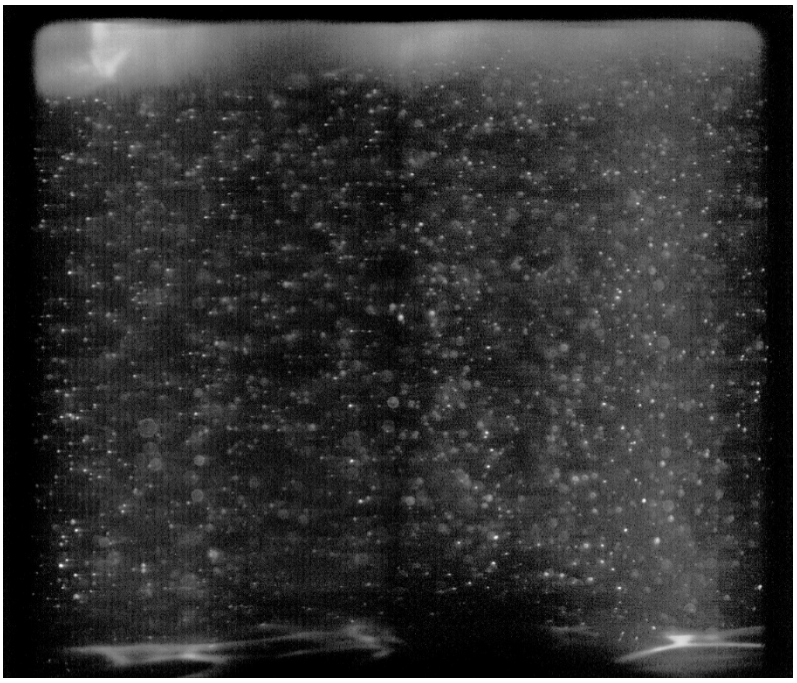

**Figure C.13** Raw PIV image for Test 14

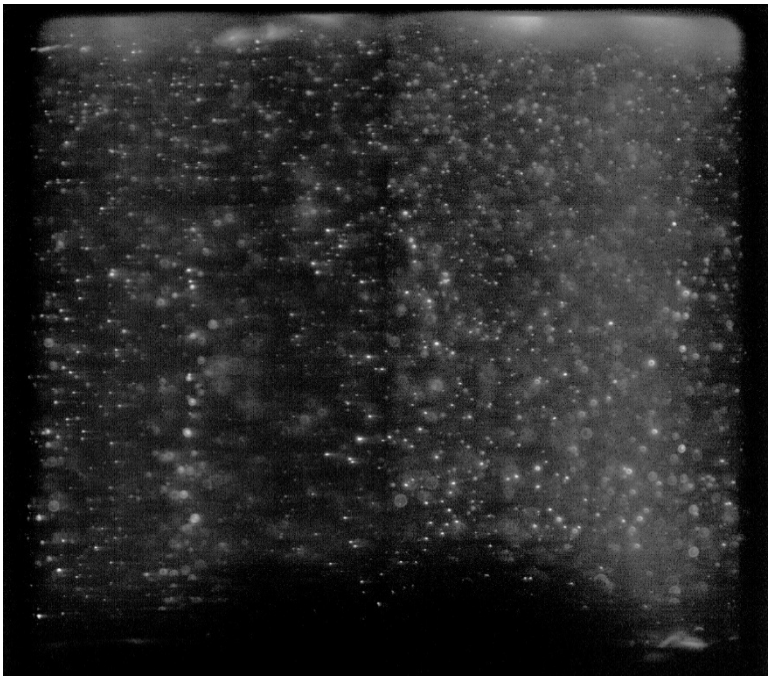

**Figure C.14** Raw PIV image for Test 15

# 12. APPENDIX D. TIME-AVERAGED VELOCITY PROFILES OVER COHESIVE SOIL BED

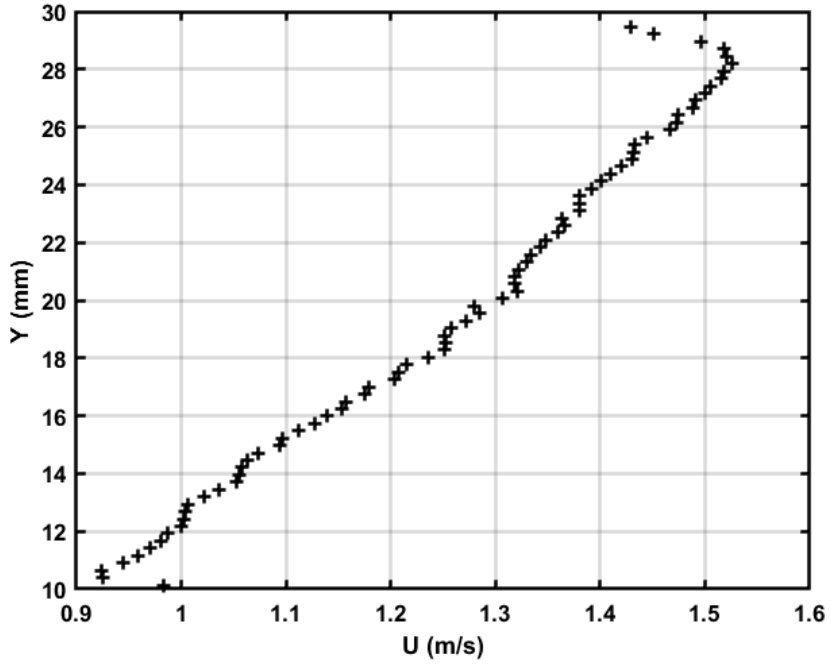


**Figure D.1** Test 2 – time-average velocity profile (zero erosion depth)

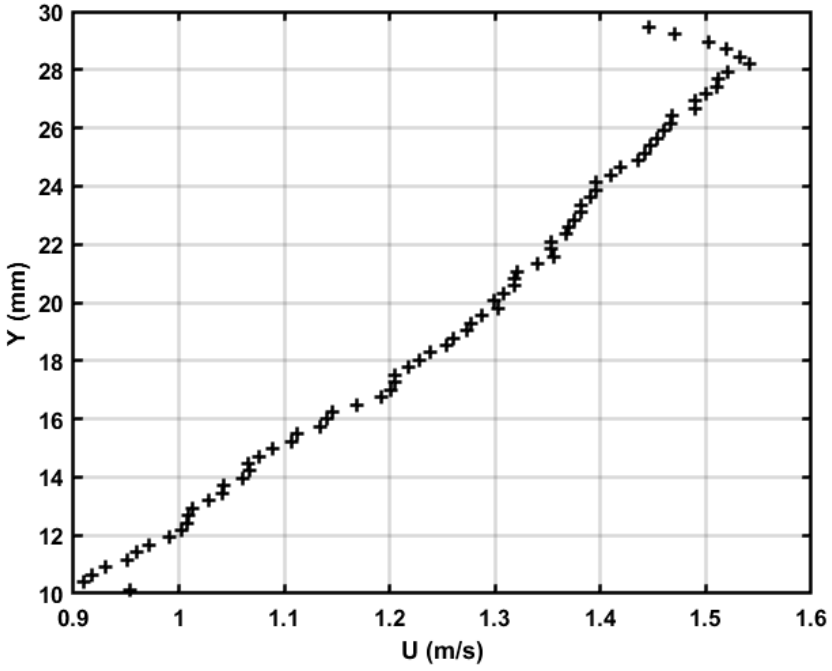


**Figure D.2** Test 3 – time-average velocity profile (zero erosion depth)

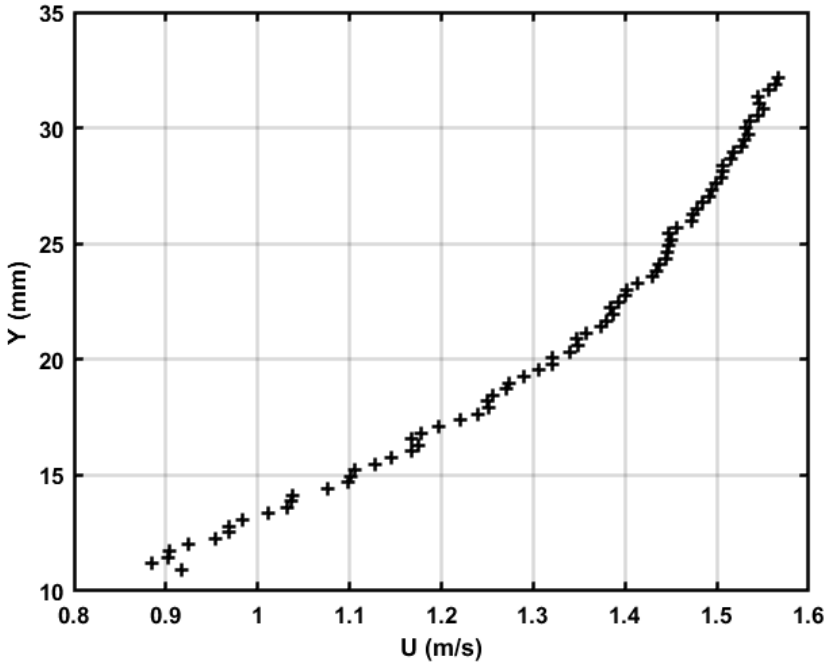


**Figure D.3** Test 5 – time-average velocity profile (1.5 mm erosion depth)

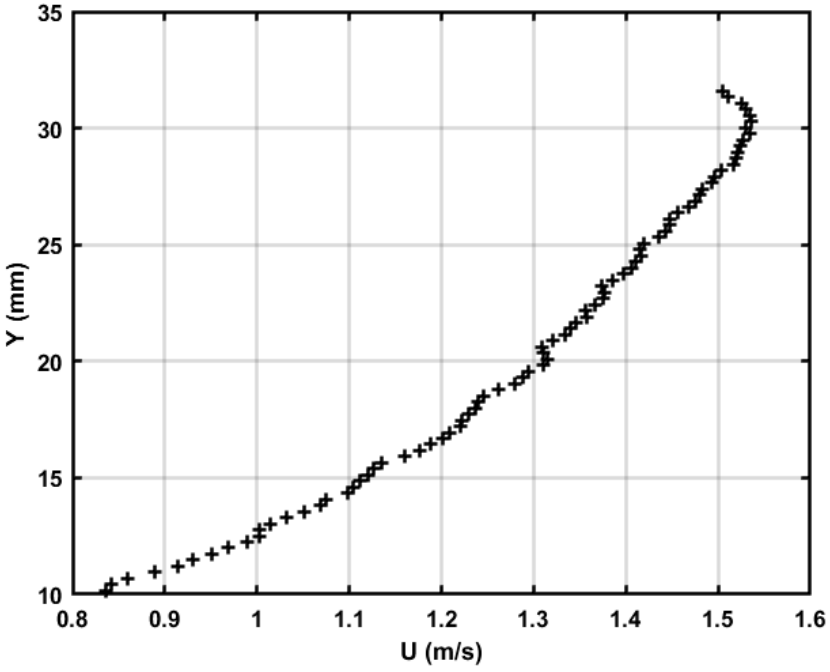


**Figure D.4** Test 6 – time-average velocity profile (1.6 mm erosion depth)

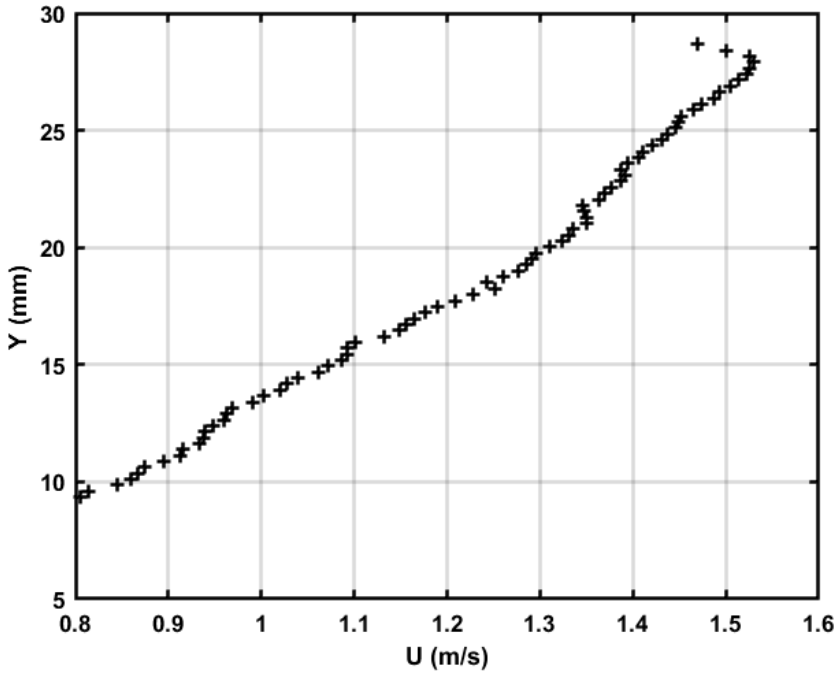


**Figure D.5** Test 7 – time-average velocity profile (1.6 mm erosion depth)

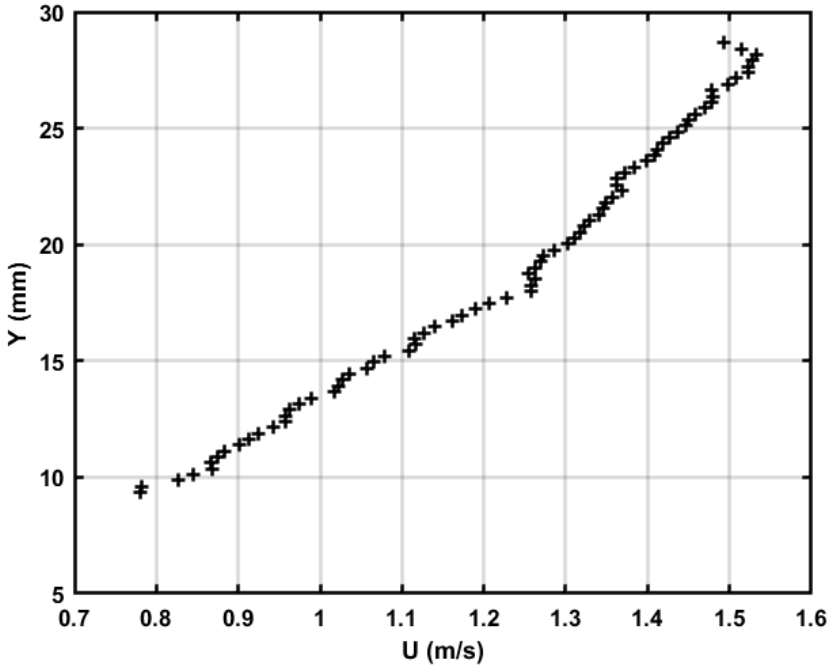


**Figure D.6** Test 8 – time-average velocity profile (1.6 mm erosion depth)

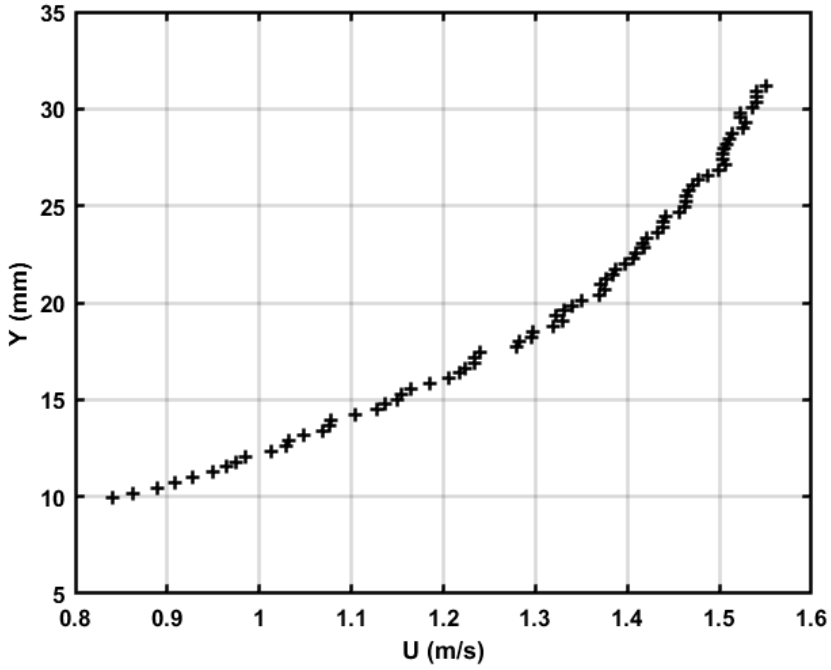


**Figure D.7** Test 9 – time-average velocity profile (2.5 mm erosion depth)

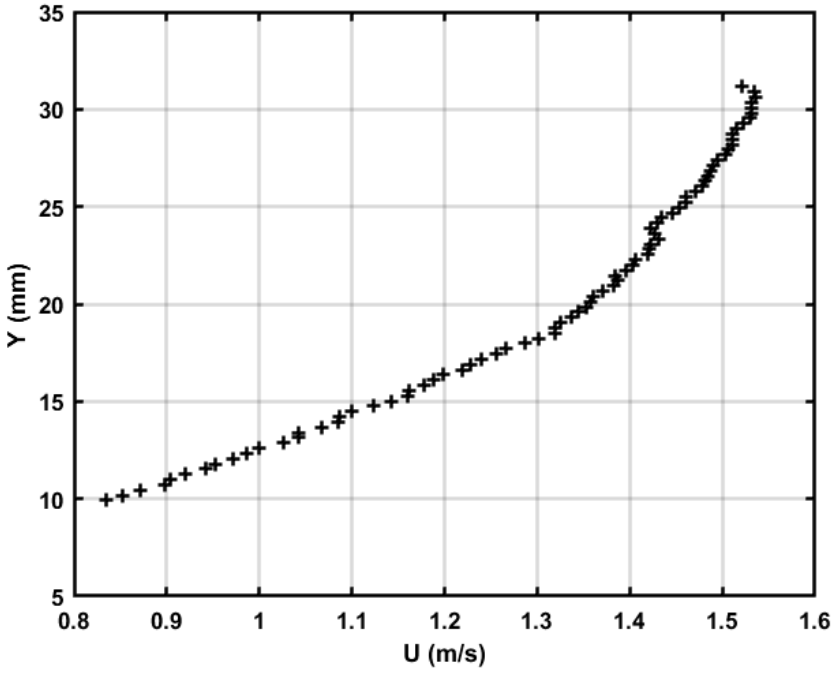


**Figure D.8** Test 10 – time-average velocity profile (2.5 mm erosion depth)

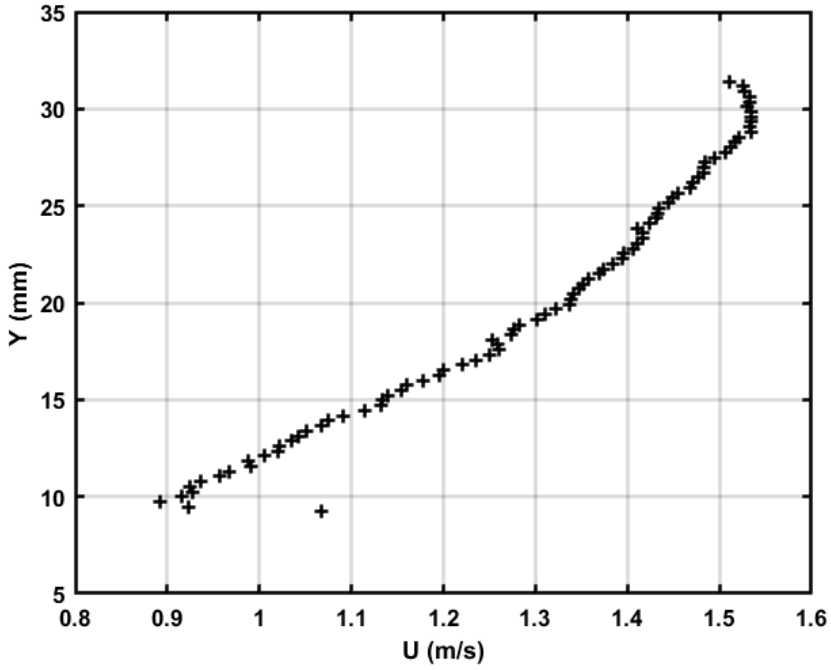


**Figure D.9** Test 11 – time-average velocity profile (3 mm erosion depth)

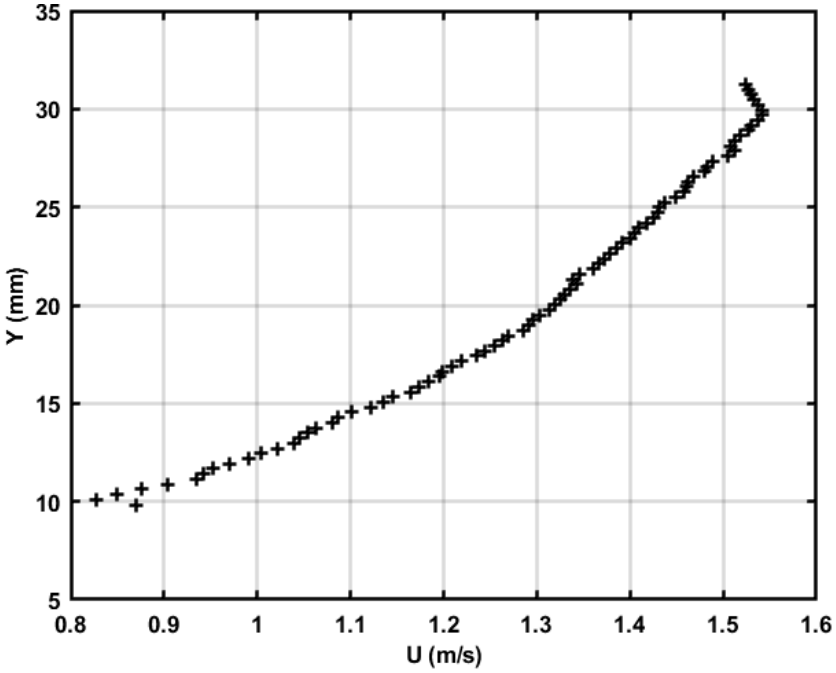


**Figure D.10** Test 12 – time-average velocity profile (3 mm erosion depth)

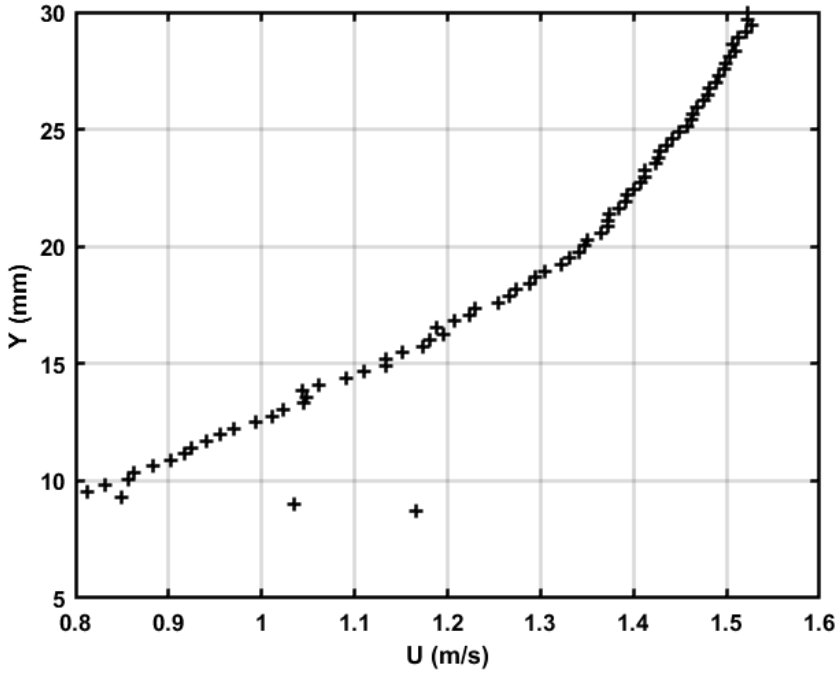


**Figure D.11** Test 13 – time-average velocity profile (4 mm erosion depth)

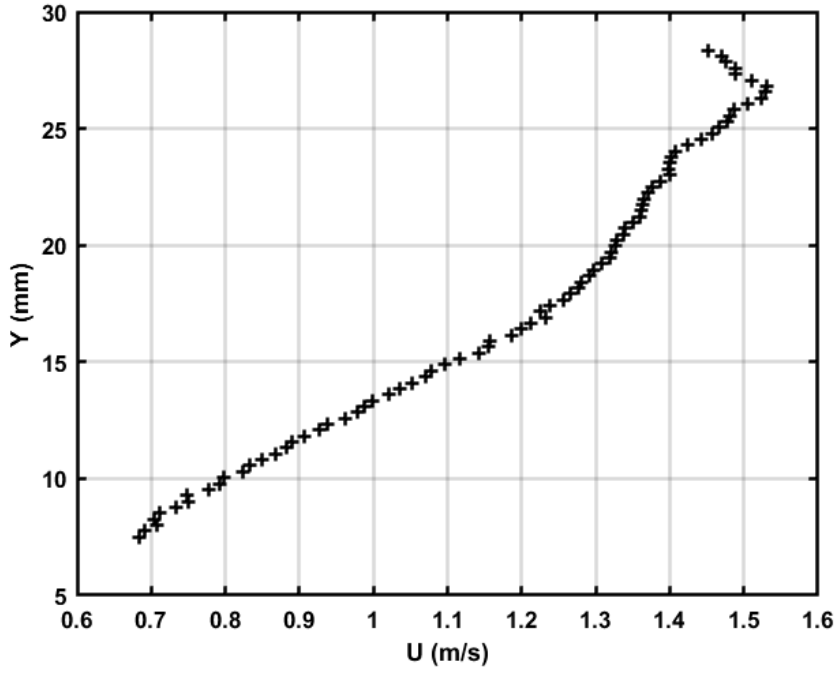


**Figure D.12** Test 14 – time-average velocity profile (4 mm erosion depth)

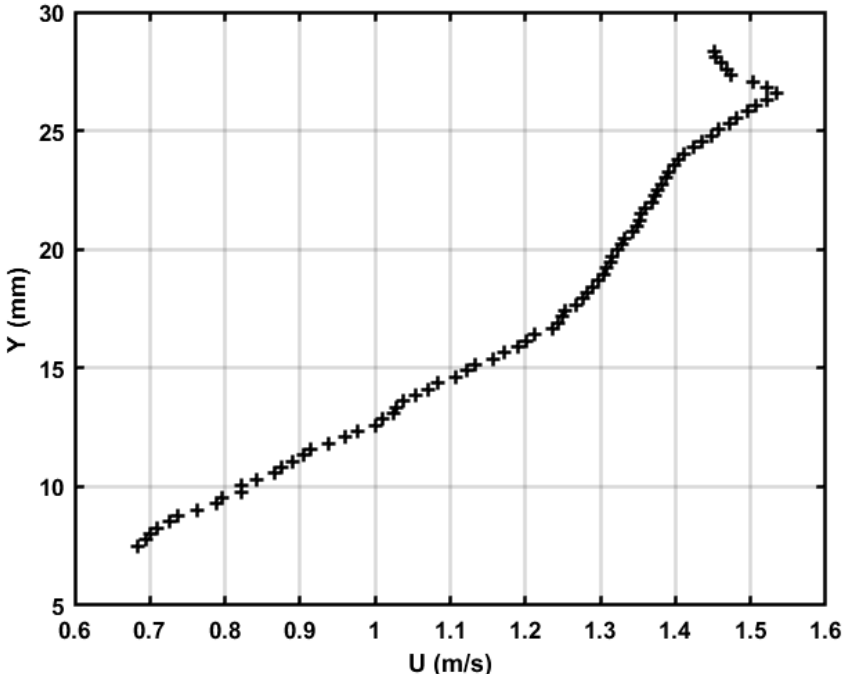


**Figure D.13** Test 15 – time-average velocity profile (5 mm erosion depth)